

6.0 GROUND MOTION MODELING

The influences of large-scale crustal velocity structure and source radiation on rock and soil ground motions at Jackson Lake Dam are the focus of this section. Ground motions are synthesized for the rock site station JLDW for a variety of magnitudes and source geometries to quantify peak ground motions scaling and variability associated with earthquake rupture scenarios postulated for earthquakes on nearby Teton fault segments. The uncertainties in fault dip are accounted for by considering three values of dip for each fault segment, yielding a total of six fault segments to consider when simulating ground motions. The northern segment is assigned a strike length of 42 km and the southern segment is assigned a strike length of 18 km. The depth to the bottom of the Teton fault is assumed to be 16 km for all rupture segments and fault dip scenarios (Figures 6-1 and 6-3). Rupture of the northern Teton fault segment is likely to produce a **M** 6.9 earthquake for a dip of 60° and **M** 7.0 for a dip of 45° (**M** 7.0 is also used for a dip of 35°) based on moment fault area relations of Wells and Coppersmith (1994). Rupture of the northern and southern Teton fault segments in a single fault rupture increases **M** by ~0.2 based on moment fault area relations of Wells and Coppersmith (1994) applied to the entire length of the Teton fault. Rupture of the northern segment for dips of 35° and 45° involves fault rupture directly beneath the dam (Figures 6-1 and 6-3). It is necessary to determine how strongly rupture directivity may influence peak ground motions and ground motion variability at the dam for all of these near-source earthquake scenarios. Impacts of 3D crustal velocity structure are substantial and much of the modeling effort is devoted to accounting for the influences of 3D velocity heterogeneity on ground motion amplitudes and durations, and evaluating the influence of fault dip uncertainties on ground motion characteristics.

6.1 Overall Approach

The basic approach follows Spudich and Archuleta (1987). We use the representation theorem, with a kinematic approximation for seismic radiation from a propagating fault rupture, to estimate linear ground motions for south abutment “rock” site conditions. Synthetic reciprocity Green’s functions (RGF) are calculated using 3D viscoelastic finite-differences using the approach of Graves and Wald (2001) and the 3D velocity-density-attenuation model from Section 4. These 3D

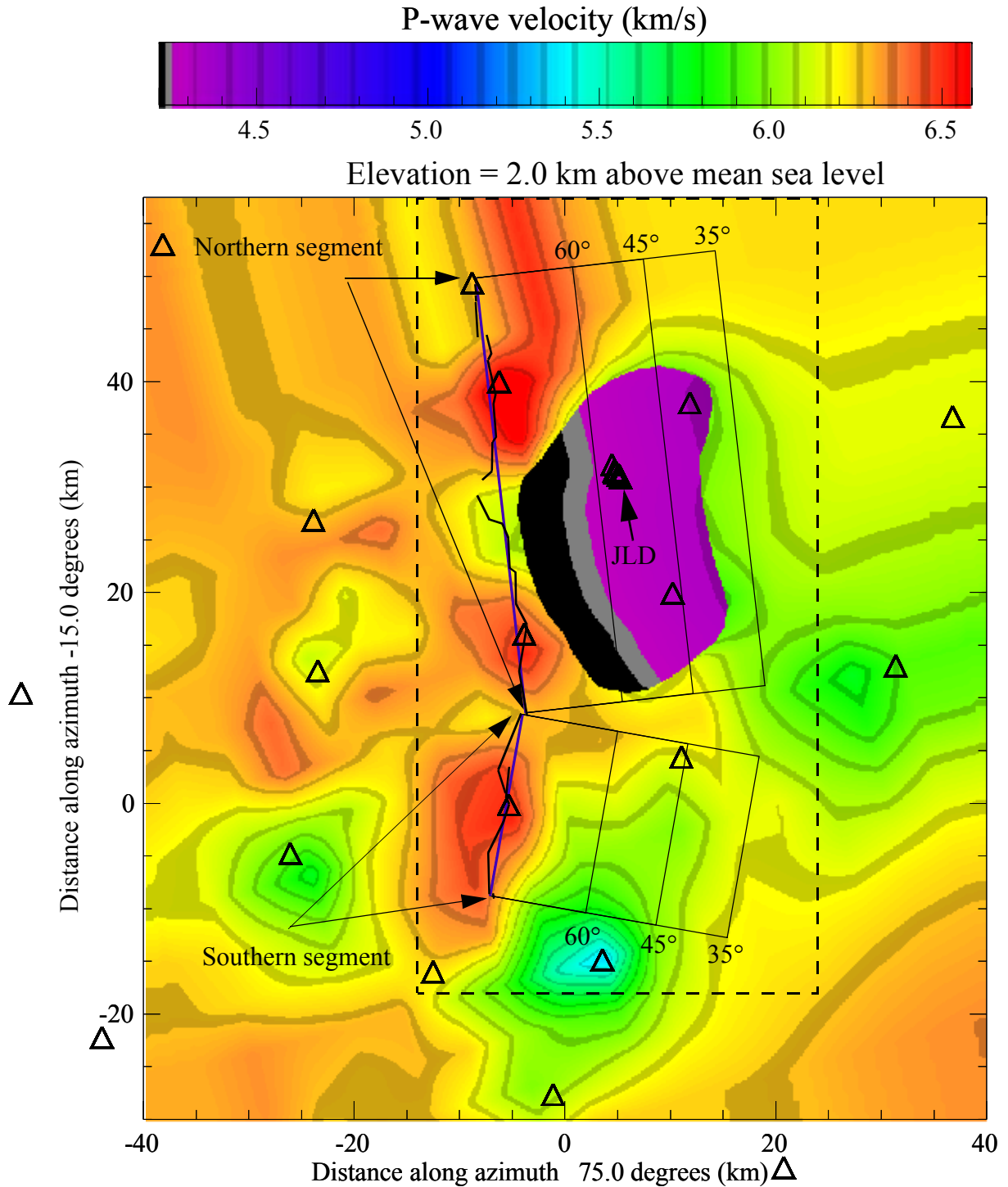


Figure 6-1: Plan view of the ground motion P-wave 3D velocity model at elevation 2 km. Seismographic stations are triangles with the cluster of stations at Jackson Lake Dam as indicated by JLD. Solid rectangles show plan projections of the Teton fault segments for dips as labeled for total fault depths of 16 km. The blue line segments show the approximation to the surface traces of the Teton fault indicated by the irregular solid line segments. Large dashed rectangle shows the limits of the 3D elastic finite-difference grids. Arrows show the limits of the two fault segments considered in ground motion simulations as labeled.

RGFs are mostly used for frequencies < 1 Hz. Empirical Green's functions (EGF) are extracted from site-response recordings of local earthquakes to provide responses > 1 Hz. Point source summation with Kostrov-like slip-velocity time functions is used to compute synthetic ground motion time histories in an approach similar to O'Connell et al. (2001). The nonlinear approach of Bonilla (2001) is used to calculate soil ground motions, including nonlinear soil responses, in low-velocity soils beneath the embankment portion of the dam. Response spectral quantiles are used to associated simulated ground motions with specific probabilities of occurrence and several simulated and observed ground motions time histories are recommended for dynamic analyses of the dam.

6.1.1 Green's Function For Linear Ground Motions. The 3D elastic finite-difference approach of Graves (1996), modified to included viscoelastic responses (Graves and Day, 2003), is applied invoking reciprocity to calculate the primarily < 1 Hz Green's functions on all six fault segments, using a nominal 0.2 km point-source spacing on the faults. This requires specifying a great deal of information about the 3D variations of seismic velocities, density, and attenuation; derivation of these quantities is summarized in Section 4. Site-response recordings of eight local earthquakes are used to construct a suite of empirical Green's functions, primarily for the purposes of synthesizing ground motion responses for frequencies > 1 Hz. The 3D Green's function were used to establish EGF amplitudes for integration points on all fault segments. The details of the preparation of the Green's functions are presented in Section 6.3.

6.1.2 Nonlinear Soil Ground Motions. The seismic responses of near-surface soils often exhibit nonlinear stress-strain relationships. Long-duration ground motions were observed on the embankment section site-response stations located on low (~ 100 m/s) S-wave velocity soils (Section 5). It is necessary to estimate ground motions at sufficient depth to provide linear input ground motions for nonlinear ground motion calculations necessary for engineering analyses of the dam. One option was to input rock motions at the base of the low-velocity soils at ~ 140 m, but the rock motions do not contain the long-durations ground motion responses characteristic of the very-low-velocity (VLV) glacial scour portion of the dam. In Section 5, it was demonstrated that the long-duration soil motions at the surface are likely to originate at $> \sim 25$ m depth due to strong vertical velocity gradients and velocity discontinuities within the low-velocity materials within

the glacial scour. A difficult problem is to accurately represent the seismic responses within the low-velocity soils to include the 3D duration influences of the glacial scour low-velocity structure as inputs into nonlinear soil response calculations, in part, because it is not clear *a priori* at what depth the soil responses behavior becomes significantly nonlinear. A convolution operator developed in Chapter 5 with weak-motion site-response data is used to develop subsurface ground motions for input into nonlinear soil response calculations. Details are presented in Section 6.6.

A second problem is to find a way to propagate the long-duration responses at $> \sim 25$ m depth to the surface that includes likely nonlinear soil responses. The one-dimensional (1D) equivalent-linear method represented by SHAKE (Schnabel et al., 1972) is the most common method for engineering analysis of earthquake ground motions for soil site conditions. However, it is an approximate method that does not have the ability to reproduce some observed classes of nonlinear soil response associated with saturated, low-velocity soils (typical of the soils in portions of the foundation of the embankment portions of Jackson Lake Dam), particularly the sometimes large-amplitude cusped, one-sided accelerograms that arrive behind the first S-waves (Porcella, 1980; Holzer et al., 1989; Zeghal and Elgamal, 1994; Iai et al., 1995; Archuleta, 1998; Bonilla *et al.*, 1998, Frankel et al., 2002). Holzer et al. (1989) reported large-amplitude cusped, one-sided accelerograms in surface seismograms of the 1987 Superstition Hills earthquake recorded on an array of surface and borehole accelerometers and downhole pore-pressure transducers. This site underwent liquefaction during the shaking. Holzer et al. (1989) found that these pulses occurred during drops in the pore pressure and suggested that they were related to episodic lateral spreading. Zeghal and Elgamal (1994) analyzed the same array data and proposed that at large strains after initial liquefaction, the soil became dilatant, pore pressure dropped, and the soil increased in strength, thus producing the cusped pulses. Strain hardening from soil dilatancy has also been observed in laboratory studies (Ishihara, 1985; Kramer and Arduino, 1999). Frankel et al. (2002) note that the cusped arrivals observed from the **M** 6.8 2001 Nisqually earthquake that arrived after the S-waves sometimes actually increased the peak accelerations relative to the peak accelerations associated with the S waves. In some cases, the nonlinear response increases the peak accelerations compared with the linear response, an observation contrary to conventional wisdom on nonlinear response.

To date no one has published results using SHAKE that reproduce the nonlinear behavior discussed above. In view of the inability of SHAKE (Schnabel et al., 1972) to reproduce observed nonlinear soil responses associated with site conditions similar to site conditions at Jackson Lake Dam (Archuleta, 1998), the NOAH nonlinear code (Bonilla et al., 1998; Bonilla, 2000) is also used to estimate ground motions as a function of depth below the portion of the embankment with ~140 m total thickness of soil deposits above the overcompacted till. NOAH is a NOnlinear Anelastic Hysteretic finite difference code, which computes the nonlinear wave propagation in water saturated soil deposits subjected to vertically incident SH ground motion. The constitutive equation implemented in this code corresponds to the strain space multishear mechanism model developed by Towhata and Ishihara (1985) and Iai et al. (1990). The code is able to perform total and effective stress analyses. The current rheology works particularly well to model the cyclic mobility of sands under undrained conditions. Results of these investigations are summarized in Section 6.6 and Appendices E and F.

6.2 Source Parameterization

A kinematic rupture model is used that mimics the spontaneous dynamic rupture behavior of a self-similar stress distribution model of Andrews and Boatwright (1998). The kinematic rupture model is also similar to the rupture model of Herrero and Benard (1994). Self-similar effective stresses (and slip velocities) are generated over the fault with rise times that are inversely proportional to effective stress. Peak rupture slip velocities evolve from ratios of one relative to the sliding (or healing peak) slip velocity at the hypocenter to a maximum ratio of 4:1 consistent with the dynamic rupture results of Andrews and Boatwright (1998) that shows a subdued Kostrov-like growth of peak slip velocities as rupture grows over a fault. The kinematic model used here produces slip models with $1/k^2$ (k is wavenumber) distributions consistent with estimates of earthquake slip distributions (Somerville *et al.*, 1999) and ω^2 (ω is angular frequency) displacement spectra in the far-field. Oglesby and Day (2002) used numerical simulations of dynamic fault rupture to show that rupture velocity, rise time, and slip are associated with fault strength and stress drop, as well as each other. The kinematic rupture model used here enforces correlations between these parameters by using a common fractal seed to specify relationships between all these fault rupture parameters, as discussed in more detail in Section 7.2 in relation to modeling of near-source ground motions from the 1994 M 6.7

Northridge, California, earthquake and in O'Connell et al. (2001). Oglesby and Day (2002) and Guatteri et al. (2003) used dynamic rupture simulations to demonstrate that rupture parameter correlation, as implemented in the stochastic kinematic rupture model outlined here, is necessary to produce realistic source parameters for ground motion estimation.

To calculate peak slip velocities, healing slip velocities, and displacements for moment calculations, we used the approximation of the Kostrov slip-velocity function of O'Connell and Ake (1995)

$$\begin{aligned} \dot{s}(r, t) \approx & C(v_r, \alpha, \beta) \frac{\sigma_E}{\mu} \beta A (H(t - T_{initial}) - H(t - T_{heal})) \\ & \left(0.7 \exp\left(-\frac{t}{(0.9a)}\right) + 0.15 \exp\left(-\frac{t}{(0.4b)}\right) + 0.15 \exp\left(-\frac{t}{(0.8b)}\right) \right) \\ & \left. \frac{-(t - T_{stop})}{h} [H(t - T_{stop}) - H(t - (T_{heal}))] + H(t - T_{initial}) - H(t - T_{heal}) \right) \end{aligned} \quad (6-1)$$

in the kinematic rupture code, where r is the distance on the fault from the hypocenter, α is the compressional velocity, β is the shear velocity, μ is the rigidity, σ_E is the effective stress, $C(v_r, \alpha, \beta)$ is a number determined from v_r , the rupture velocity, and α/β (Dahlen, 1974; Richards; 1976), H is the Heaviside step function, t is time of rupture, $T_{initial}$ is the time of rupture initiation, T_{heal} is the time the rupture begins to stop, and T_{stop} is the time rupture ceases. A is an amplitude factor calculated from the Kostrov slip-velocity function of Archuleta and Hartzell (1981) at dt after $T_{initial}$ that allows (6-1) to replicate the Kostrov slip-velocity function, and a , b , and c , are times from the onset of rupture until the slip velocity reaches, 0.5, 0.1, and 0.05 of the difference between peak slip-velocity amplitudes and steady slip-velocity amplitudes, respectively. Equation (6-1) was normalized over the entire fault to produce a maximum ratio of peak rupture slip velocity to peak healing slip velocity of 3:1. The approximation to $C(v_r, \alpha, \beta)$ of O'Connell and Ake (1995)

$$C(v_r, \alpha, \beta) = 0.446437 + 0.707423 v_r - 0.151251 \frac{\alpha}{\beta} \quad (6-2)$$

was used in (6-1). It has a maximum error of less than 2% relative to the results of Dahlen (1974) and Richards (1976). Guatteri et al. (2003) showed with dynamic rupture simulations that

Kostrov-like slip-velocity functions provide the most-realistic slip-velocity functions for ground motion estimation.

The time domain Kostrov slip velocity function of Archuleta and Hartzell (1981)

$$\dot{s}(r, t) = C(v_r, \alpha, \beta) \frac{\sigma_E}{\mu} \beta t \frac{H\left(t - \frac{r}{v}\right)}{\sqrt{t^2 - r^2/v^2}} \quad (6-3)$$

was convolved with the 3D Green's functions to produce the < 1 Hz synthetic ground motions. The EGF summations required 16 times more integration points than the RGF summations to ensure integral convergence, resulting in > 400,000 point source integrations to calculate for each single ground motion. To eliminate the slip-velocity convolutions from inside the point source summation integral, an approximate "Kostrov" function was convolved after the EGF point-source summation to approximate the amplitude and phase effects of the a Kostrov slip velocity functions. The high-frequency approximation to the Kostrov function was constructed by extracting the portion of the Kostrov function that produces the deviation of the Kostrov function from a boxcar function (Figure 6-2a), and convolving that "residual function" (Figure 6-2b) with the EGF synthetic ground motions. This produces a high-frequency decay similar to using the exact Kostrov function (Figure 6-2c), but does not to account for variation in Kostrov slip velocity behavior as a function of rupture time. This approach is more accurate than other methods of high-frequency summation methods, like stochastic subevent summation used by Silva and Lee (1987), Schneider et al. (1993), Zeng et al. (1994), and Beresnev and Atkinson (1997), because it employs a rigorous point-source integration accuracy of 6 points-per-shortest-wavelength (Spudich and Archuleta, 1987), but is less accurate than retaining the slip-velocity function convolution at each integration point.

Effective stress correlation lengths were increased by 33% relative to the **M** 6.7 Northridge rupture simulations of O'Connell (2001) to be consistent with the empirical relations of Somerville et al. (1999), that indicate that asperity size increases with magnitude. Rupture velocities were allowed to vary over a wide range (between 0.6β to 1.05β) in each rupture simulation to allow rupture directivity caustics to develop, and to produce variable rupture times.

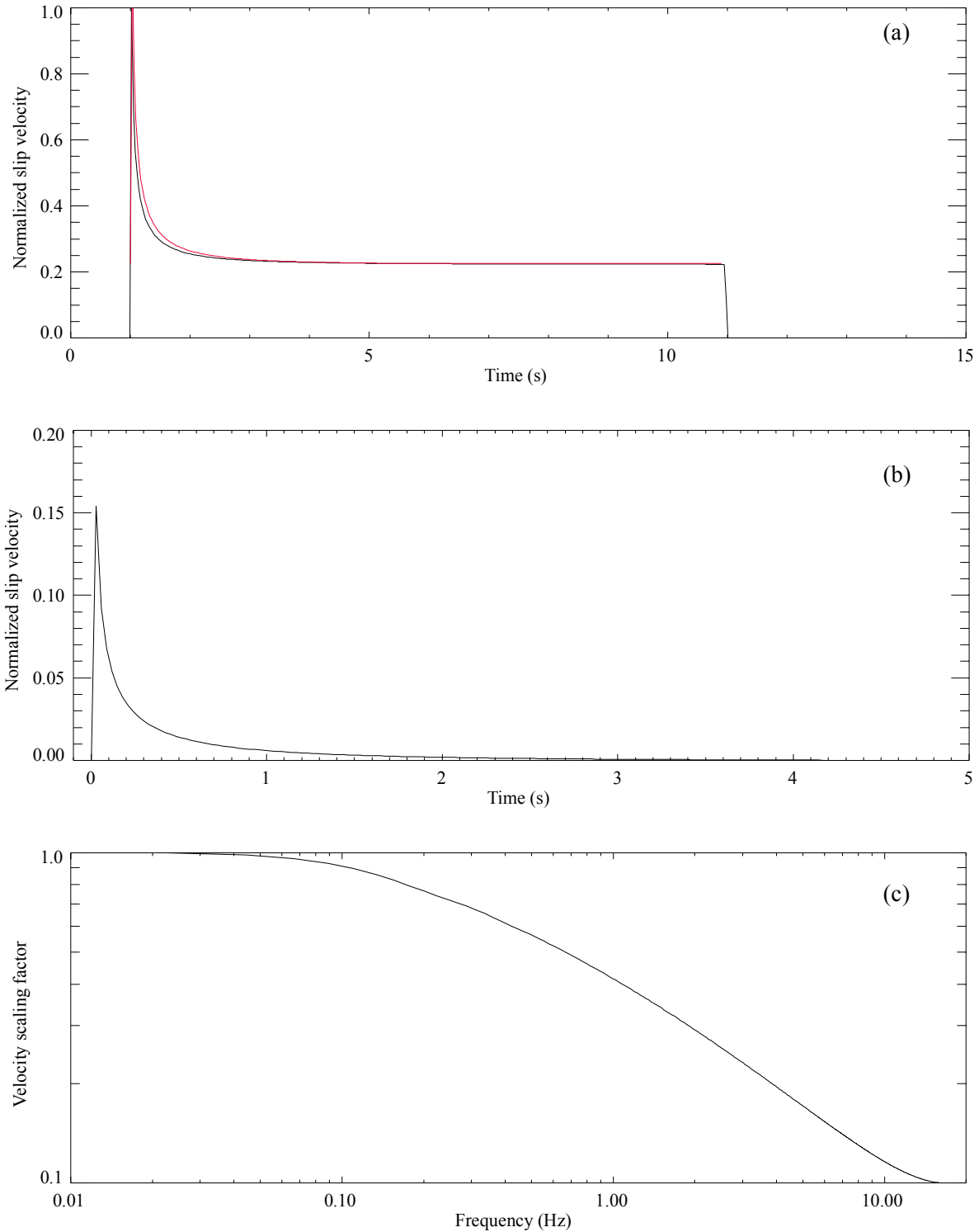


Figure 6-2: High-frequency approximation to the Kostrov slip-velocity function. (a) Exact Kostrov slip-velocity function for a rupture time of 1 s and duration of 10 s is the black curve and the red curve is the portion of the slip-velocity function extracted and rescaled to unit amplitude at a frequency of 0.022 Hz and plotted in (b). (c) Ground velocity scaling factor as a function of frequency obtained from (b).

Effective stresses averaged 30-40 bars, consistent with stress drops typically associated with normal-faulting earthquakes (McGarr, 1984; Mendoza and Hartzell, 1988; Anderson et al., 2001).

A large number of assumptions and choices must be made to specify earthquake rupture models. This discussion focuses on significant assumptions made in this study:

1. The radiation pattern is applied at all frequencies. As discussed in O'Connell and Ake (2002), the high frequency limits of coherent seismic radiation are not well established. There are theoretical reasons to expect seismic radiation to become incoherent at sufficiently high frequencies as a result of dynamic rupture processes (Madariaga, 1977; Boatwright, 1982). The scattering properties of crustal velocity heterogeneity also contribute to reducing high-frequency coherence (O'Connell, 1999a). The crustal wave propagation filter is sufficiently strong to make it impossible to determine the source limits of coherent seismic radiation from surface ground motion observations. Abercrombie (1995) showed that the top several km of the crust severely attenuate high-frequencies and that downhole earthquake recordings show that earthquake source processes are self-similar. Since coherence at the site persists to at least 4 Hz, and possible to 6 Hz (Section 4), it is prudent to apply the radiation pattern for all frequencies.
2. A total of eight EGF's are used in the simulations (Appendix D). In this study phase is not spatially interpolated between EGF's, as suggested by Hutchings (1994). Since phase is not randomized beyond phase variability contained in the eight distinct EGF's, phase is less coherent than the approach of Hutchings (1994). The random selection of one of the eight EGF's at each point-source positions and the considerably variable initial phases of the direct S-waves in the EGF's suggests that phase may be overly randomized in the EGF ground motion simulations for low frequencies. Conversely, the random selection of EGF's at each point-source position is effectively a proxy for randomizing the phase of high-frequencies, e.g., reducing the coherence of the effective radiation pattern for all frequencies.
3. Rupture velocity is assumed to not exceed $1.105*\beta$. As discussed in O'Connell and Ake (2003), there are a number of earthquakes where rupture velocity may have reached $\sim 1.4*\beta$ and there are theoretical reasons to expect high rupture velocities in some situations (Ben-

Zion, 2001). A significant caveat is that there are no dynamic investigations of rupture velocities and systematic velocity contrasts across faults for dipping faults have been performed (Ben-Zion, 2001; O'Connell and Ake, 2003). So the arguments presented below w.r.t. high rupture velocities on the Teton fault are by analogy to strike-slip simulations (summarized in Ben-Zion, 2001) and observations (Bouchon et al., 2001).

Rupture velocities $\sim 1.4\beta$ on the Teton fault are not likely to occur for the following reasons:

1. Rupture is likely to propagate from near the bottom of the fault to the surface, in the opposite direction to the normal-slip direction of the hanging wall. The 3D velocity inversion shows a slight decrease of P-wave velocity from the footwall to the hanging wall below 5 km depth (admittedly, the resolution of this velocity change is marginal, at best). Thus, slip direction and rupture direction are the same for the stiffer side of the fault and supershear rupture velocities of $\sim 1.4\beta$ are unlikely for depths > 5 km (by appealing to strike-slip results summarized in Ben-Zion, 2001).
2. Oglesby et al. (1998) present dynamic rupture simulations that show that slip may jump to the free surface and propagate downdip to intersect the primary updip rupture front. This results was reproduced using the approach of Andrews (1999). In this case, rupture is coincident with the slip direction of the hanging wall. However, the gravity modeling summarized in Byrd et al. (1994 and references therein) and velocity structure modeling in Section 4 suggest that a high-density body is located in the hanging wall between the fault and the LVB. Consequently, the compliant material is on the footwall and is not moving in the direction of rupture for downdip rupture; supershear rupture velocities of $\sim 1.4V_s$ are unlikely for this configuration (Ben-Zion, 2001).

There is a possible exception that would allow for rupture velocities of $\sim 1.4\beta$ on a portion of the Teton fault. Updip rupture and footwall slip direction are parallel for the top several km of the fault, so supershear rupture velocities of $\sim 1.4\beta$ are not precluded in this region (Ben-Zion, 2001). However, the velocity contrast across the fault in the top 5 km may be insufficient to allow supershear rupture velocities of $\sim 1.4V_s$. Without dynamic rupture simulations using the fault geometries of the Teton fault in a realistic 3D moduli structure, it is unclear what various rupture

velocity scenarios are likely or unlikely. This is an issue that could significantly influence ground motions at Jackson Lake Dam and may merit further investigation.

6.3 Linear Wave Propagation Methods

This section provides details of the application of the viscoelastic 3D finite difference methods of Graves and Day (2003) and P.C. Liu (pers. comm.) to calculate ground motions for frequencies < 1 Hz, and construction of empirical Green's functions for simulated ground motions for frequencies > 1 Hz.

6.3.1 Low-Frequency 3D Green's Functions. In Section 4, a finite 3D grid of velocities, densities, and attenuation coefficients that contains the Teton fault segments, the dam, and sufficient distance from the grid boundaries to minimize artificial boundary effects was constructed using available geophysical data. In Figure 6-3 representative cross-sections show the positions of the Teton fault for the three discrete dips used in ground motions simulations. As discussed in Section 4, there are significant caveats concerning the velocity model, particularly the LVB that contains the dam. First, while the strong velocity contrast between the LVB and the surrounding medium reproduce overall amplitude and duration characteristics of MEQ ground motions recorded at the dam, the eastern extent of the LVB is artificially truncated, based on the refraction travel-time data. The overall shape and roughness of the bottom of the LVB are not well constrained by the data analyzed to date. The 2D finite-difference modeling suggested that strong correlated-random velocity variations may exist in the LVB, but the velocity model used here (Figures 6-1 and 6-3, Appendix C) has no randomization of LVB velocities. The only velocity randomization was applied to the medium outside the LVB in the form of vertical velocity oscillations with wavelengths of ~ 1 km that are strongest in the highest velocity gradient portions of the model (Figure 6-3). More sophisticated randomizations (O'Connell, 1999a) could significantly change predicted ground motions, but would entail a significantly expanded scope of investigation. Since as is shown in Section 6.4, the LVB strongly influences peak ground motion scaling and durations at the dam, the uncertainty in the 3D velocity-model may be an important source of ground motion estimation uncertainty at the dam. To better characterize ground motion estimation uncertainties, several alternative ground motion estimation approaches that use purely empirical Green's functions are presented and used in Section 7.

6.3.1.1 Viscoelastic 3D Finite-Difference Calculations. Viscoelastic 3D finite difference methods are used for forward-modeling ground simulations of single and multiple segment finite-fault rupture of the Teton fault using the method of P.C. Liu (pers. comm). The approach of Graves and Wald (2001), updated as per Graves and Day (2003) to provide a more realistic approximation for damping, was used to calculate reciprocity Green's functions for grids of point sources distributed on the six fault segments used to evaluate ground motions associated with earthquakes on the Teton fault.

Reciprocity Green's function were obtained for the south abutment of Jackson Lake Dam by calculating the moment tensor responses at 93,485 point-source positions distributed across the six Teton fault segment scenarios for each ground motion component, yielding 280,455 Green's function files. The nominal point-source spacing along strike and downdip was 0.2 km, but deviates slightly from 0.2 km, because point-source positions coordinates are rounded to the nearest integer node position in the reciprocity calculations. The forward-modeling code interpolates precisely between nodes to enforce a 0.2 km point-source spacing along strike and down dip. The maximum frequency before velocity dispersion begins to influence calculated responses is 0.8-1.0 Hz using these node spacings. Consequently, the 3D finite-difference results were low-pass filtered using a two-pole Butterworth filter with a corner frequency of 0.8 Hz to smoothly attenuate high-frequency responses prior to blending with EGF ground motions, as described below. This filter reduced 1.0 Hz amplitudes by half, making 1.0 Hz the cross-over frequency for blending high- and low-frequency synthetic ground motions. A time step of 0.0015 s was used to meet explicit stability requirements. After anti-alias filtering, computed responses were saved every 0.015 s. The anti-alias filter was applied to the source time function, a Gaussian velocity pulse, to improve computational efficiency. The anti-alias filter and Gaussian source-time function responses were deconvolved from the reciprocity Green's function in preparation for the imposition of Kostrov-like source time functions for ground motion synthesis.

6.3.2 High-Frequency Empirical Green's Functions. In theory there is no reason the $M < 3$ EGF's could not be used to produce broadband ground motions. In practice, ambient background noise precludes using the EGF's for frequencies substantially < 1 Hz. A total of eight MEQ three-component seismograms obtained from site-response stations in the vicinity of

Jackson Lake Dam were used to produce EGF's for ground motion simulations corresponding to earthquake ruptures on the northern Teton fault segment (Figure 6-4, Table 6-1). Seven

Table 6-1: Empirical Green's Function Earthquake Information

Date.	Time.	Latitude.	Longitude.	Elevation.	Magnitude.
1996/09/29	00:35:59.471	43.91073	-110.64070	-3.720	1.6
1996/10/15	22:03:12.602	43.89276	-110.67271	-8.050	2.0
1996/11/28	09:56:56.902	44.00331	-110.54839	-7.230	2.2
1997/02/06	18:56: 7.464	43.70396	-110.43253	-4.830	2.2
1997/09/11	04:11:18.022	43.93142	-110.56208	-6.550	2.0
2001/04/19	03:28:19.000	43.82266	-110.69444	-1.870	1.4
2001/11/15	02:16:10.000	43.68424	-110.49812	-2.870	2.9
2001/12/06	14:15:14.000	43.82436	-110.82595	-7.890	2.2

seismograms were obtained from station JLDW, located on the south abutment of the dam. One seismogram was obtained from station JLD7 located on the northern end of the dam because the seismograms from stations JLDW and JLD2 were dominated by noise. These earthquakes were selected because of their proximity to the northern segment of the Teton fault. Several of the earthquakes conceivably are located on the Teton fault; the uncertainties in fault dip and hypocenter locations precludes definitive assignment of these earthquakes to the Teton fault.

The mean spectral velocity responses of the 3D reciprocity Green's functions in the ~0.8 Hz to 1.5 Hz frequency band were used to establish EGF scaling for integration points on all fault segments. Although the strict grid dispersion limit for the 3D RGFs was about 1 Hz (Moczo et al., 2000), the realities of EGFs signal-to-noise as a function of frequency required calculating mean amplitudes in the ~0.8 Hz to 1.5 Hz frequency band. Rigorously extending the 3D RGF calculations to 2 Hz would have required 8 times more memory and storage, and 16 times more computer time (about 2 months), and was not feasible within the project schedule. The approach used was probably the most accurate approximation available; alternative 1D wave methods including reflectivity approaches were considered, but would have produce larger errors. Further calibrations of estimated ground motion amplitudes using purely empirical Green's functions are presented in

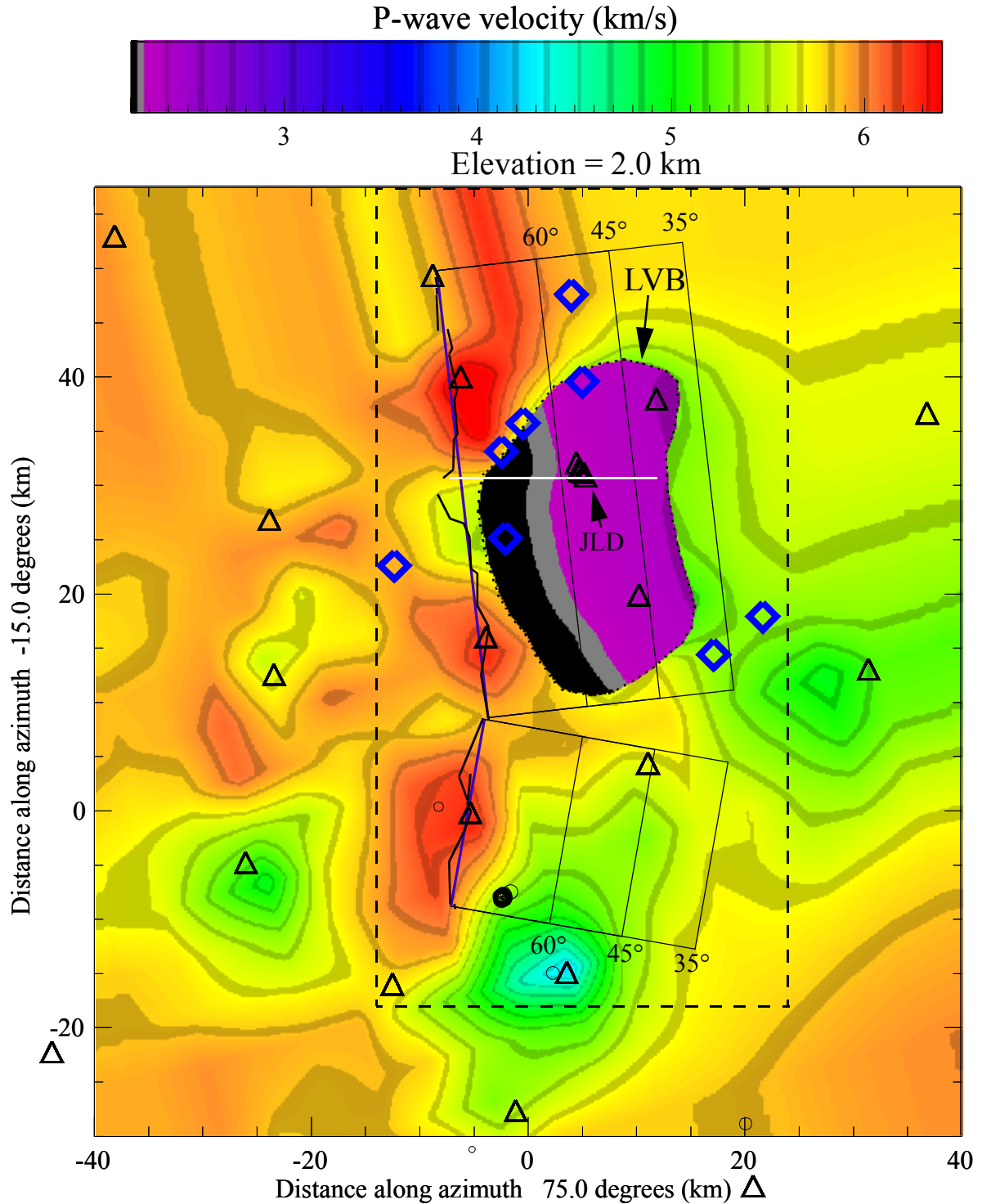


Figure 6-4: Epicenters of the EGFs with P-wave 3D velocity model at elevation 2 km. Blue diamonds are EGF epicenters. Seismographic stations are triangles with the cluster of site-response stations at Jackson Lake Dam indicated as JLD. Solid rectangles are plan projections of the Teton fault segments for dips as labeled. Blue line segments show approximations to the surface traces of the Teton fault (irregular solid line segments). Large dashed rectangle shows the limits of the 3D elastic finite-difference grids. Closed dotted curve labeled LVB denotes the limits of the LVB and circles are event epicenters. The white line shows ground motion profiles in Figs. 6-8 to 6-15.

Section 7 to better ascertain ground motion the significance of theoretical Green's function assumptions on ground motion uncertainties.

The amplitude and polarity plots in Figures 6-5 to 6-7 provide insights into the factors that most strongly influence ground motion amplitudes at the dam. For E15S horizontal motions, large slip-velocities on the upper half of the fault within a ~15 km strike distance region centered on the dam produce ground velocities at the dam 3 to 6 times stronger than slip-velocities on the rest of the upper half of the fault (Figure 6-5). The polarities of the largest contributors to ground velocity at the dam have mixed S-wave polarities, which generally reduces amplitudes associated with directivity, although the dam is located too far east of the fault to experience the strongest directivity effects (see Section 6.4). The polarity variability is a product of a simple radiation pattern effect where the polarity changes at ~15 km downdip distance. S-wave propagation complexity accounts for the varying polarities at downdip distance < 10 km; S-wave interacts with the 3D LVB make polarity identification ambiguous and may produce phases shifts sufficient to switch first S-wave arrival polarities. Slip-velocities in the ~20 km strike distance region centered on the lower half of the fault produce ground velocities at the dam ~2 times stronger than slip-velocities on the rest of the lower half of the fault (Figure 6-5). For the dam to experience decreased E15S ground motion velocities, would require that no high slip-velocity asperities occur in the central half of the northern rupture segment. Somerville et al. (1999) obtained relations between seismic moment and asperities radius. Using there relation for a **M** 7.0 earthquake on the northern Teton fault segments, indicates that the largest asperity would have diameters of ~11-15 km. Somerville et al. (1999) found that the location of the centers of asperities for dip slip faults were located within the central 80% of fault strike about 86% of the time. Asperities centered 20% or 80% of the strike distance would have nearly half of their asperity areas intersecting the regions of elevated amplitude contribution in Figure 6-5. Thus, it is likely (> 86%) that at least half or more of the area of the largest asperity on the northern Teton fault segment will occur on the portions of the fault that produce the strongest E15S ground shaking.

The situation is more complex for the N15E horizontal component (Figure 6-6); the polarities switch along strike centered on the strike position of JLDW and the radiation pattern produces a

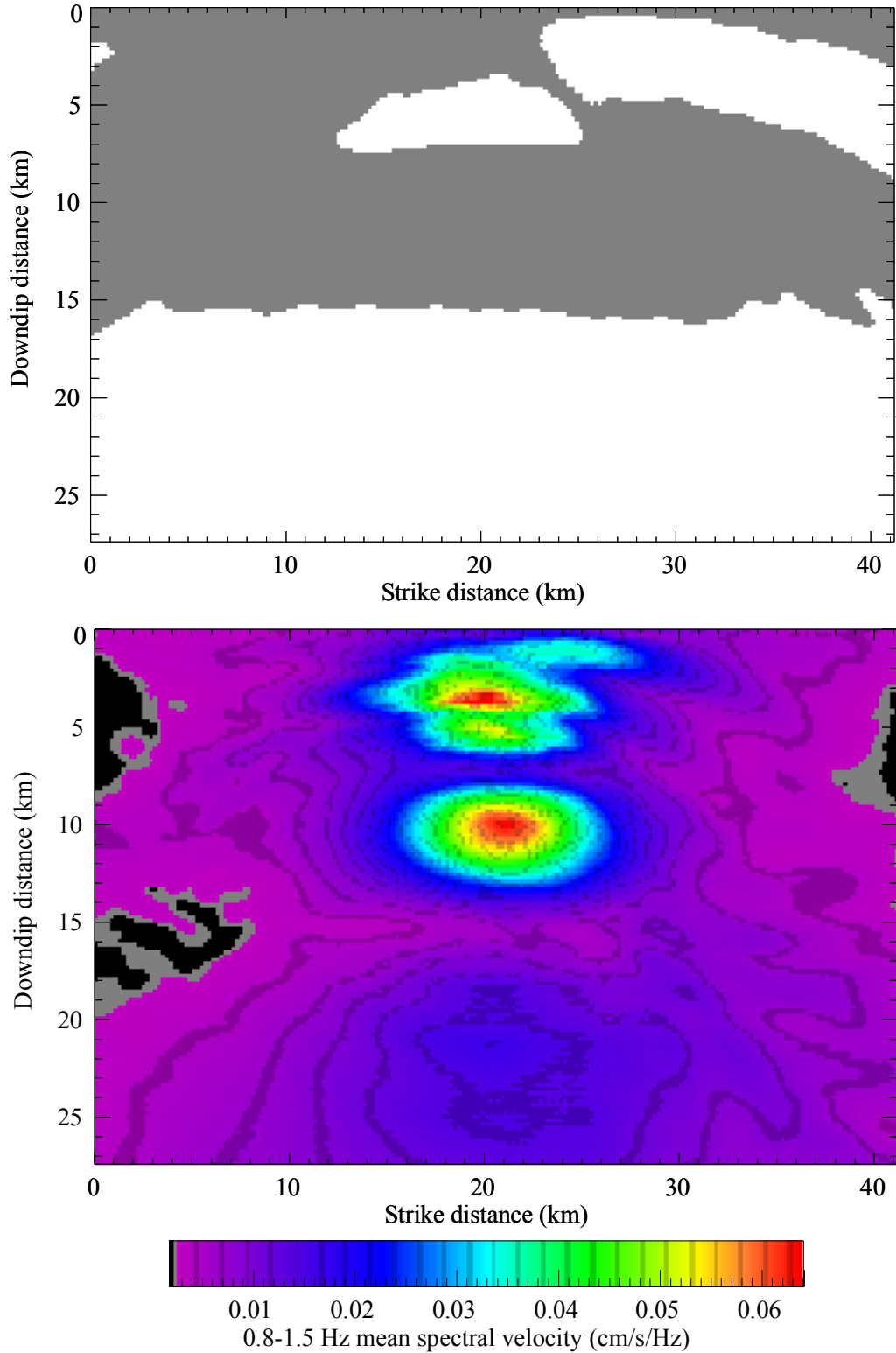


Figure 6-5: E15S-component S-wave normal-dip-slip polarities and 0.8-1.5 Hz amplitudes at JLDW for a 35° fault dip. Perspective is normal to the fault surface. Polarity is shown at the top with grey positive and white negative. RGF mean spectral amplitudes are color contoured with the color bar showing the amplitude range. Point source spacing is 0.2 km. JLDW's strike position is ~21 km.

nearly quadrupole amplitude variation about the position of the normal on the fault to JLDW. It appears that the LVB substantially amplifies N15E ground motions associated with seismic radiation from the shallow portion of the fault located in the ~10 km portion of the fault south of the JLDW. Again the central half of the fault produces the largest ground motion amplification at the dam, similar to the E15S component (Figure 6-5), except there are near nulls associated with the quadrupole radiation pattern in the center of the fault (Figure 6-6). Thus, the N15E motions are also likely (>86%) to be amplified by the largest rupture asperity, in a manner similar to the E15S component. The polarities for the vertical S-wave contributions are complex and the strongest contributions to vertical motions are confined to the upper half of the fault (Figure 6-7). Consequently, if most of the largest asperity were located on the lower half of the fault, vertical ground velocities at JLDW would be lower than for either of the horizontal components.

The polarity complexities in Figures 6-5 to 6-7 ensure that realistic radiation patterns are used when summing the EGF. Vidale (1989) showed that the standard double-couple radiation pattern is observable to 6 Hz based on analysis of the mainshock and an aftershock from the Whittier Narrows, California, thrust-faulting earthquake sequence. In contrast, Liu and Helmberger (1985) found that a double-couple radiation pattern was only discernible for frequencies extending to 1 Hz based on analysis the 1979 Imperial Valley earthquake and an aftershock. Since it was possible to model MEQ S-waves to at least 4 Hz in Section 4, it is more appropriate to include the radiation pattern explicitly in the EGF summations, than to assume random polarities at frequencies > 1 Hz. Consequently, polarity-corrected EGFs are likely more realistic for frequencies extend to 4-6 Hz than assuming random polarities EGFs (e.g., stochastic subevent summation as used by Silva and Lee, 1987; Schneider et al., 1993; Zeng et al., 1994; Beresnev and Atkinson; 1997).

Several processing steps were required to convert the seismograms to EGF's. First, the S-wave arrival times were picked to provide a time reference for the finite-fault summations. Also, the polarities of the initial S-wave arrivals were picked and the seismograms normalized to have positive initial polarities on all components prior to application of the radiation pattern polarities. The radiation pattern polarities and overall amplitude scaling were obtained by using the mean ~0.8 Hz to 1.5 Hz spectral amplitudes from the 3D Green's functions distributed over the fault surfaces (remember we have three fault dips to consider for the northern segment) to scale the

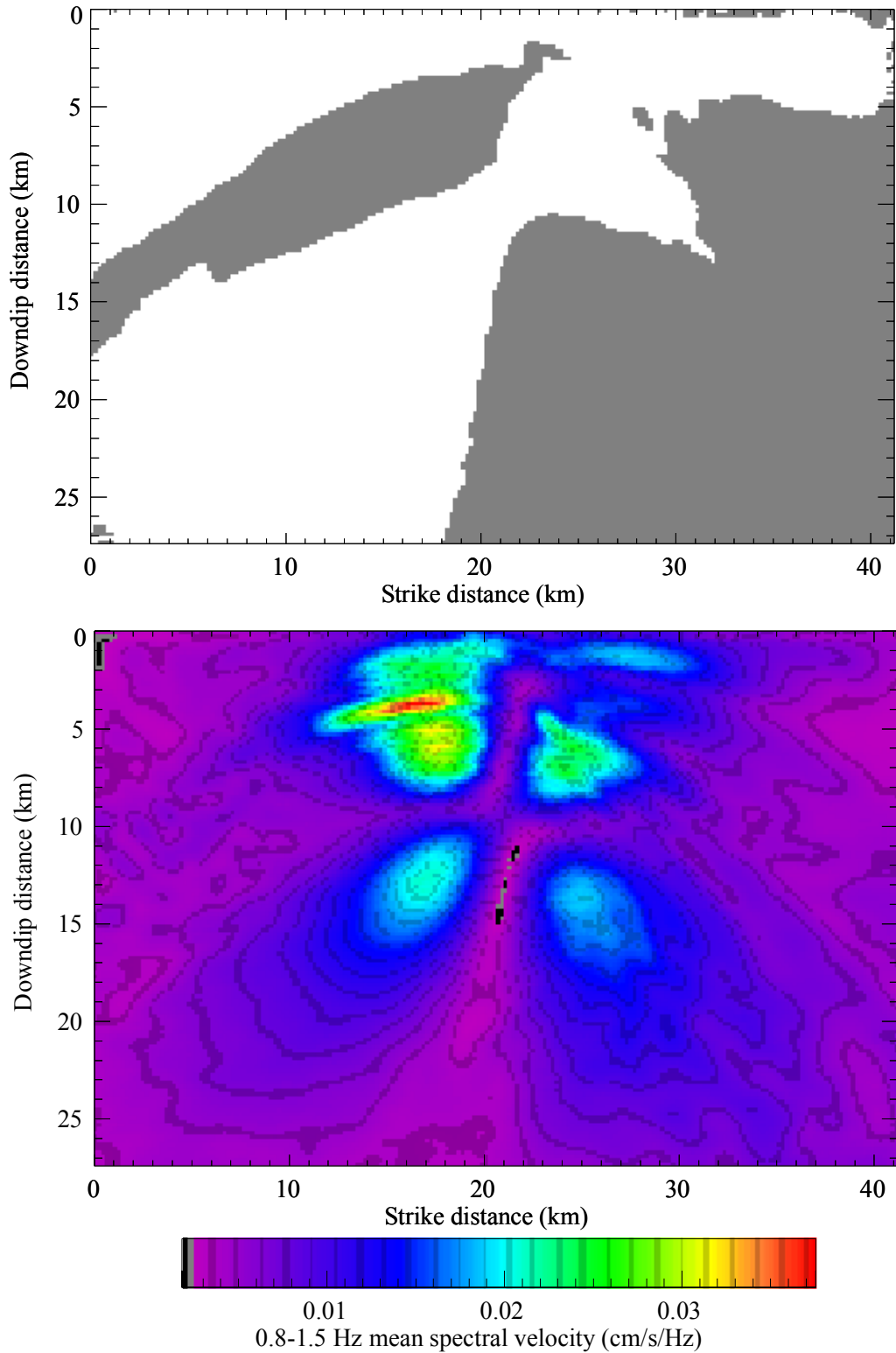


Figure 6-6: N15E-component S-wave normal-dip-slip polarities and 0.8-1.5 Hz amplitudes at JLDW for a 35° fault dip. Perspective is normal to the fault surface. Polarity is shown at the top with grey positive and white negative. RGF mean spectral amplitudes are color contoured with the color bar showing the amplitude range. Point source spacing is 0.2 km. JLDW's strike position is ~21 km.

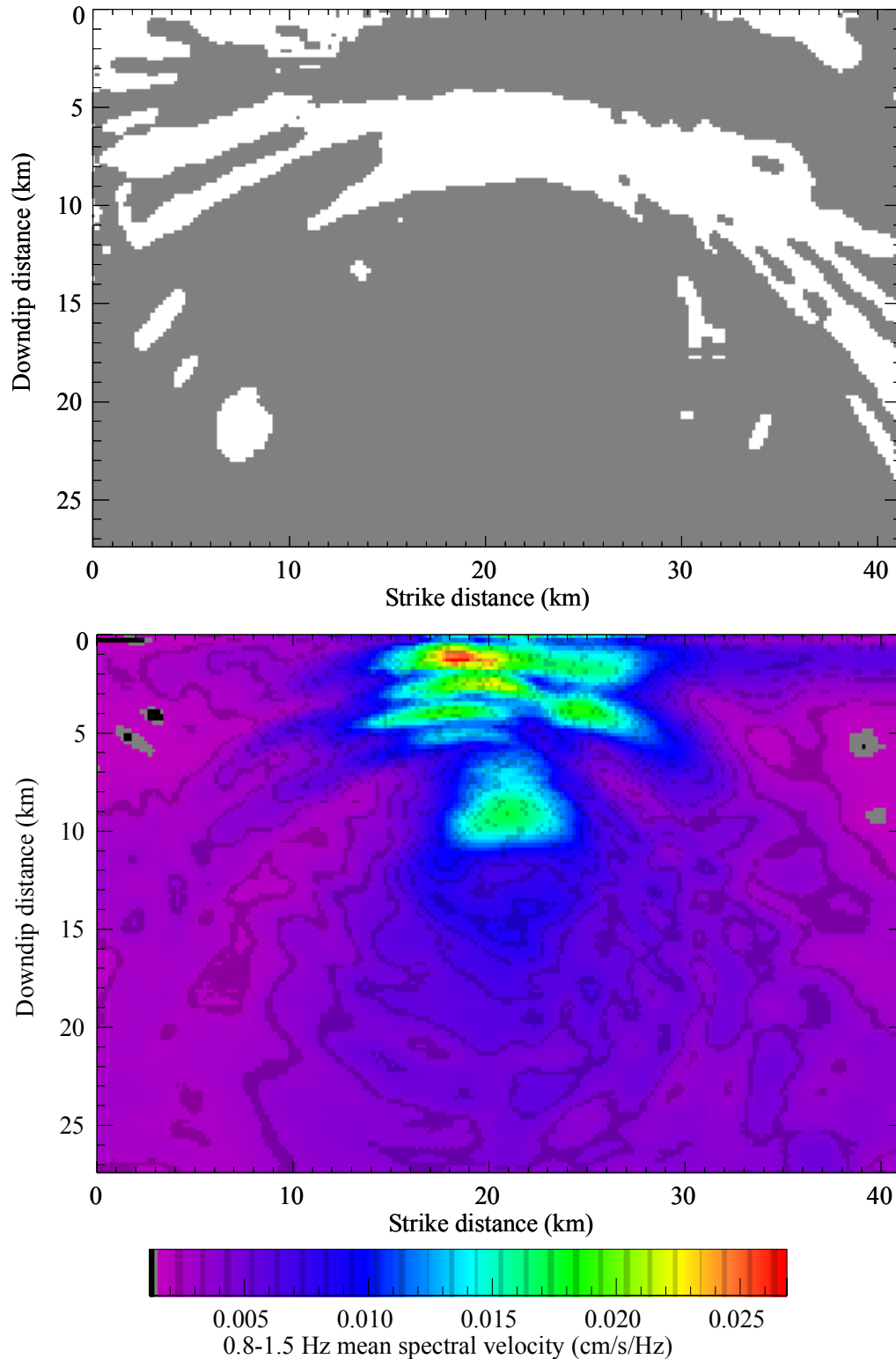


Figure 6-7: Vertical-component S-wave normal-dip-slip polarities and 0.8-1.5 Hz amplitudes at JLDW for a 35° fault dip. Perspective is normal to the fault surface. Polarity is shown at the top with grey positive and white negative. RGF mean spectral amplitudes are color contoured with the color bar showing the amplitude range. Point source spacing is 0.2 km. JLDW's strike position is ~21 km.

EGF's. The 3D eikonal equation solver of Hole and Zelt (1995) was used to calculate first S-wave arrival times and the polarities of the 3D Green's function were estimated by extracting the signs of the integrals over 0.4 s of each component of the 3D Green's function starting at the computed S-wave arrival time. A median smoother was applied to the polarities obtained over fault surface to obtain the polarities used in the EGF calculations. EGFs were constructed of total lengths of 15 s to ensure ground motion calculations could be accomplished on a reasonable project schedule. The 15 s EGFs, consisted of about 1.5 s of pre-S-wave and ~13.5 s of post S-wave ground motions. The ~1.5 s of ground motion preceding the first S-wave was included to capture any significant converted phases that had apparent velocities similar to the first S-wave arrival. All EGF's are presented in Appendix D.

A point-source integration interval of 0.05 km was used in the EGF ground motion simulations to ensure a sampling of at least 6 points per wavelength for frequencies < 10 Hz and rupture velocities of ~3 km/s. To achieve this, the polarity and amplitude factors from the 3D Green's functions were bilinearly interpolated onto the integration grid.

To approximate the influence of a Kostrov-like slip velocity function while avoiding the computational demands of performing slip-velocity function convolutions at every integration point, a modification of the isochrone approach of O'Connell and Ake (2003) was used. The "residual" Kostrov-like slip-velocity function that represented the most "typical" Kostrov slip-velocity function in terms of rise-time documented in Section 6.2 was convolved with the ground motions after point-source summation. This produces an appropriate ground motion scaling (e.g., ω^2 displacement spectral rolloff), but is not as accurate as convolving the Kostrov slip-velocity functions at each integrating point on the fault. However, it reduces the computational burden by factors of $\sim 10^3$ and makes simulations of many ground motion scenarios possible. Uncertainties in the application of the Kostrov slip-velocity functions introduce uncertainties, more accurately potential biases, in the high-frequency acceleration amplitudes of 10% to 30%. This is less than the uncertainty in ground motion synthesis when specifying the distribution of subevent sizes using Brune sources to achieve an ω^2 displacement spectral rolloff (Bereznev and Atkinson, 1997).

6.4 Linear Ground Motion Simulations

The 3D ground motion velocity model presented in Section 4 and shown in Figures 6-1 and 6-3 is used to synthesize all ground motions. The 3D reciprocity Green's functions and empirical Green's functions were used to synthesize ground motions at site JLDW located ~200 m east of the southern end of Jackson Lake Dam to provide reference rock motions. The 3D ground motion S-wave velocity model is also used to calculate S-wave travel times for empirical Green's function ground motions. These synthesized ground motions provide the basis for all rock and soil ground motions recommended for dynamic analyses of the dam.

6.4.1 Idealized Fault Rupture Geometries. The Teton fault consists of numerous, sometimes discontinuous, fault traces (Section 2). For the purposes of ground motion simulations, the Teton fault has been idealized using two planar fault rupture segments. The ~42-km-long northern rupture segment consists of the central and northern sections of the Teton fault as defined in Section 2, approximated by a single planar fault striking N8E with dips of 35°, 45°, or 60°, as shown in Figure 6-1. The ~18-km-long southern rupture segment consists of the southern section of the Teton fault as defined in Section 2, approximated by a single planar fault striking N21E with dips of 35°, 45°, or 60°, as shown in Figure 6-1. Maximum fault depth is 16 km for all dip scenarios and both fault segments as indicated in Figure 6-3. Low-frequency 3D ground motion simulations were used to determine the impact of rupturing both rupture segments in a single earthquake on peak ground motions and durations at the dam (Section 6.4.2.2).

6.4.2 Forward Calculations of Low-Frequency 3D Ground Motions. It is important to calculate ground motions over a significant region in plan view to understand how ground motions vary in space in relation to distance from the Teton fault, and in relation to the 3D crustal velocity structure. Several 3D finite-difference simulations of Teton fault rupture scenarios provided ground motion profiles for sites extending from the footwall of the Teton fault through site JLDW to points just west of the eastern limit of the LVB in Figure 6-4. These calculations were also used to compare ground motions produced by rupture of the entire Teton fault with ground motions produced by rupture of the northern ~42 km of the Teton Fault. These calculations were performed for dips of 35° and 60° to bracket the range of ground motion responses associated with plausible ranges of fault dip. These are by necessity, low-frequency (<

1 Hz) ground motion simulations, so peak velocities, peak accelerations, and Arias intensities are all smaller than would be associated with broadband ground motions.

Ground motions for rupture of the entire Teton fault were constructed by using ground motions produced by rupture from the southern end of the southern segment added to ground motions produced by rupture of the northern segment from its southern edge, with a 1 s rupture delay between the time rupture arrived at the northern end of the southern segment, and when rupture was initiated at the southern end of the northern rupture segment. The horizontal component orientations of the simulated ground motion are 7° from being perfectly aligned parallel (N15E) and normal (E15S), respectively, to the idealized strike of the northern Teton fault rupture segment. For the purposes of discussion the 7° deviation is ignored. Jackson Lake Dam strikes generally north along the northern $\sim 40\%$ of its crest length, but generally has a NNW strike for most of the rest of the dam. For the southern half of the embankment section the N15E horizontal component is more representative of downstream motions than the E15S component, whereas those roles are reversed for the northern embankment section and concrete section.

For a Teton fault dip of 35° the largest peak horizontal velocities (PHV) occur on the fault normal horizontal component for sites about 4.5 km east of the fault (Figure 6-8). The largest PHV does not occur above the deepest portions of the LVB, but occur along the western portion of the LVB, indicating a complex interaction between rupture directivity and LVB structure. The PHVs within the LVB, and at the dam, are larger than PHVs at two of the three rock motions located < 2 km from the Teton fault (Figures 6-8 and 6.9). In contrast, the largest vertical velocities occur adjacent to the Teton fault on the rock portion of the hanging wall (Figure 6-10). The dam experiences larger PHAs and PHVs than rock sites located within 2 km of the Teton fault, but PHAs and PHVs are about $2/3$ of the maximum PHAs and PHVs that occur the western portion of the LVB (Figure 6-11). The dam is located at the edge of a region of elevated Arias Intensity (Figure 6-11) associated with LVB amplification, and the interactions of prolonged ground motions associated with LVB-edge waves and resonant LVB responses with direct S-waves from later portions of the fault rupture. Strong ground velocity pulses nearly comparable in amplitude to the PHVs associated with direct S-waves occur about 8 s after the first S-wave arrival at the dam (dashed lines in Figures 6-8 and 6-9). These arrivals have apparent velocities indicating that

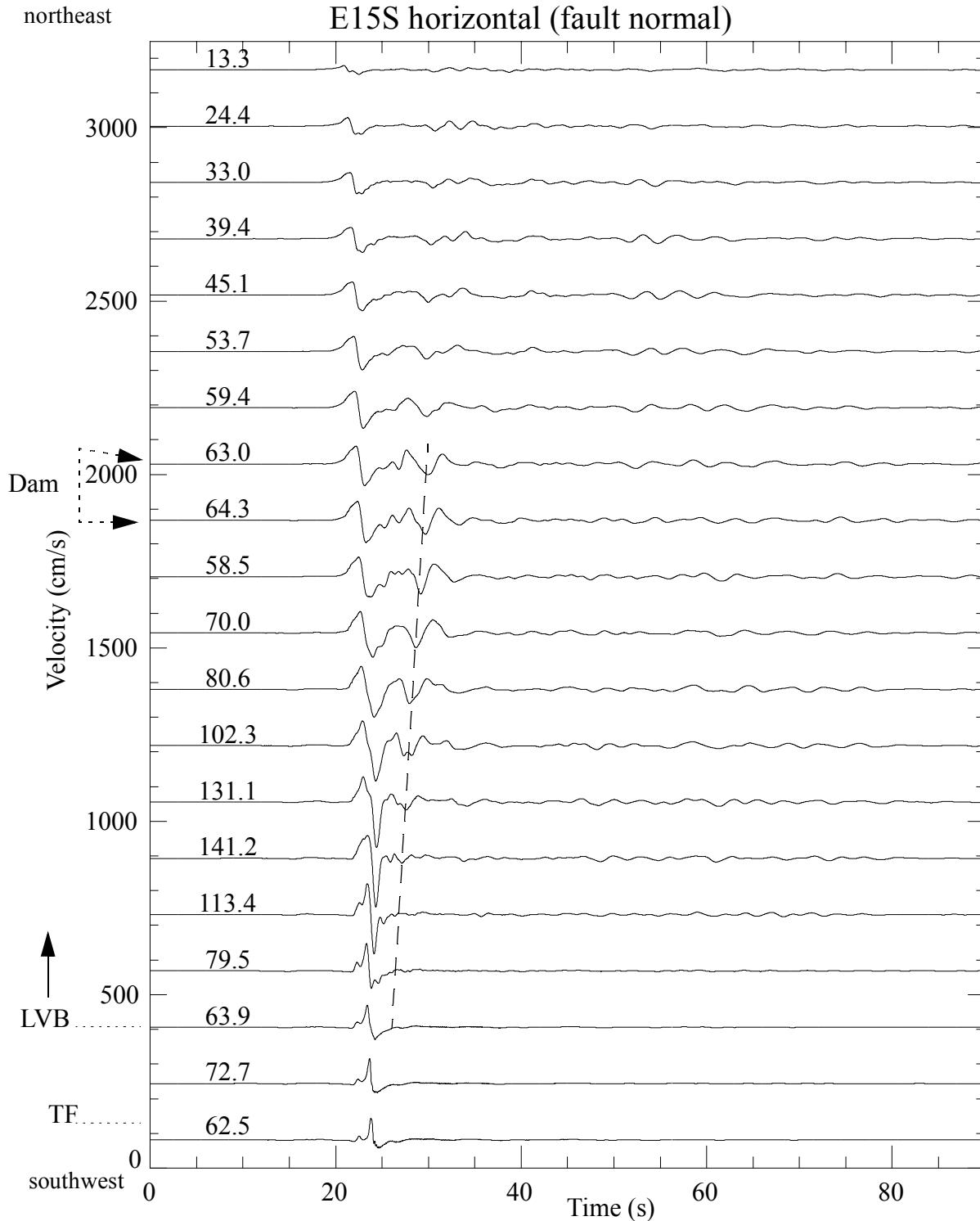


Figure 6-8: Low-frequency (< 1 Hz) E15S-component velocity waveforms for a full Teton fault rupture with a 35° fault dip. The seismograms span a 19-km profile (as shown in Figure 6-4) extending from 330 m west of the Teton fault (bottom waveform) through site JLDW with a 1 km seismogram spacing. TF is the Teton fault, western LVB-edge is dotted line labeled LVB, and dotted arrows show the two seismograms representative of the range of positions represented by the dam. Above each seismogram is its peak velocity in cm/s. Dashed line shows strong LVB-edge S-wave arrivals.

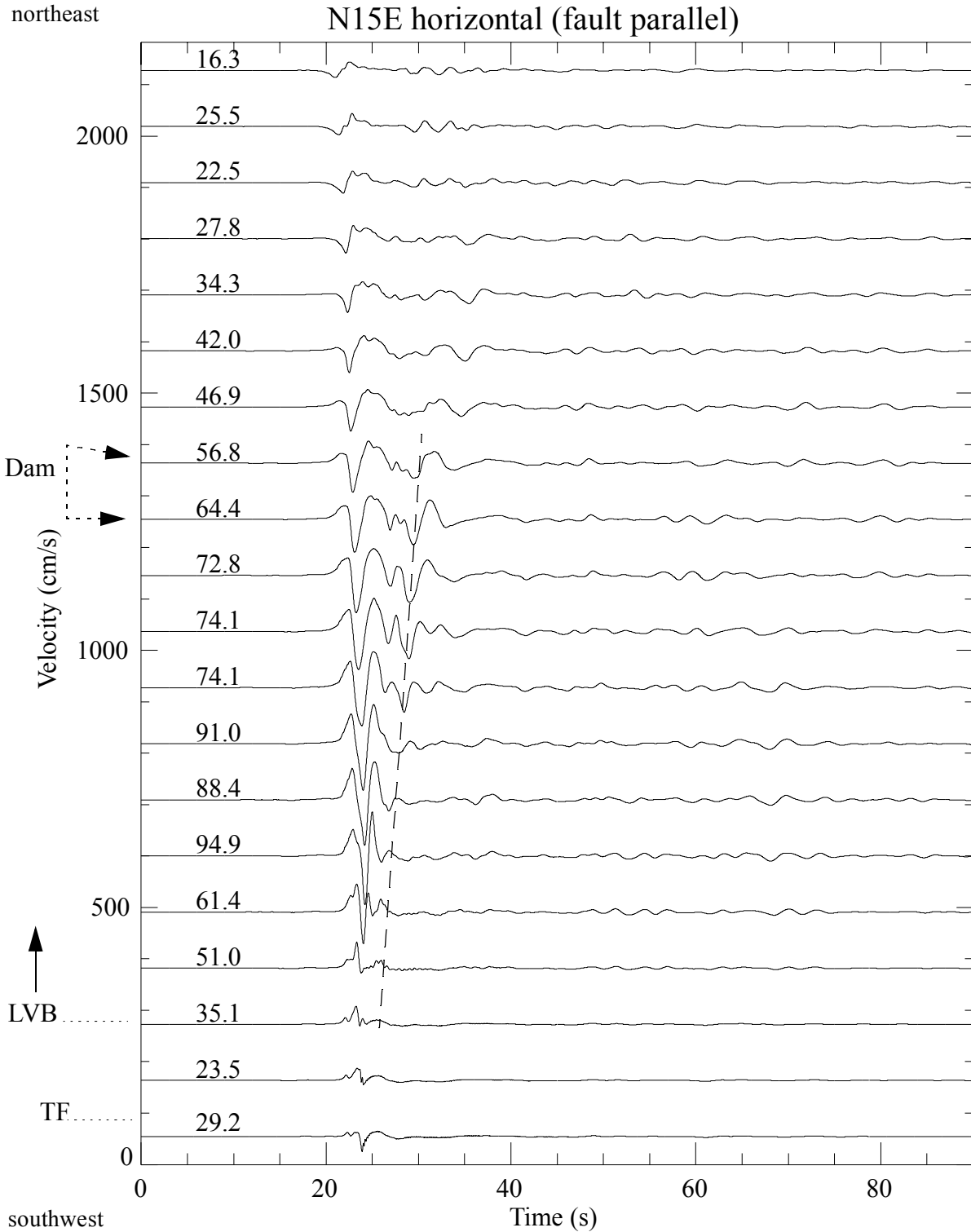


Figure 6-9: Low-frequency (< 1 Hz) N15E-component velocity waveforms for a full Teton fault rupture with a 35° fault dip. See Figure 6-8 for plot details.

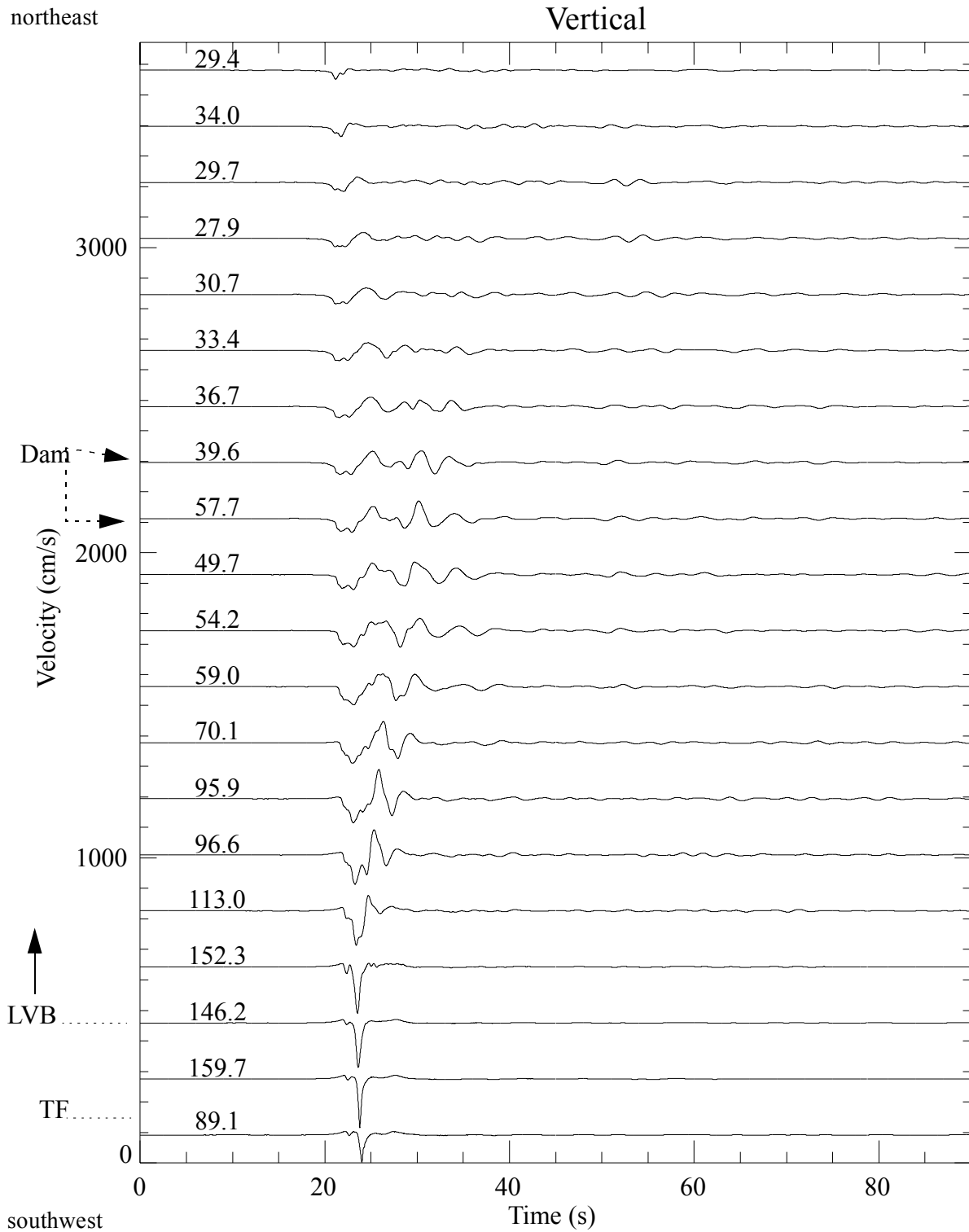


Figure 6-10: Low-frequency (< 1 Hz) vertical-component velocity waveforms for a full Teton fault rupture with a 35° fault dip. See Figure 6-8 for plot details.

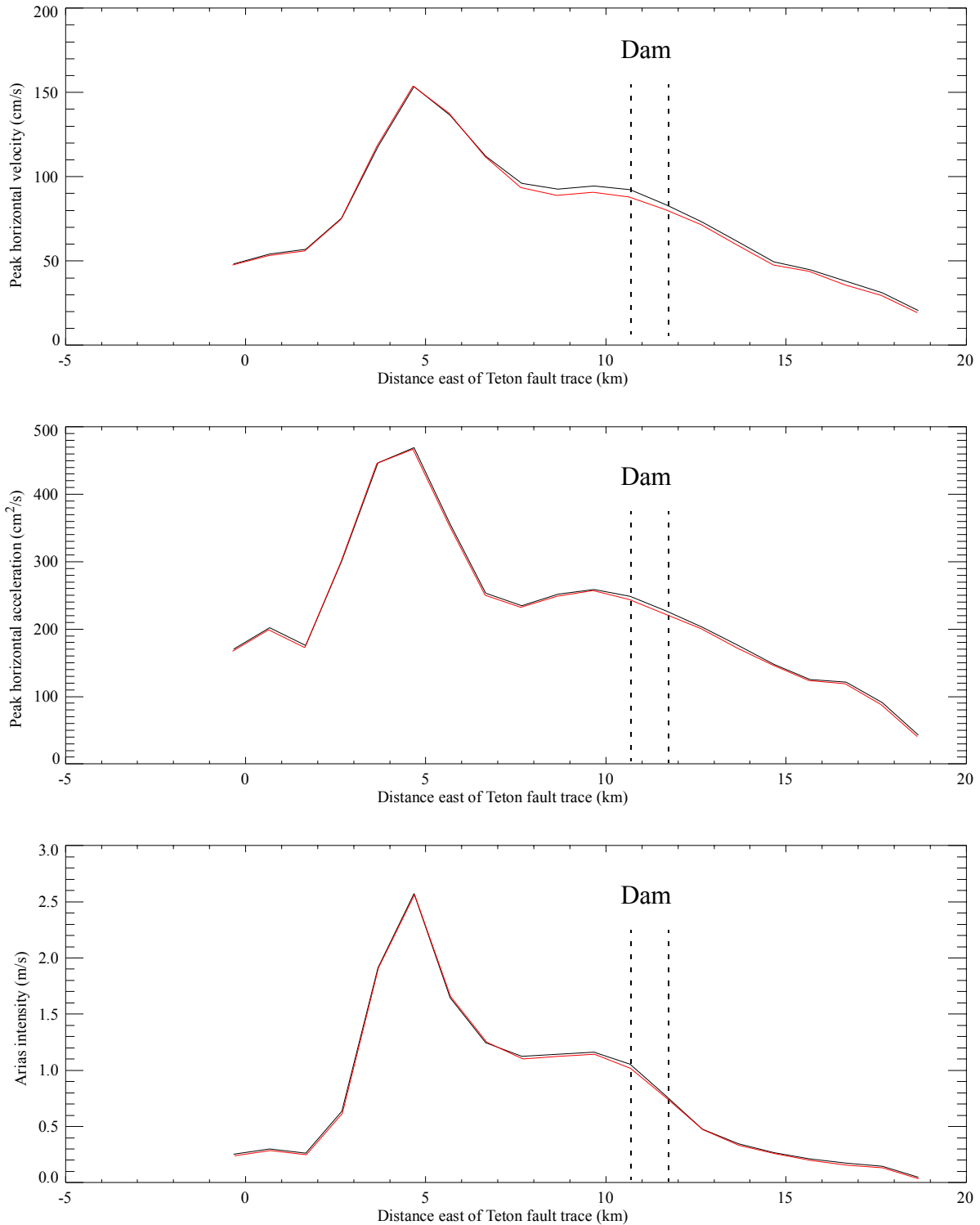


Figure 6-11: Low-frequency (< 1 Hz) horizontal peak velocity, acceleration, and Arias intensity profiles for a full Teton fault rupture with a 35° dip (black curves). The ground motion profiles span a 19-km profile extending from 330 m west of the Teton fault through site JLDW as shown in Figure 6-4. Red curves are results when only the 42-km-long northern rupture segment is used instead of the entire length of the Teton fault. Note, minimum near-surface S-wave velocities of ~1 km/s in the 3D model represent rock site conditions. These results do not account for soil responses.

they originate as S-waves at the western edge of the LVB and contribute to the increased Arias Intensities at the dam. They diminish rapidly in amplitude east of the dam (Figures 6-8 and 6-9), producing the sharp reduction in Arias Intensity east of the dam (Figure 6-11).

Figure 6-11 shows that peak ground motions and Arias Intensities at the latitude of the dam are relatively insensitive to the inclusion of seismic energy associated with rupture of the ~18-km-long southern Teton fault rupture segment. Likewise, the addition of the southern ~18-km-long rupture segment does not appreciably increase ground motion durations at the dam. For instance, PHVs > 15 cm/s occur ~40 s after the beginning of strong shaking on the E15S component associated with the first S-wave arrivals even when the seismic energy from the southern Teton fault rupture segment is not included in the simulated ground motions. The closest point of the southern Teton fault rupture segment is > 22 km from the south end of the dam and is located beyond the southern limits of the LVB. Essentially the same conclusions were reached in 3D finite-difference simulations of ground motions using two other asperity models of earthquake rupture. Rupture toward the dam (from the southern edge of the southern rupture segment) was used in all three asperity model ground motion simulations, but inclusion of the southern rupture segment in the ground motion calculations produced little change in PHA, PHA, or Arias Intensity relative to omitting the seismic energy from the southern rupture segment from the simulated ground motions. Consequently, it was concluded that the southern Teton fault rupture segment does not strongly influence peak ground motions or durations at site JLDW for fault dips of 35°.

For a Teton fault dip of 60°, the PHVs on the fault normal component (Figure 6-12) are not always larger than on the fault parallel component (Figure 6-13). In fact, the largest PHV occurs on the fault parallel component, providing clear evidence of strong 3D LVB influences on the strong ground motions. As was the case with a fault dip of 35°, the strongest vertical ground motions occur adjacent to the fault on the rock portion of the hanging wall (Figure 6-14). PHVs > 15 cm/s occur ~40 s after the first S-wave arrival (Figures 6-12 and 6-13), as also occurred for a fault of 35°; the LVB duration effects is not a strong function of fault dip. Strong velocity pulses nearly comparable in amplitude to the PHVs associated with direct S-waves occur about 8 s after the first S-wave arrival at the dam (dashed lines in Figures 6-12 and 6-13). These arrivals have

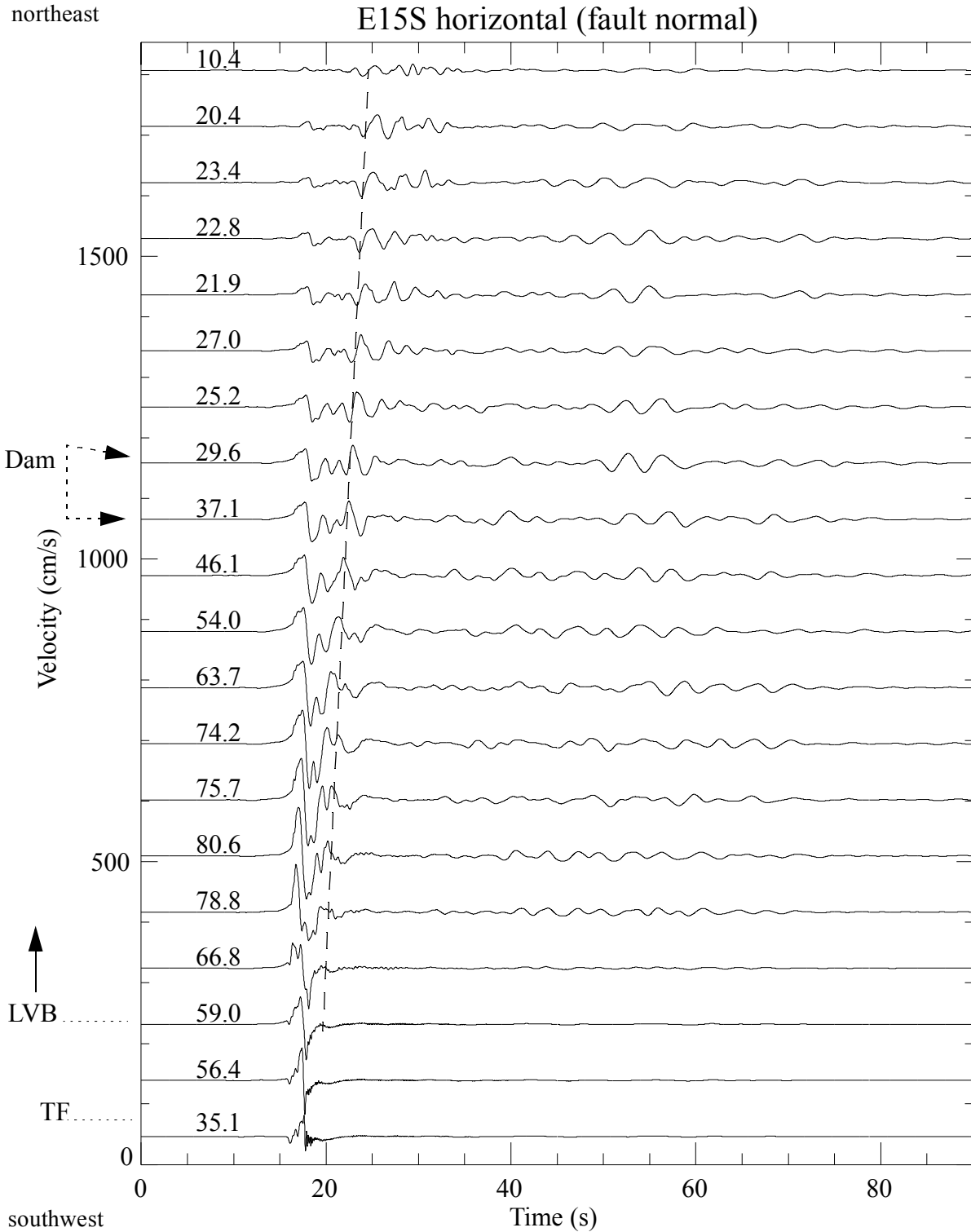


Figure 6-12: Low-frequency (< 1 Hz) E15S-component velocity waveforms for a full Teton fault rupture with a 60° fault dip. See Figure 6-8 for plot details.

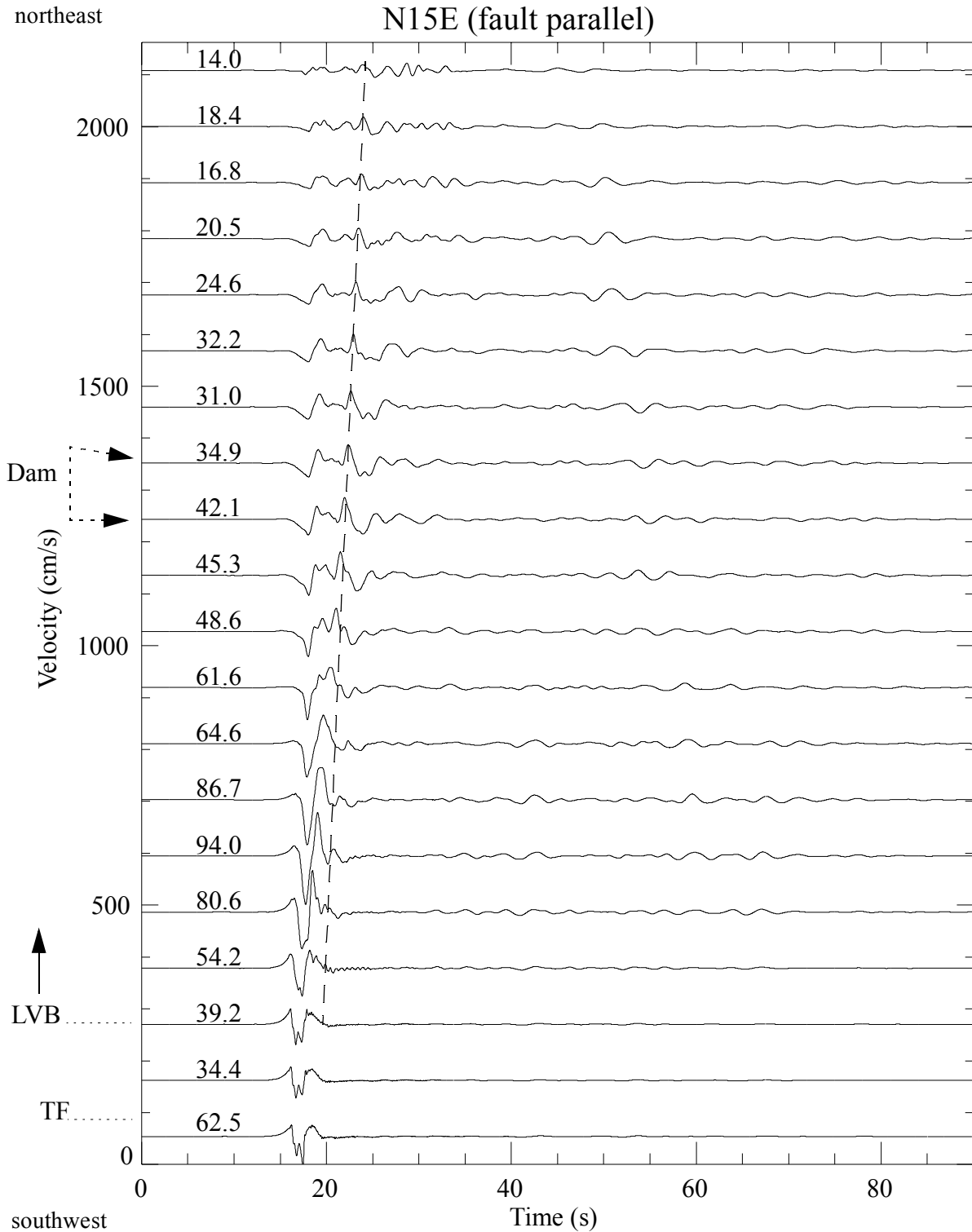


Figure 6-13: Low-frequency (< 1 Hz) N15E-component velocity waveforms for a full Teton fault rupture with a 60° fault dip. See Figure 6-8 for plot details.

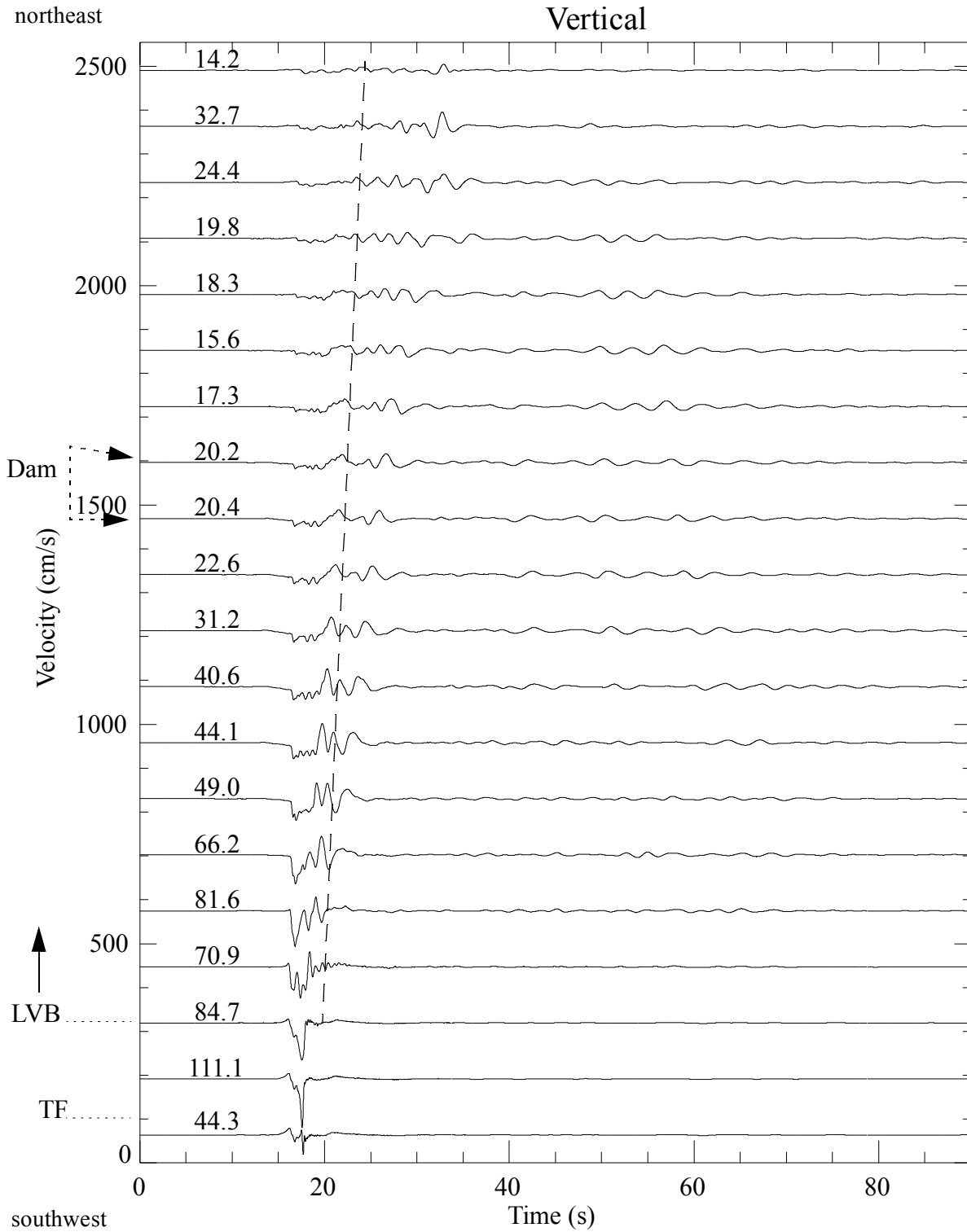


Figure 6-14: Low-frequency (< 1 Hz) vertical-component velocity waveforms for a full Teton fault rupture with a 60° fault dip. See Figure 6-8 for plot details.

apparent velocities indicating that they originate as S-waves at the western edge of the LVB and contribute to the increased Arias Intensities at the dam. They diminish slowly in amplitude west of the dam (Figures 6-12 and 6-13), producing a more gradual reduction in Arias Intensity east of the dam (Figure 6-15), compared to the case of a 35° fault dip (Figure 6-11). These results indicate that large-amplitude LVB-edge S-waves will occur at the dam, independent of fault dip. However, PHVs and PHAs are reduced for a fault dip of 60°, and PHVs and PHAs at the dam are lower than PHVs and PHAs near the fault (Figure 6-15) Arias Intensities for a fault dip of 60° are reduced by 50% relative to a fault dip of 35° (compare Figures 6-15 with 6-11). As was the case of a fault dip of 35°, for a fault dip of 60° PHVs, PHAs, and Arias Intensities at the latitude of the dam are little affected by rupture of the southern Teton fault rupture segment (Figure 6-15). Consequently, further investigations of the influence of the southern Teton fault rupture segment on ground motions at site JLDW were not pursued.

6.4.3 Broadband Hybrid Ground Motions. Only the combined broadband RGF and EGF ground motion results are reported for brevity. Based on the results of Section 6.4.2 we only simulate ground motions for rupture on the 42-km-long northern segment of the Teton fault. A total of 3300 rupture scenarios and resultant ground motions were calculated using 33 hypocenter positions and 100 rupture model fractal randomizations. Eleven strike positions at distances (in km) of 0.8, 4.8, 8.8, 12.8, 16.8, 20.8, 24.8, 28.8, 32.8, 36.8, and 40.8 from the south end of the fault were used to ensure an even span of hypocenter strike positions, since there is no prior information as to where along strike rupture is likely to start. Conversely, most normal-faulting earthquake rupture from near the base of seismicity towards the surface, so hypocenters were placed at depths of 13.8, 14.8, and 15.8 km, consistent with the findings of Doser and Smith (1989). They found that in the extensional region of the western United States that all $M \geq 7.0$ earthquakes occurred at depths of ≥ 12 km. Since each hypocenter position interacts differently with the 100 fractal randomizations of rupture and healing velocities, and effective stress, the 33 hypocenter positions produce a total of 3300 discrete rupture scenarios and independent ground motions; this number of ground motions simulations is sufficient to calculate various ground motion quantiles and to investigate the dependence of ground motions on hypocenter position.

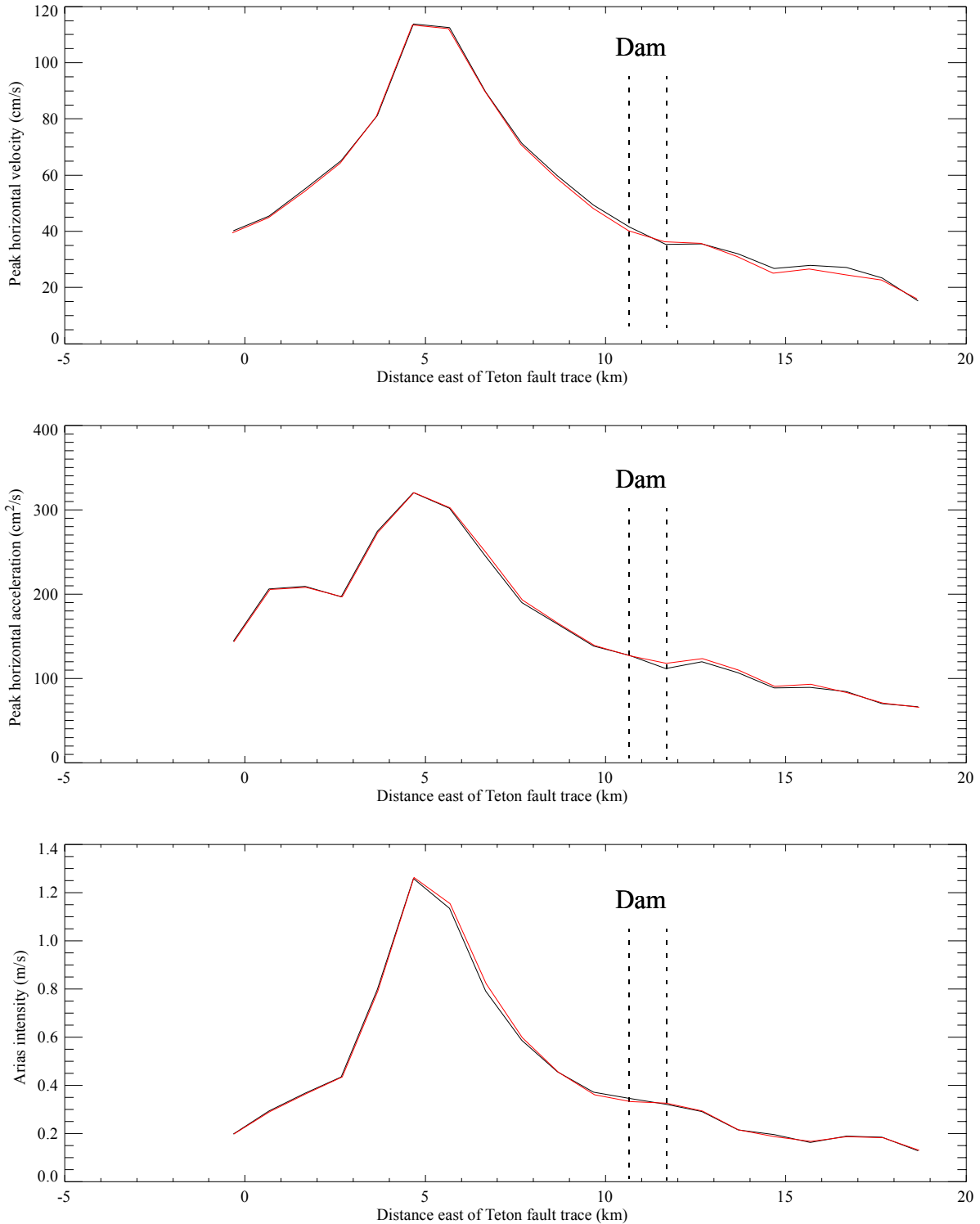


Figure 6-15: Low-frequency (< 1 Hz) horizontal peak velocity, acceleration, and Arias intensity profiles for a full Teton fault rupture with a 60° dip (black curves). The ground motion profiles span a 19-km profile extending from 330 m west of the Teton fault through site JLDW as shown in Figure 6-4. Red curves are results when only the 42-km-long northern rupture segment is used, instead of the entire length of the Teton fault. Note, minimum near-surface S-wave velocities of ~1 km/s in the 3D model represent rock site conditions. These results do not account for soil responses.

6.4.3.2 Northern Teton Fault Segment - 35° Dip. Table 6-2 summarizes the characteristics of broadband ground motions synthesized for station JLDW. Arias duration and energy duration are defined as the time between the 5% and 95% of total Arias Intensity and cumulative kinetic energy, respectively. Since the EGFs were limited to ~13.5 s durations, all duration-related quantities (Arias Intensity and duration, and energy duration) are lower bounds.

Table 6-2: JLDW Rock Ground Motion Parameters: 35°-Dipping Northern Teton Fault Segment.

Component	Peak velocity	Arias Intensity	Cumulative energy	Arias duration	Energy duration
	(cm/s)	(m/s)	(J)	(s)	(s)
E15S mean	146	6.2	10,928	15.1	21.2
E15S 84%	201	9.3	15,343	17.7	27.9
N15E mean	102	3.5	9,111	18.5	21.2
N15E 84%	135	5.1	14,154	21.4	26.3
Vertical mean	125	2.4	11,233	16.5	14.3
Vertical 84%	147	3.4	15,709	20.1	16.9

The strongest shaking occurs on the fault-normal (E15S) horizontal component, indicating a substantial influence from rupture directivity. However, ground motions on the fault-parallel (N15E) horizontal component are also substantial. Peak velocities are very large, exceeding the largest median and 84% peak velocities estimated previously for a Reclamation dam by > 50% (Casitas Dam, O'Connell, 1999b). Maximum Arias Intensities are similar to empirical attenuation relation predictions of Kayen and Mitchell (1997) for rock sites. The energy durations exceed the Arias durations by about 10 s because the LVB and relatively high site kappa of ~0.08 produce stronger long duration velocity responses than high-frequency acceleration responses.

The mean (Figure 6-16) and 84% (Figure 6-17) E15S acceleration response spectra (PSA) exhibit responses more similar to soil responses from the Spudich et al. (1999) extensional acceleration attenuation relations than rock responses. At periods > ~1.2 s the 35° PSA response become much larger than predicted by Spudich et al. (1999), reflecting the strong influence of the LVB at rock site JLDW, and the unusually large peak velocities in Table 6-2. Conversely, E15S acceleration

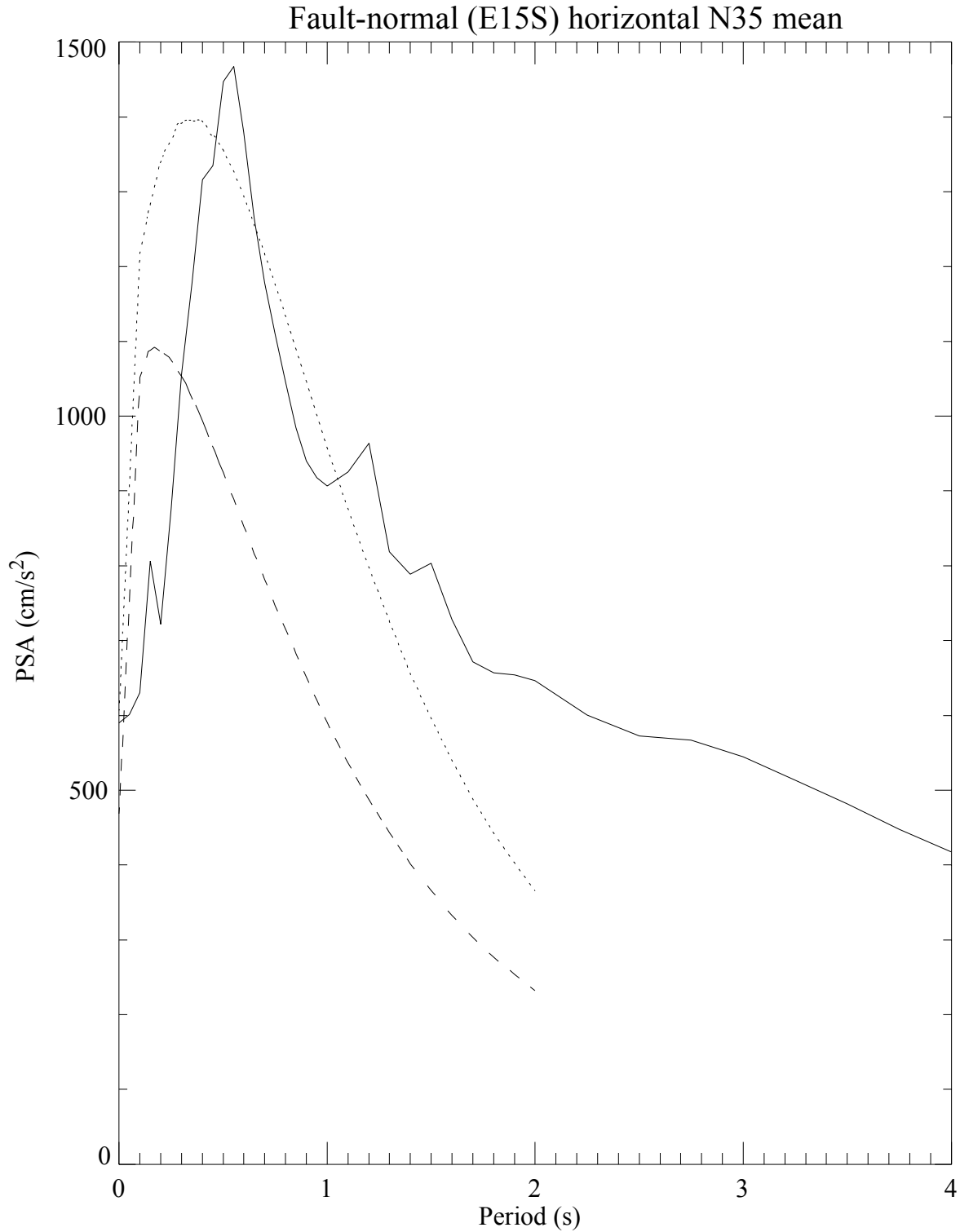


Figure 6-16: JLDW rock site mean downstream horizontal PSA response spectra for a 35°-dipping northern Teton fault segment (solid). SEA99 average horizontal component estimates for a M 7.0 normal-faulting earthquake are shown for soil (dotted) and rock (dashed) site conditions.

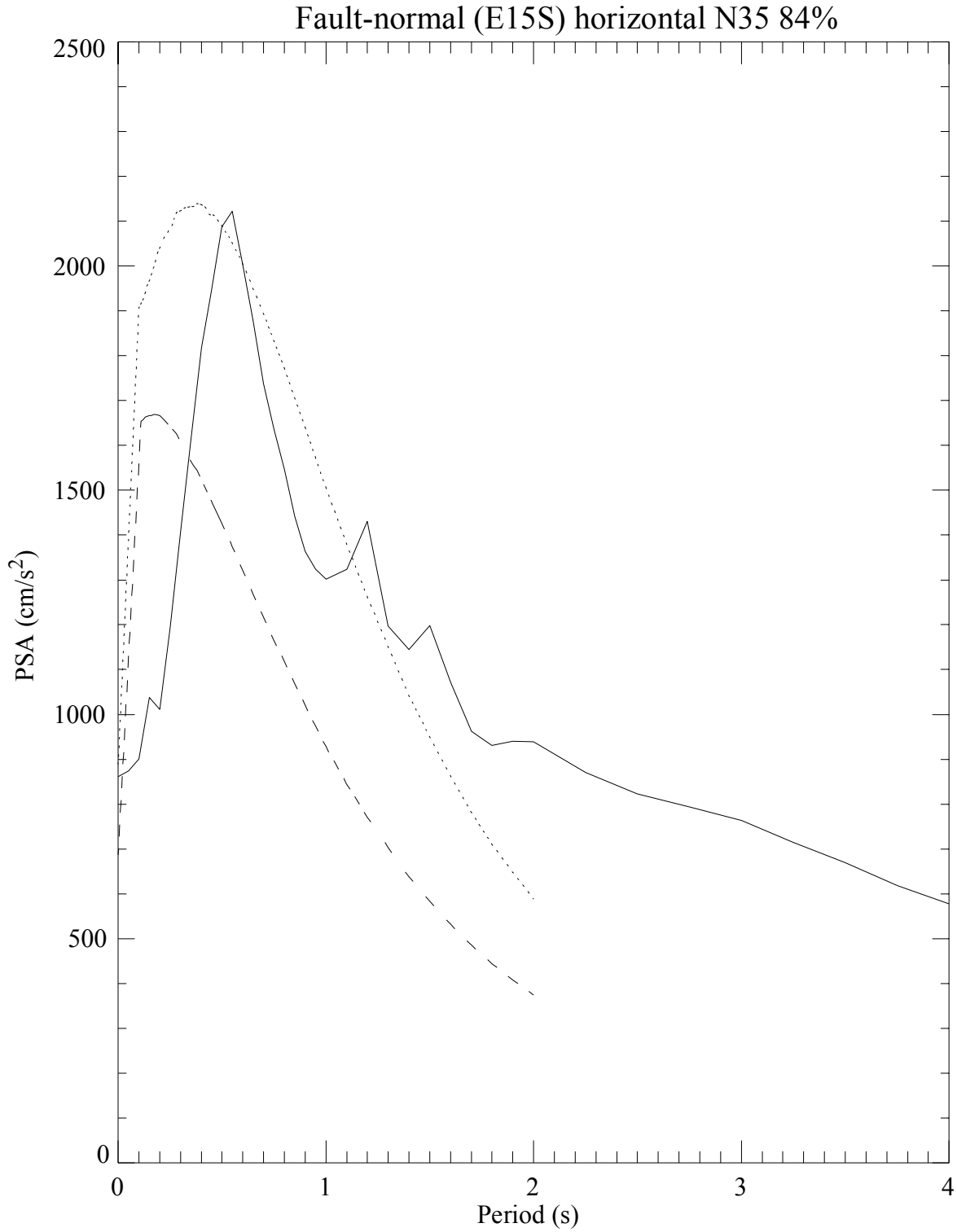


Figure 6-17: JLDW rock site 84% quantile downstream horizontal PSA response spectra for a 35°-dipping northern Teton fault segment (solid). SEA99 average horizontal component estimates for a M 7.0 normal-faulting earthquake are shown for soil (dotted) and rock (dashed) site conditions.

responses decrease more rapidly for periods < 0.5 s than Spudich et al. (1999), reflecting the relatively large kappa of ~ 0.08 at site JLDW, relative to rock kappa values of ~ 0.04 more typically associated with rock sites. However, peak accelerations in Figures 6-16 and 6-17 are very similar to the Spudich et al. (1999) estimates for a **M** 7.0 normal-faulting earthquake.

The fault-parallel (N15E) PSAs are about 60% of the fault-normal (E15S) PSAs for periods < 1 s indicating a significant influence from directivity (Figure 6-18), as expected for a dip slip fault (O'Connell and Ake, 2003), but the horizontal PSAs become nearly equal at periods > 3 s; the long-period responses are dominated by the influences of the 3D LVB and nearly independent of horizontal component orientation. The vertical PSA have a secondary maximum between 2 s and 3 s associated with some aspect of the 3D LVB response.

PSA responses are sensitive to hypocenter position. Hypocenters near the center of the fault along strike produce typical vertical and fault-normal (E15S) responses, but produce substantially lower fault-parallel (N15E) responses (Figure 6-18), with 84% fault-parallel PSAs being barely larger than mean PSAs for all hypocenter positions. Conversely, fault-parallel and fault-normal PSAs are significantly larger for northern hypocenters (Figure 6-19). For fault-normal PSAs, PSAs increase primarily for periods < 1 s, indicating that the interaction between northern 3D LVB structure and north hypocenter rupture times increases rupture directivity. For fault-parallel PSAs, PSAs increase nearly uniformly for nearly all periods, indicating a strong contribution of some aspect of the 3D LVB structure to fault-parallel ground motions. Southern hypocenters (Figures 6-20) produce substantially lower fault-normal responses and only slightly larger fault-parallel PSA responses. The combination of a steep LVB boundary dip, a deeper basin at the north end of the 3D LVB, and hypocenters near the northern LVB boundary, produce the strongest ground motions at the dam and indicate that this type of velocity structure would likely produce peak acceleration responses at the dam about 50% larger than indicated in Figures 6-16 and 6-17. Thus, the assumptions about details of LVB margin structure strongly influence estimated ground motions at the dam. As indicated in Section 4, there are significant uncertainties about structure of the northern, eastern, and southwestern margins of the LVB. If the southwestern margin of the LVB has a steeper dip and a thicker section of low-velocity sediments, peak ground motion responses at the dam may be under predicted. Conversely, if the northeastern margins of the LVB have

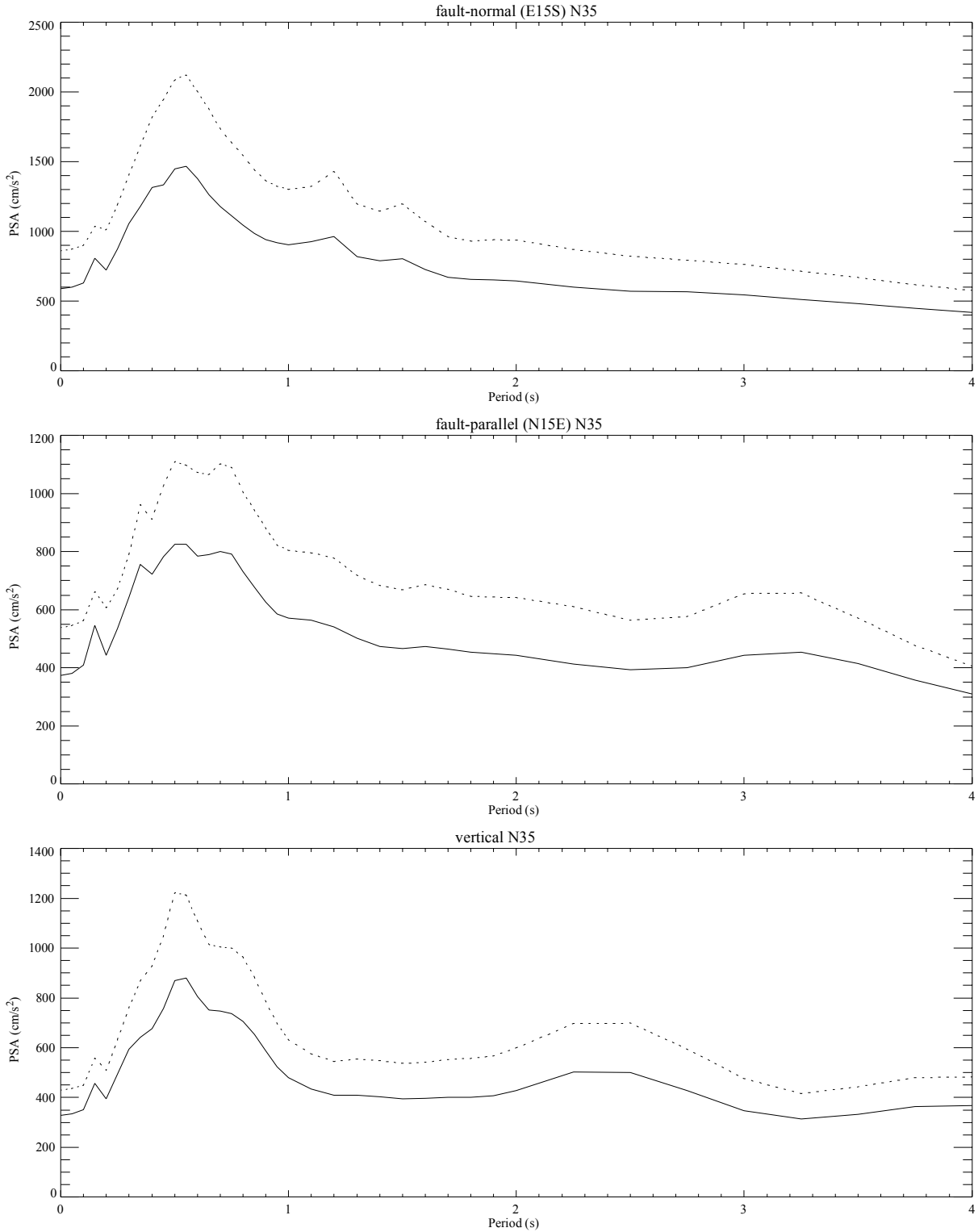


Figure 6-18: JLDW rock site PSA response spectra for a 35°-dipping northern Teton fault segment for all hypocenters. Mean curves are solid and 84% quantile curves are dotted. Components are as labeled.

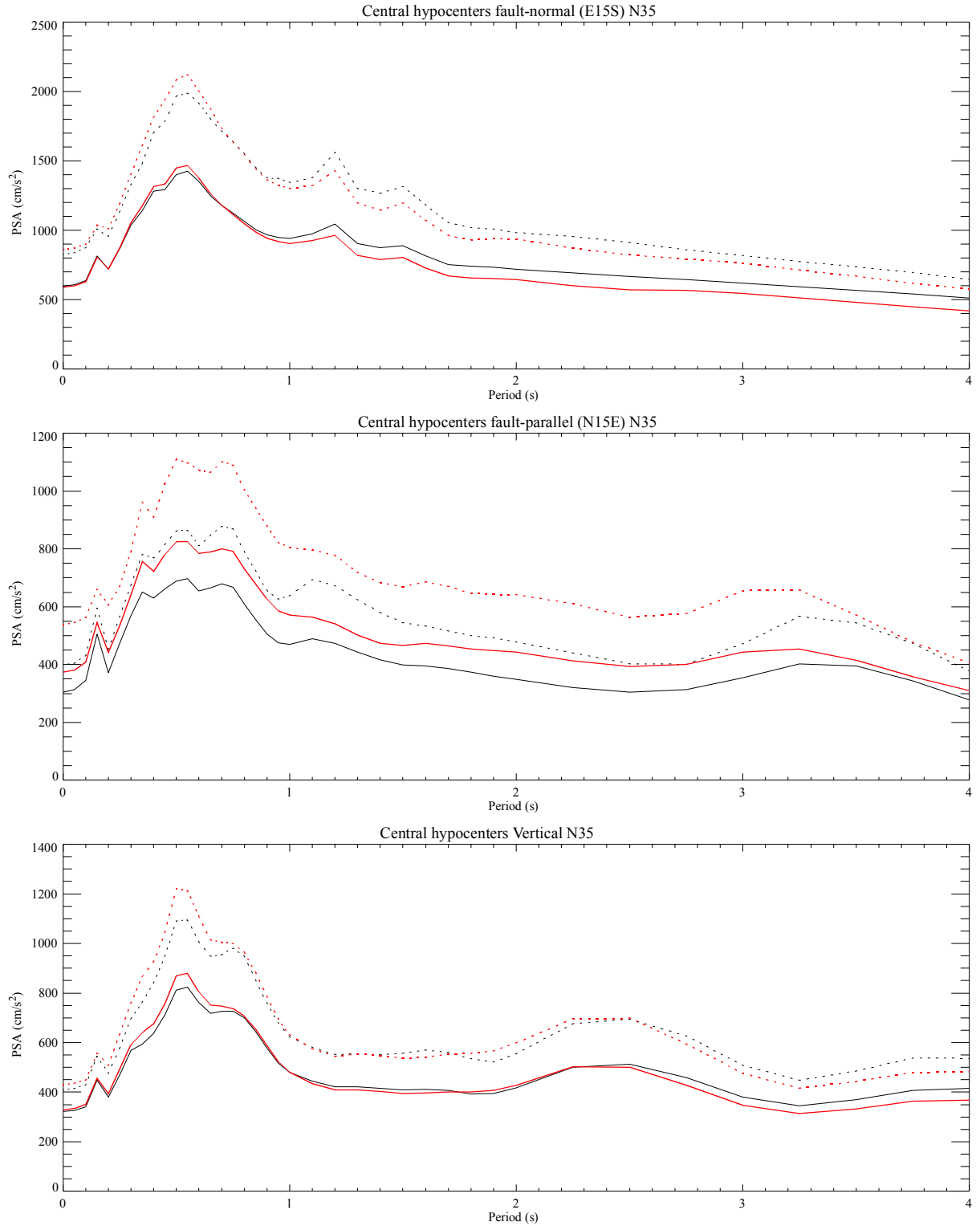


Figure 6-19: JLDW rock site central hypocenter PSA response spectra for a 35°-dipping northern Teton fault segment (black). Red curves are reference mean (solid) and 84% quantile (dotted) results using all hypocenters (from Figure 6-18). Components are as labeled.

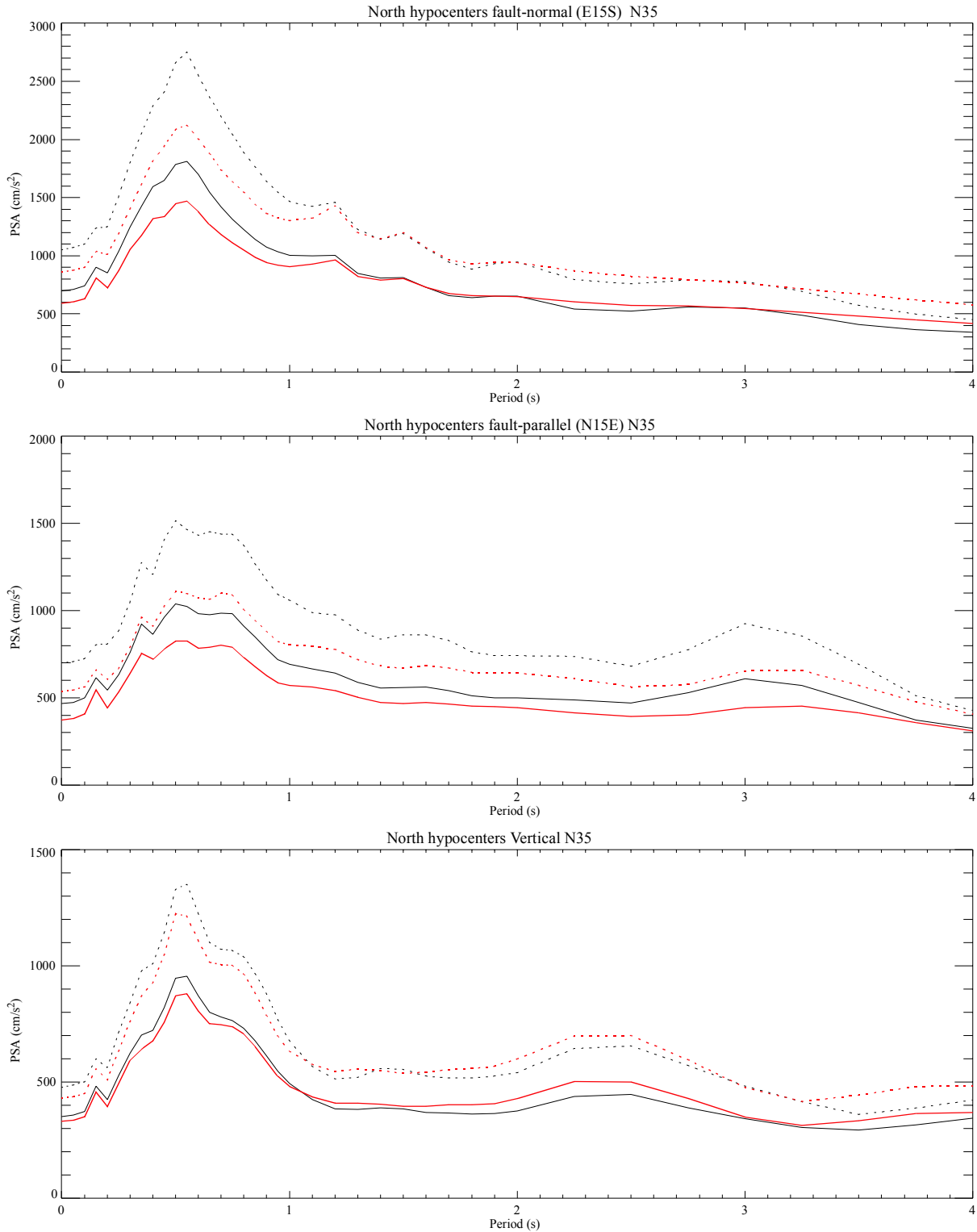


Figure 6-20: JLDW rock site northern hypocenter PSA response spectra for a 35°-dipping northern Teton fault segment (black). Red curves are reference mean (solid) and 84% quantile (dotted) results using all hypocenters (from Figure 6-18). Components are as labeled.

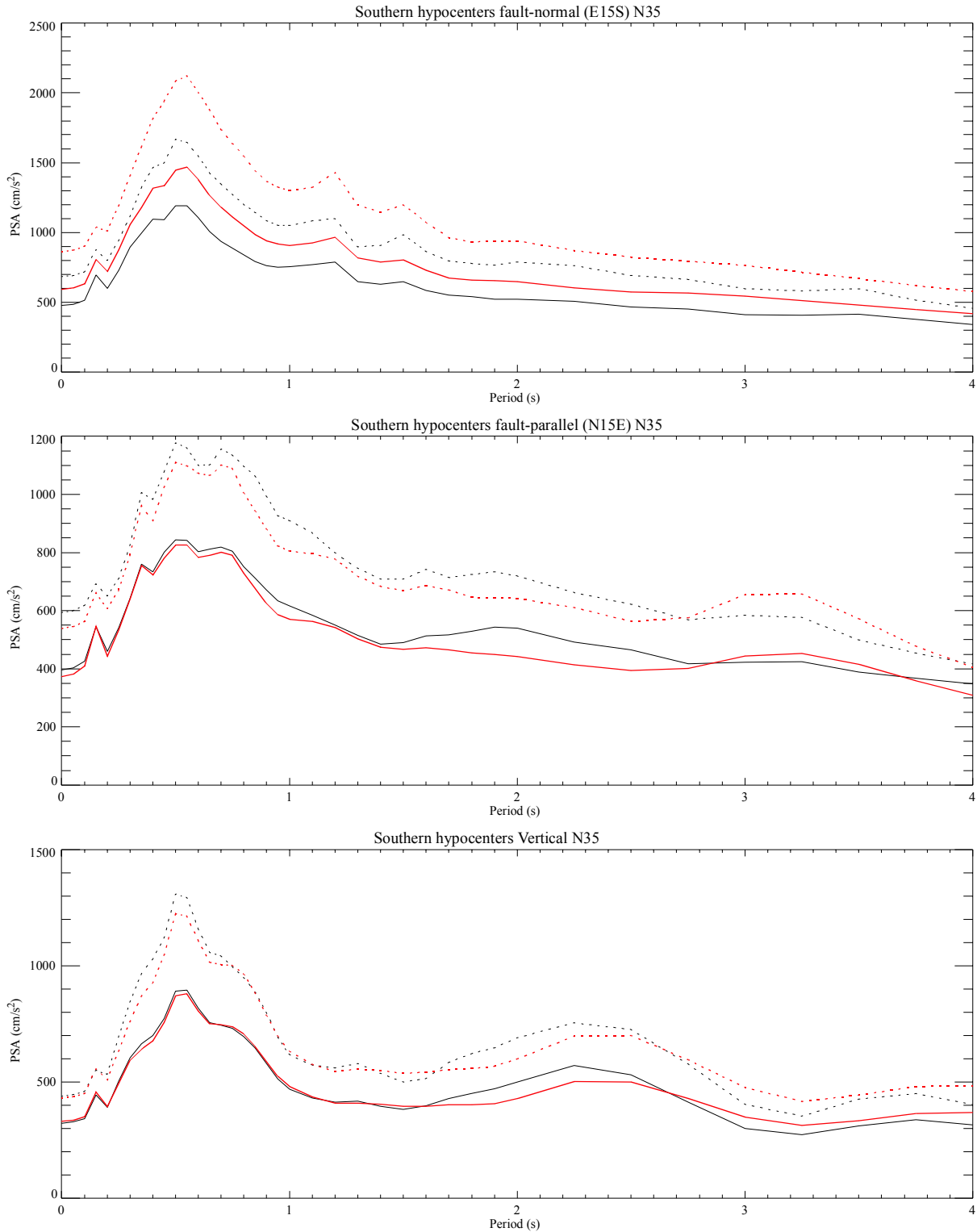


Figure 6-21: JLDW rock site southern hypocenter PSA response spectra for a 35°-dipping northern Teton fault segment (black). Red curves are reference mean (solid) and 84% quantile (dotted) results using all hypocenters (from Figure 6-18). Components are as labeled.

shallower dips and a smaller thickness of low-velocity sediments, peak ground responses at the dam may be overpredicted. These issues are evaluated in detail in Section 7 using earthquakes recorded at the dam from a variety of azimuths and distances.

6.4.3.3 Northern Teton Fault Segment - 45° Dip. While fault-normal peak velocities and Arias Intensities decrease relative to the 35°-fault-dip results, fault-parallel Arias Intensities are larger than the 35°-fault-dip results (compare Table 6-3 to 6-2). Vertical peak velocities decrease, but Arias Intensities are the same, compared to the 35°-fault-dip results.

Table 6-3: JLDW Rock Ground Motion Parameters: 45°-Dipping Northern Teton Fault Segment.

Component	Peak velocity	Arias Intensity	Cumulative energy	Arias duration	Energy duration
	(cm/s)	(m/s)	(J)	(s)	(s)
E15S mean	133	4.8	11,767	16.1	23.4
E15S 84%	171	7.1	16,956	18.1	33.1
N15E mean	111	4.0	10,063	18.5	21.8
N15E 84%	155	6.1	16,010	21.1	27.4
Vertical mean	105	2.4	9,605	16.3	16.7
Vertical 84%	130	3.6	14,111	19.1	20.1

Fault-normal PSA responses are about 50% larger than fault-parallel PSA responses (Figure 6-22), indicating that rupture directivity still dominates the short-period responses at the dam. Mean (Figure 6-23) and 84% (Figure 6-24) fault-normal PSA are lower than Spudich et al. (1999) soil responses, but greater than corresponding rock responses for periods < 1.5 s. For periods > 2 s, simulated PSA substantially exceed Spudich et al. (1999) soil responses, consistent with the strong influence of the 3D LVB on long-period responses; these are large acceleration loads for long-periods.

As was the case for a fault dip of 35°, N15E PSA responses for central hypocenters (Figure 6-25) are substantially lower than for southern hypocenters (Figure 6-26) or northern hypocenters (Figure 6-27). The phasing of fault rupture times, direct S-wave travel times, and LVB-edge S-

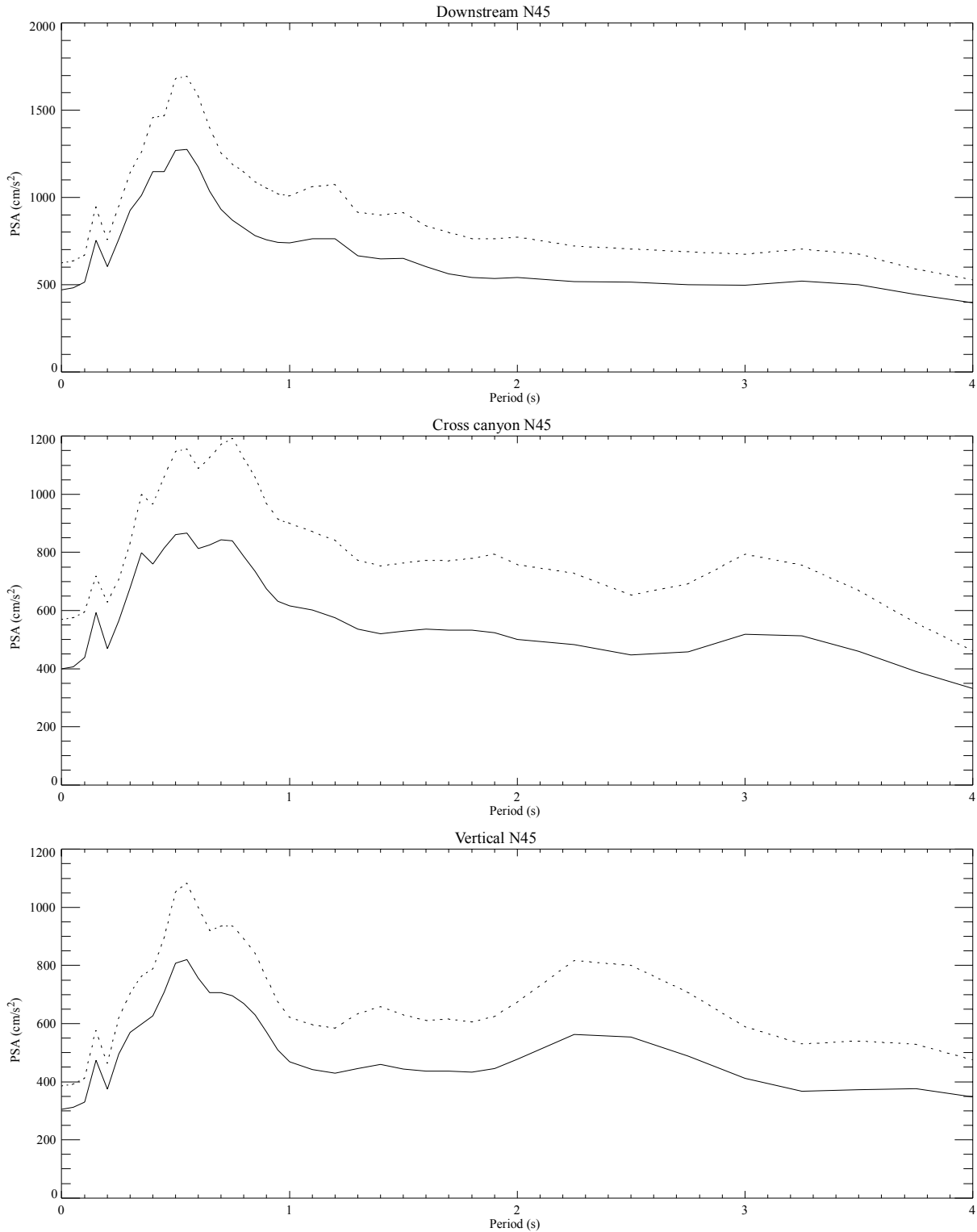


Figure 6-22: JLDW rock site PSA response spectra for a 45°-dipping northern Teton fault segment using all hypocenter positions. Mean curves are solid and 84% quantile curves are dotted. Components are as labeled.

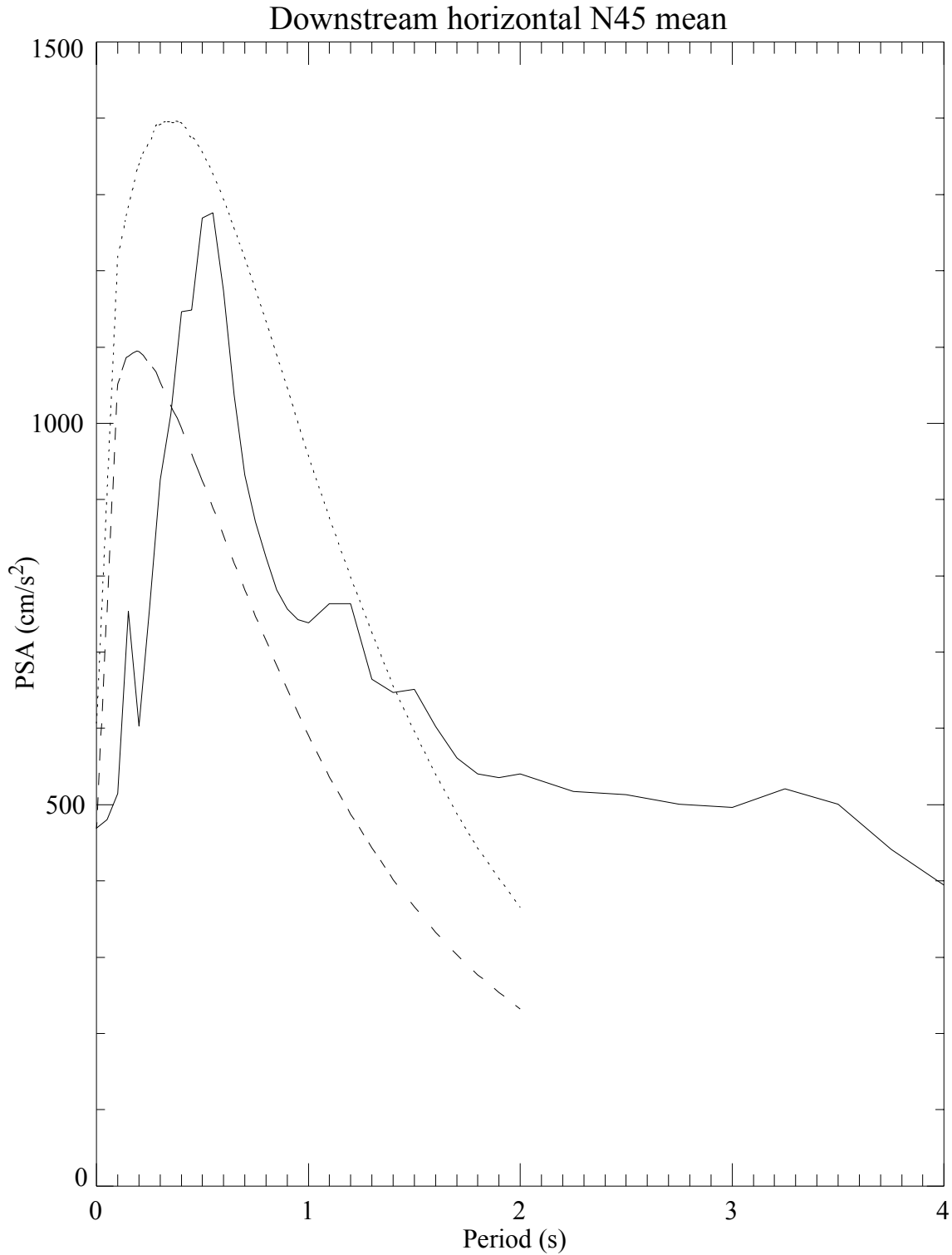


Figure 6-23: JLDW rock site mean downstream horizontal PSA response spectra for a 45°-dipping northern Teton fault segment (solid). SEA99 average horizontal component estimates for a M 7.0 normal-faulting earthquake are shown for soil (dotted) and rock (dashed) site conditions.

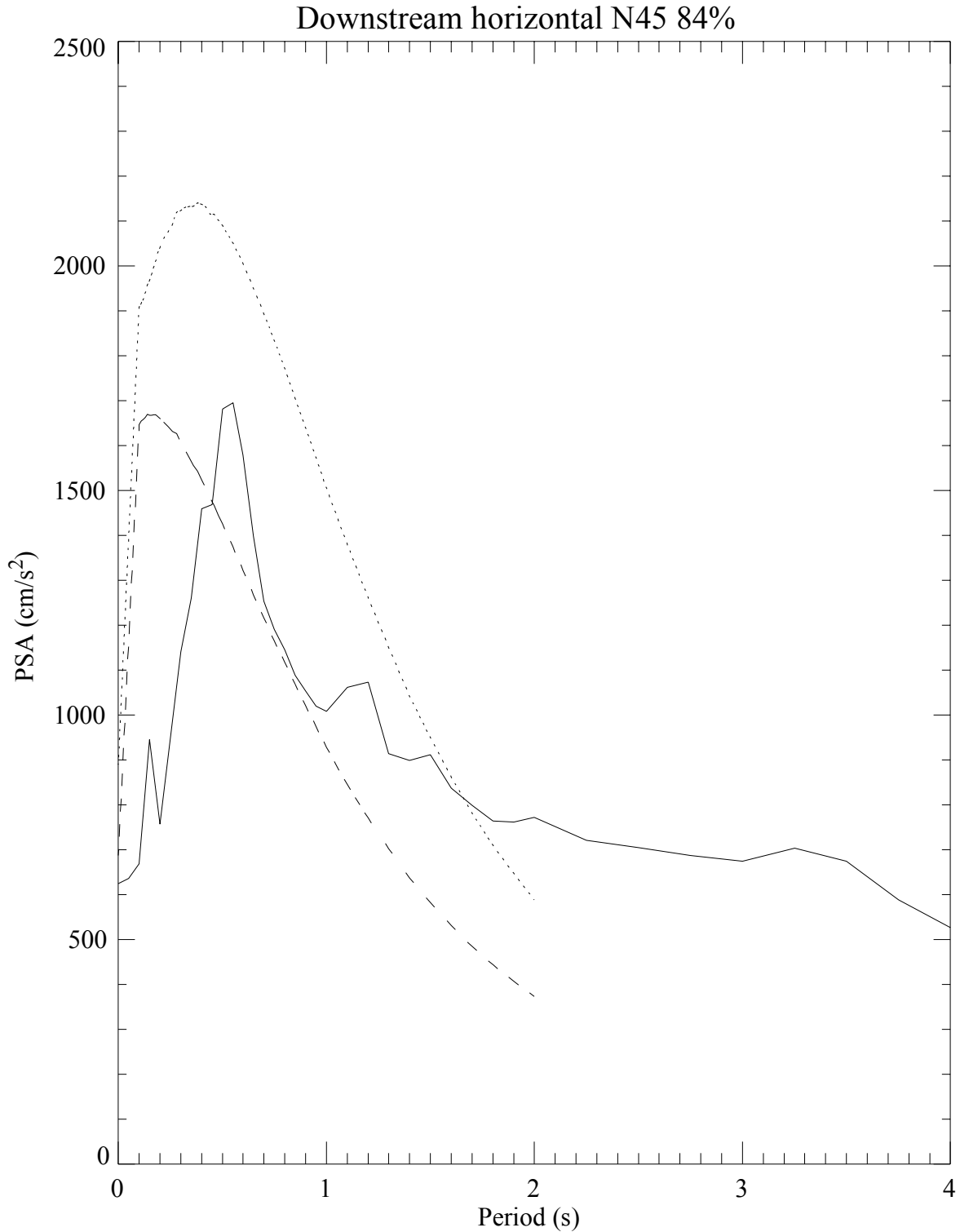


Figure 6-24: JLDW rock site 84% quantile downstream horizontal PSA response spectra for a 45°-dipping northern Teton fault segment (solid). SEA99 average horizontal component estimates for a M 7.0 normal-faulting earthquake are shown for soil (dotted) and rock (dashed) site conditions.

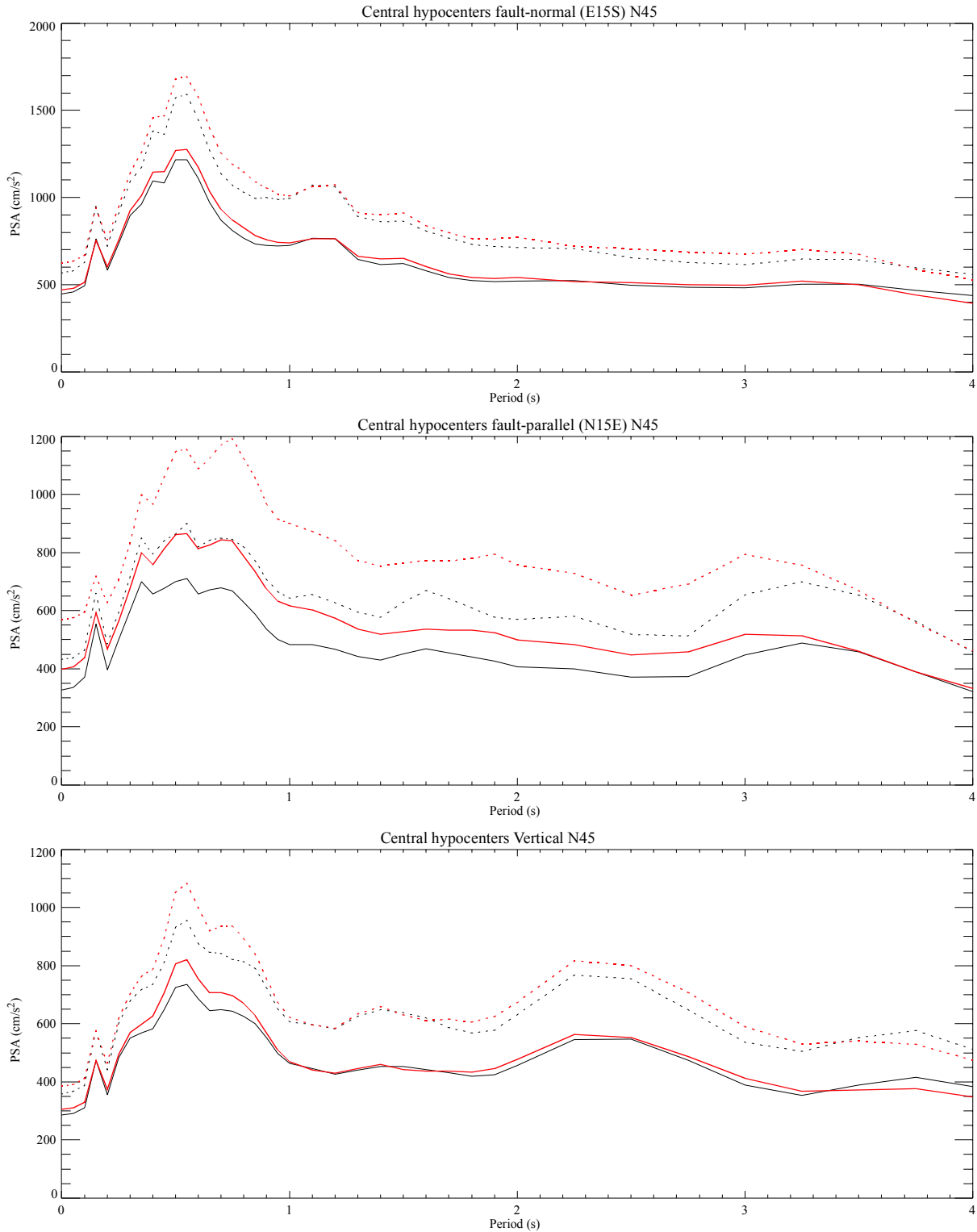


Figure 6-25: JLDW rock site central hypocenter PSA response spectra for a 45°-dipping northern Teton fault segment (black). Red curves are reference mean (solid) and 84% quantile (dotted) results using all hypocenters (from Figure 6-22). Components are as labeled.

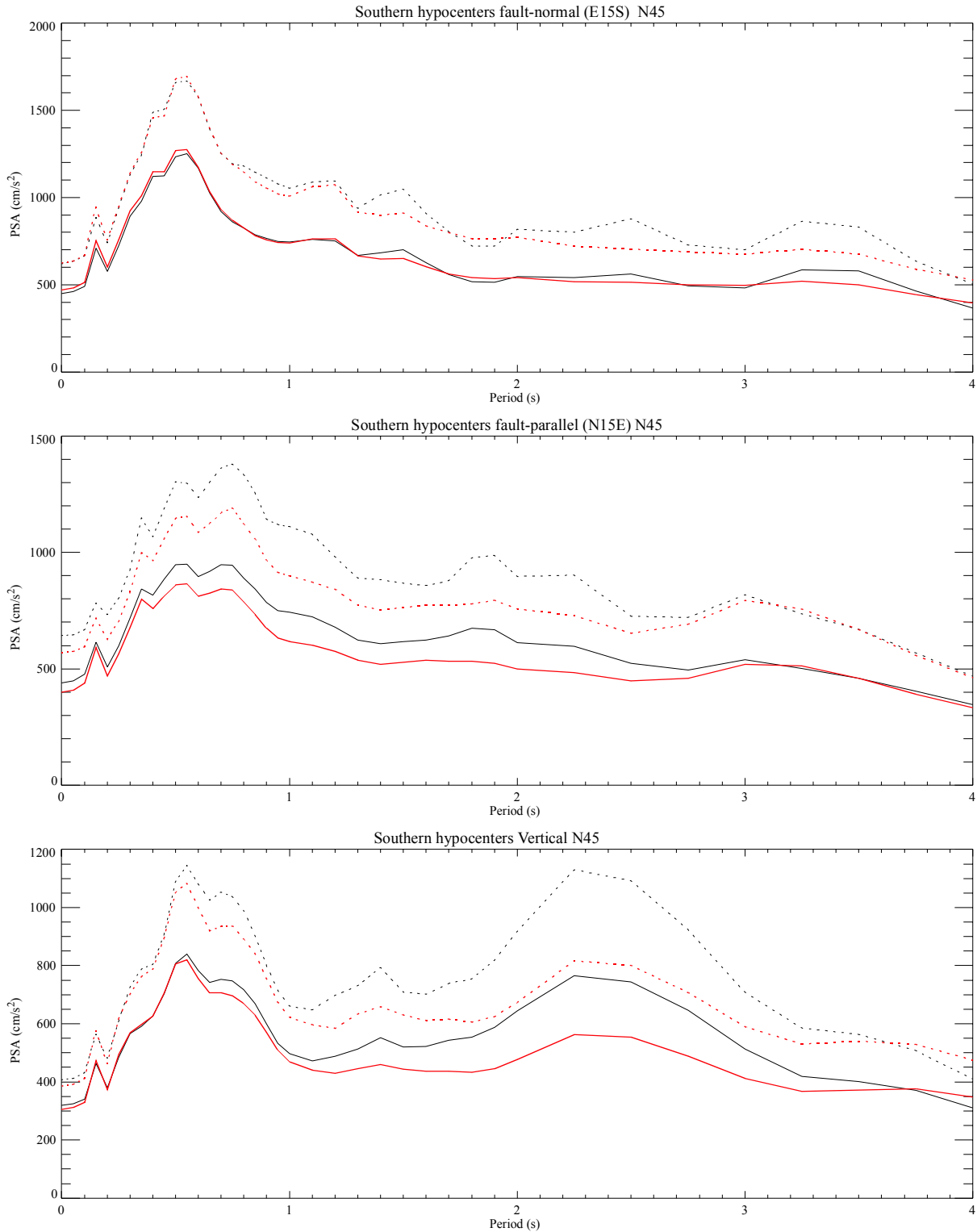


Figure 6-26: JLDW rock site southern hypocenter PSA response spectra for a 45°-dipping northern Teton fault segment (black). Red curves are reference mean (solid) and 84% quantile (dotted) results using all hypocenters (from Figure 6-22). Components are as labeled.

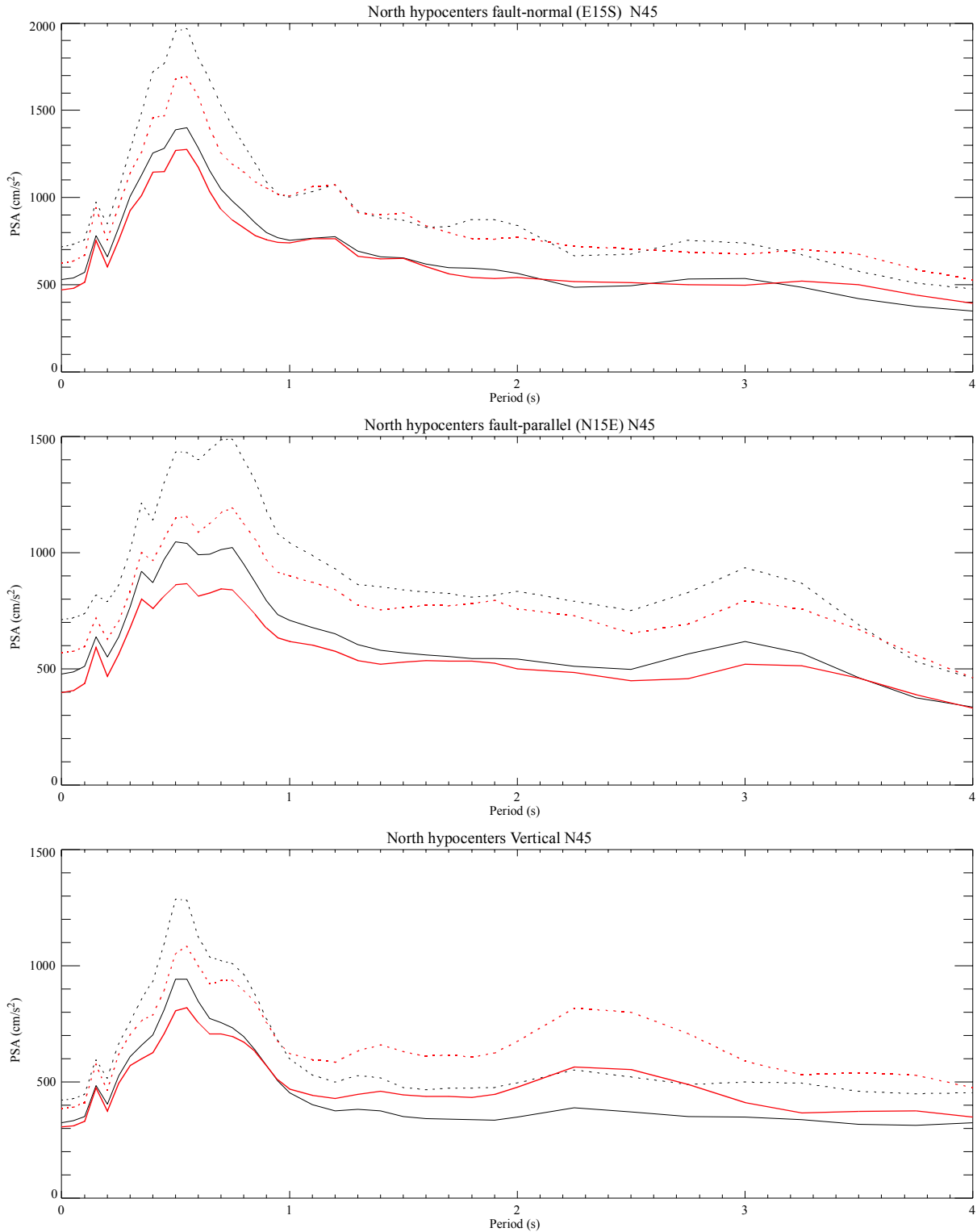


Figure 6-27: JLDW rock site northern hypocenter PSA response spectra for a 45°-dipping northern Teton fault segment (black). Red curves are reference mean (solid) and 84% quantile (dotted) results using all hypocenters (from Figure 6-22). Components are as labeled.

wave and surface wave travel times provide a qualitative explanation of these results. When hypocenters are located near the ends of the LVB, a coherent wavetrain of LVB-edge waves is preferentially generated at the hypocenter end of the LVB early in the rupture process that proceed to propagate coherently across the LVB and constructively add to direct S-wave energy produced later in the rupture process. For central hypocenters, LVB edge waves are generated much later in the rupture process and have less opportunity to add to direct S-wave energy associated with rupture of the fault, since most direct S-waves will have arrived at the JLDW prior to the arrival of the LVB edge-waves. The differences in the onset times of rupture for different hypocenter positions also explains the amplified short-period fault-normal PSA responses for northern hypocenters (Figure 6-27). Since the northern edge of the LVB is located closer to the dam than the southern end of the LVB (Figure 6-4), the LVB-edge S-waves generated at the north end of the LVB for early portions of the fault rupture can add energy to direct S-waves from later rupture beneath the dam, increasing the influence of directivity on the short period fault-normal, fault-parallel, and vertical PSA (Figure 6-27). Since the EGFs were used to construct the > 1 Hz responses and contain a wide variety of LVB-edge S-wave amplitudes and time moveouts relative to the direct S-wave arrival, the < 1 s PSA responses may be significantly underestimated because LVB-edge S-waves would likely have more systematic move-outs, amplitudes, and phasing that represented by the random summing of eight EGF responses.

The southern hypocenters produce very large (> 1 g at 84%) 2-2.5 s period vertical PSA responses, relative to other hypocenter positions (Figure 6-26). The southern end of the LVB is about twice as far from the dam as the northern end of the LVB (Figure 6-4). As noted in Section 4, LVB-edge Rayleigh waves develop only large amplitudes at the dam for the microearthquake source near the southeast edge of the LVB. It is likely that the very large 2-2.5 s period vertical PSA responses for southern hypocenter are a product of LVB-edge Rayleigh wave response generated at the southern end of the LVB. These vertical responses have PSA comparable to peak short period (< 1 s) vertical responses. Amplification of 2-2.5 s period vertical PSA responses is more subtle for a fault dip of 35° (Figure 6-21), indicating a very strong dependence of vertical LVB response to Teton fault dip, when rupture of the northern Teton fault segment initiates in the southern portion of the fault segment.

6.4.3.4 Northern Teton Fault Segment - 60° Dip. Peak ground motions are smaller for a Teton fault dip of 60° than for fault dips of 35° or 45° (Table 6-4). Peak velocities and Arias

Table 6-4: JLDW Rock Ground Motion Parameters: 60°-Dipping Northern Teton Fault Segment.

Component	Peak velocity	Arias Intensity	Cumulative energy	Arias duration	Energy duration
	(cm/s)	(m/s)	(J)	(s)	(s)
E15S mean	96	2.7	9,366	18.3	24.8
E15S 84%	122	3.9	14,100	23.0	33.8
N15E mean	84	2.6	5,616	19.5	26.0
N15E 84%	116	3.9	8,510	22.4	36.0
Vertical mean	76	1.8	4,819	15.9	20.0
Vertical 84%	98	2.6	,7220	18.7	28.2

Intensities are nearly identical on the two horizontal components of ground motion. Only cumulative kinetic energy is substantially larger on the fault-normal (E15S) component relative to the fault-parallel (N15E) component, indicating a smaller influence of rupture directivity and a proportionally larger influence of the 3D LVB on ground motion responses. Fault-normal (E15S) PSA responses are peaked at ~0.5 s (Figure 6-28), indicating that directivity does mildly amplify short period responses. Fault-parallel (N15E) PSA responses increase slightly at short periods (< 1 s), but have remarkably constant PSA responses between 1 s and 3 s period, indicating significant amplification of > 1 s responses by the 3D LVB. As seen with the 35° and 45° Teton fault dip cases, fault-parallel responses for central hypocenters (Figure 6-29) are substantially less than PSA responses for hypocenters near the ends of the fault segment, particularly hypocenters near the southern end of the fault (Figure 6-30). In the case of a fault dip of 45° both southern and northern hypocenters produced amplified fault-parallel PSA responses (Figures 6-26 and 6-27). In contrast to the case of a 60° fault dip, for a fault dip of 35° hypocenters at the northern end of the fault produced the largest fault-parallel responses (Figure 6-20). Thus, there is a very strong dependence of fault-normal motions on fault dip and hypocenter position. For a fault dip of 60°, hypocenters at the northern end of the rupture segment produce PSA closest to the simulated

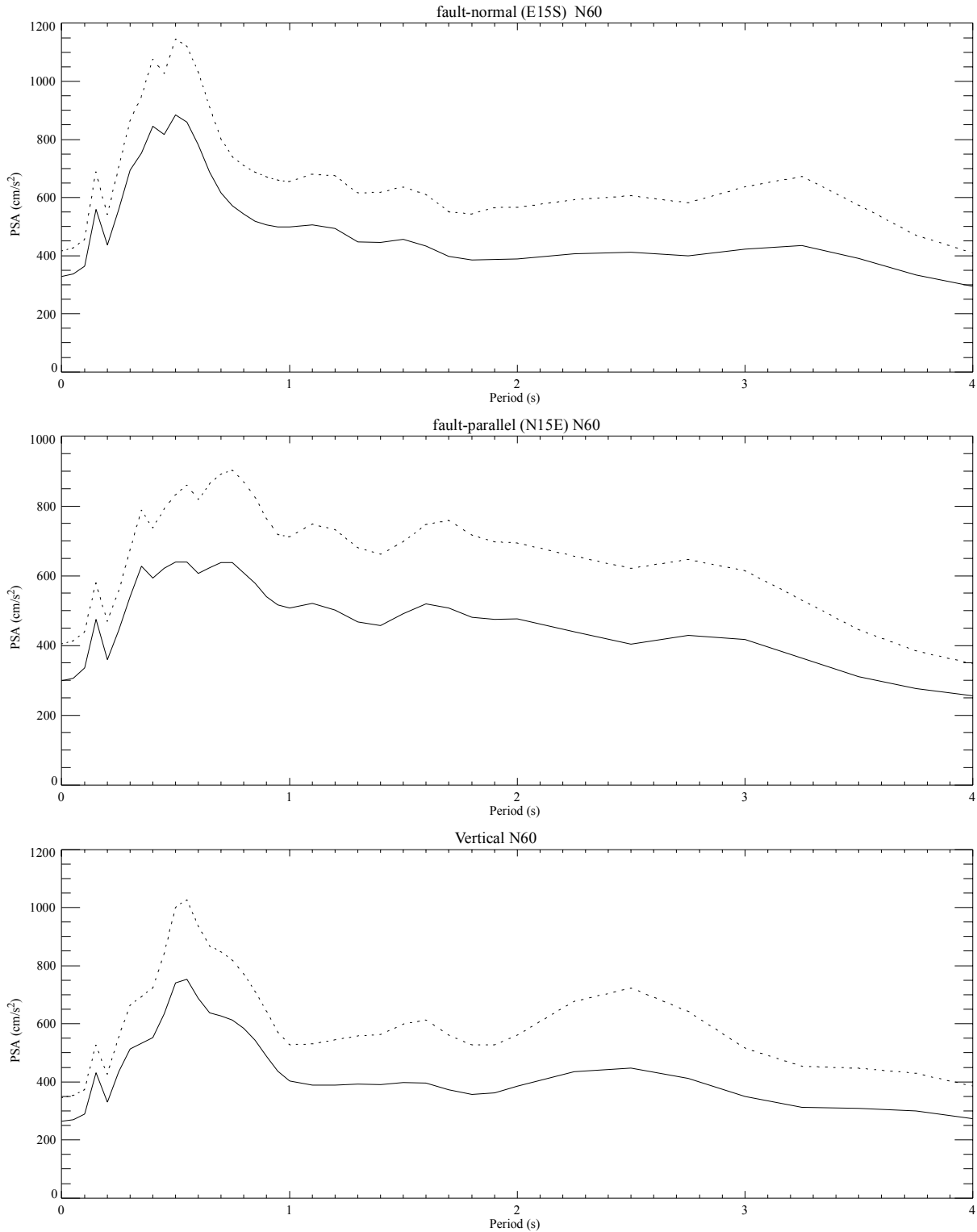


Figure 6-28: JLDW rock site PSA response spectra for a 60°-dipping northern Teton fault segment using all hypocenter positions. Mean curves are solid and 84% quantile curves are dotted. Components are as labeled.

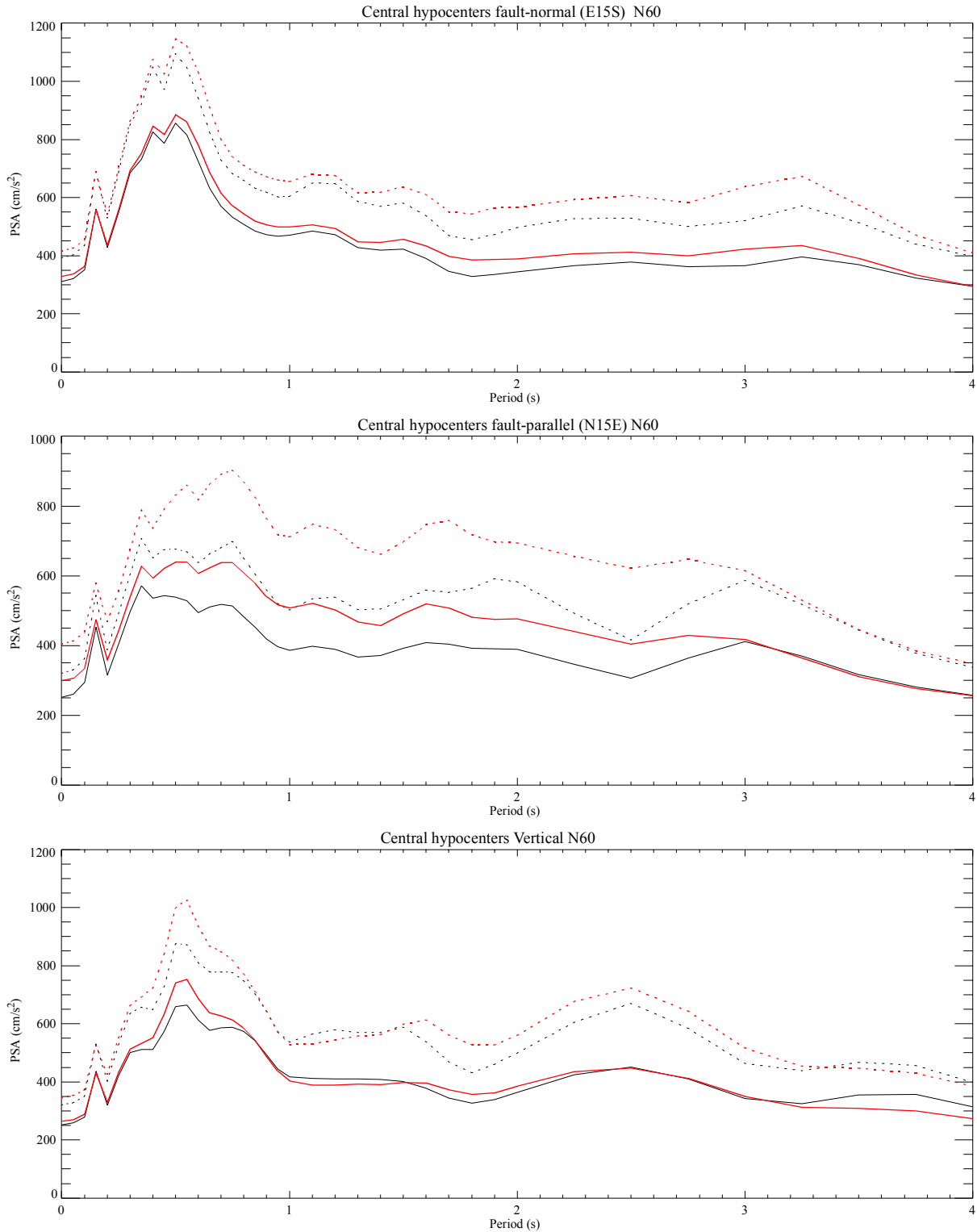


Figure 6-29: JLDW rock site central hypocenter PSA response spectra for a 60°-dipping northern Teton fault segment (black). Red curves are reference mean (solid) and 84% quantile (dotted) results using all hypocenters (from Figure 6-28). Components are as labeled.

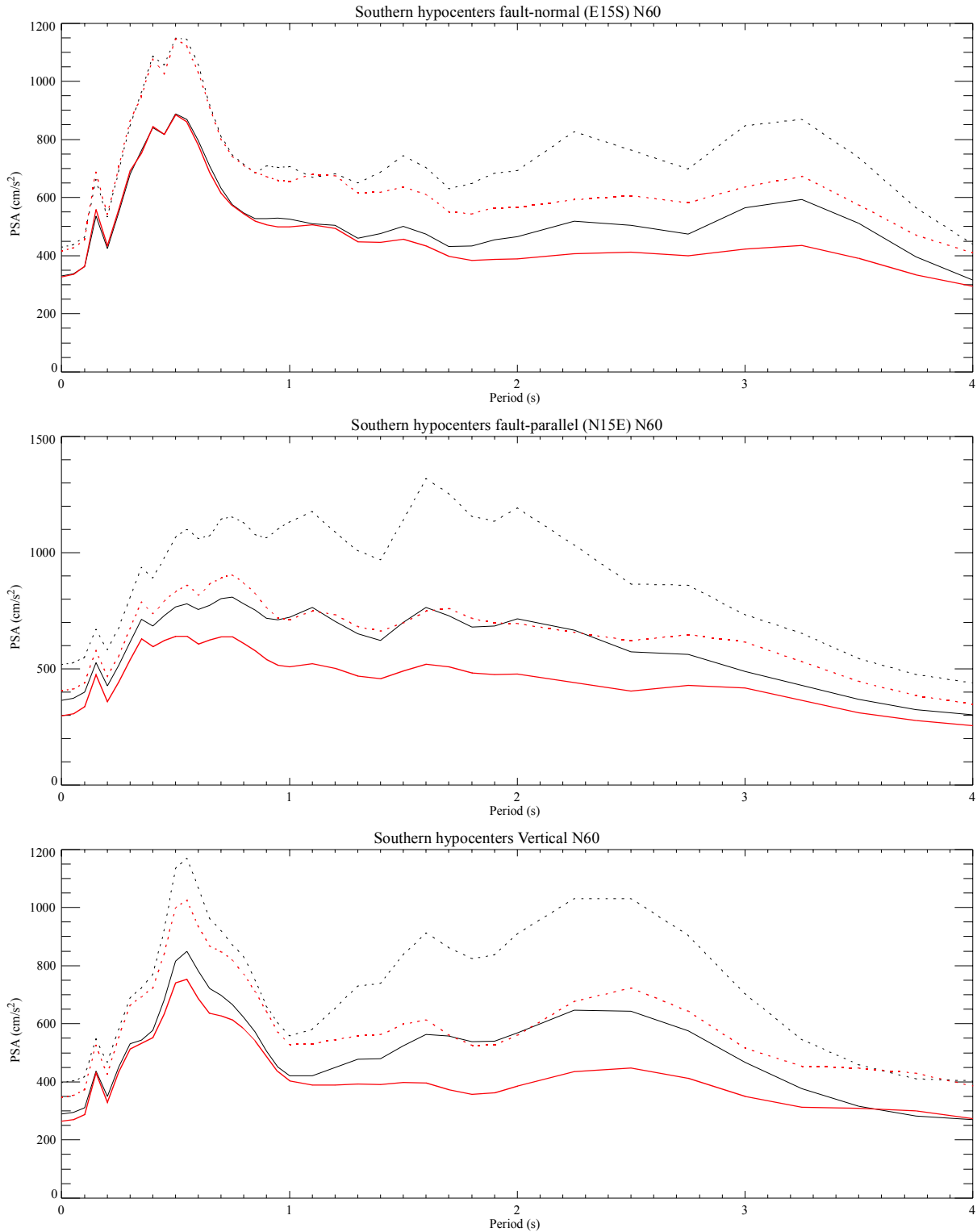


Figure 6-30: JLDW rock site southern hypocenter PSA response spectra for a 60°-dipping northern Teton fault segment (black). Red curves are reference mean (solid) and 84% quantile (dotted) results using all hypocenters (from Figure 6-28). Components are as labeled.

mean and 84% PSA responses for all hypocenter positions (Figure 6-31). Vertical PSA responses to southern hypocenters are strongly amplified between 1.5 s and 3 s period for a fault dip of 60° (Figure 6-30), similar to the southern hypocenter vertical PSA results for a fault dip of 45° (Figure 6-26), but extending over a broader period range.

The rupture area for the 60°-dipping fault is nearly half the rupture area of the 35°-dipping fault, and for a 60° dip none of the fault projects beneath the dam (Figure 6-4). Consequently, mean (Figure 6-32) and 84% (Figure 6-33) horizontal response spectra are generally lower than Spudich et al. (1999) rock responses. The site to source distance definition for Spudich et al. (1999) only changes to 2 km for a 60° fault dip from 0 km for 35° and 45° fault dips. Consequently, the Spudich et al. (1999) relations do not predict the reduced short period directivity indicated by the simulated ground motions because the distances, defined using the criteria of Joyner et al. (1994), hardly change. Joyner et al. (1994) intended distance to act as a proxy for directivity (W. Joyner, pers. comm.), as opposed to concocting a hanging wall definition of directivity, such as Abrahamson and Silva (1997). Consequently, the Spudich et al. (1999) relations probably overpredict the influences of directivity for a fault dip of 60° and may underpredict directivity effects for a fault dip of 35°. Both mean and 84% PSA responses on both horizontal components substantially exceed Spudich et al. (1999) PSA responses for periods > 2 s.

6.4.4 Comparison of Linear Ground Motions for Varying Fault Dips. The assumed dip of the northern Teton fault segment strongly influences peak ground motion responses. Fault-normal component peak ground motion responses for a dip of 35° are 50% to 100% larger than corresponding responses for a dip of 60° in the 0.5 s to 2.0 s period range (Figure 6-34); fault-parallel responses are about 30% larger for periods < 1 s and > 3 s and vertical responses are about 20% larger. The net effect of systematically increasing both horizontal peak responses for a dip of 35° relative to a dip of 60° is that peak horizontal acceleration responses are about twice as large for a fault dip of 35°. PSA responses for a fault dip of 45° are also systematically higher than 60° responses (Figure 6-35); peak horizontal PSA responses for a fault dip of 45° are systematically about 50% larger than 60° fault dip responses for periods < 2 s. The smallest changes in PSA responses occur between dips of 35° and 45° (Figure 6-36). Fault-normal PSA responses generally increased only about 20%-30% for periods < 2 s when dip was reduced from 45° to 35°.

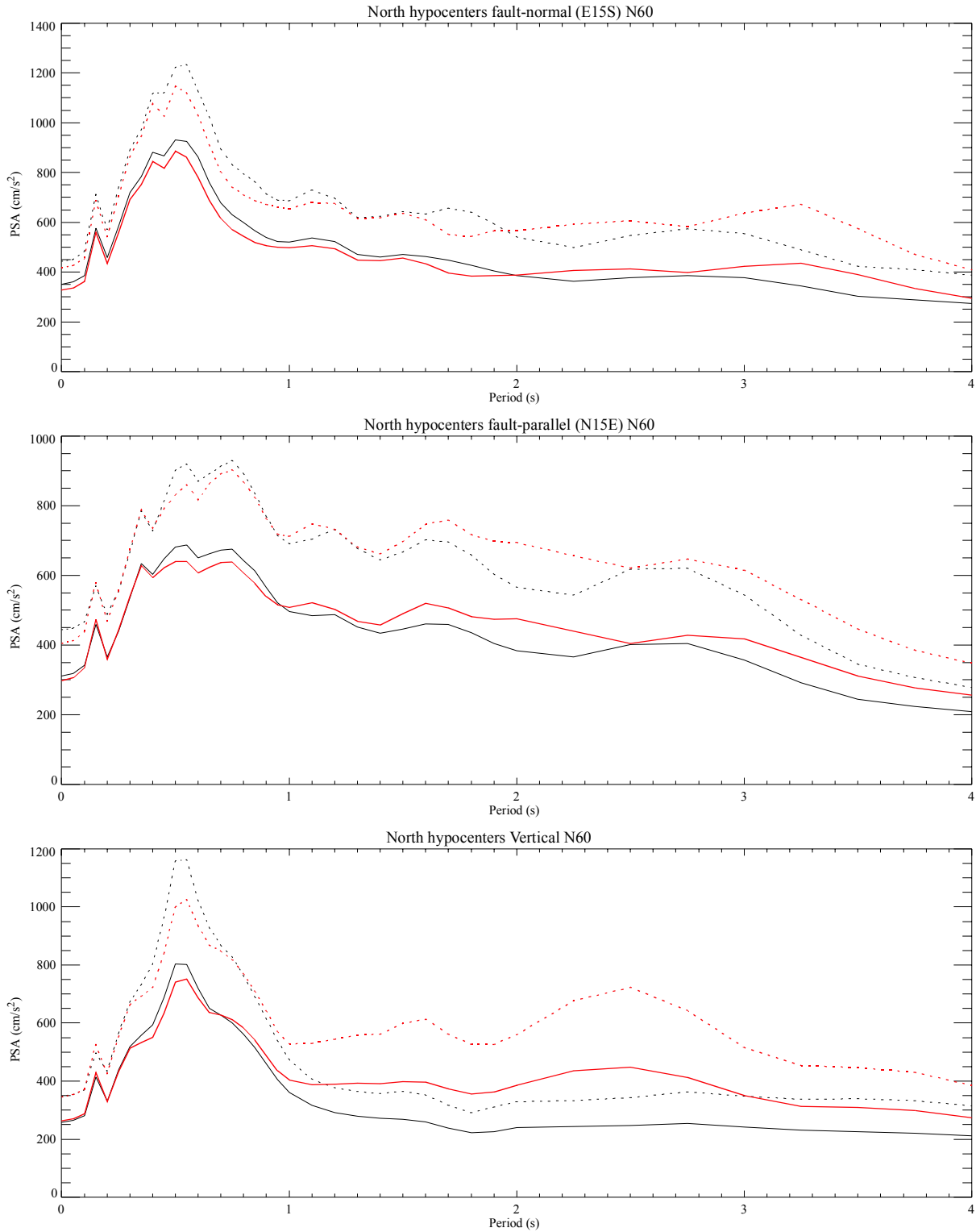


Figure 6-31: JLDW rock site northern hypocenter PSA response spectra for a 60°-dipping northern Teton fault segment (black). Red curves are reference mean (solid) and 84% quantile (dotted) results using all hypocenters (from Figure 6-28). Components are as labeled.

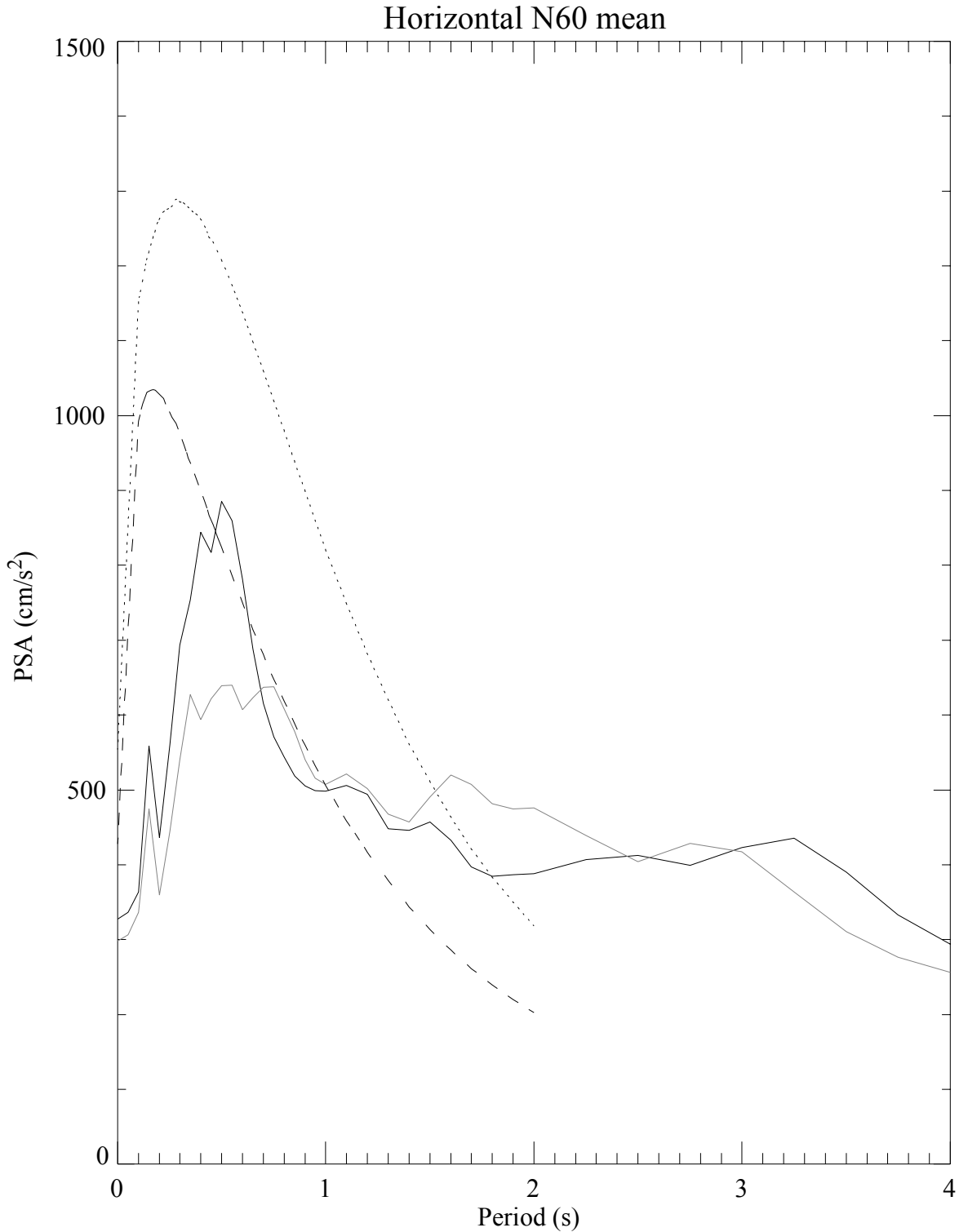


Figure 6-32: JLDW rock site mean PSA horizontal response spectra for a 60°-dipping northern Teton fault segment. The E15S component is solid and the N15E component is gray. SEA99 average horizontal component estimates for a M 6.9 normal-faulting earthquake are shown for soil (dotted) and rock (dashed) site conditions.

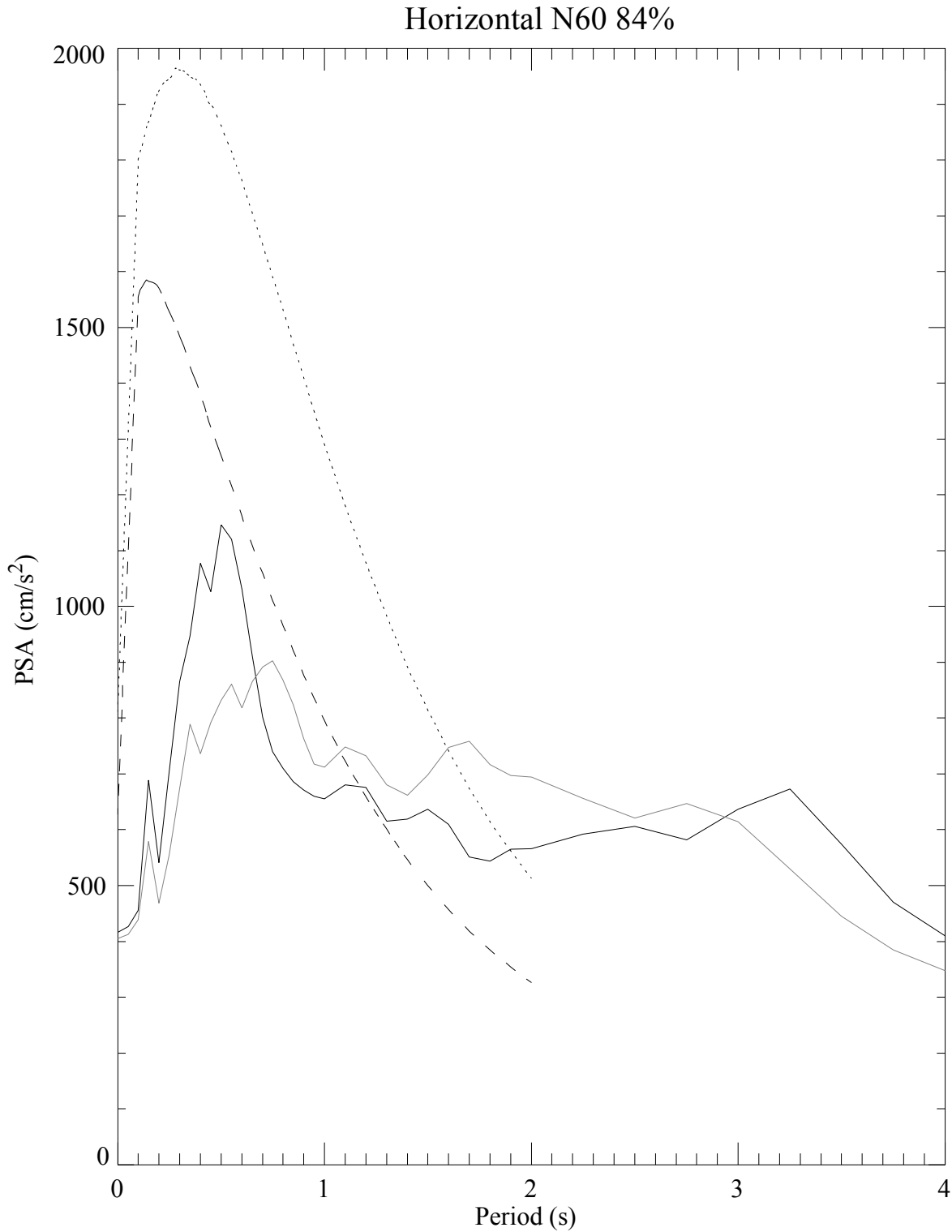


Figure 6-33: JLDW rock site 84% quantile PSA horizontal response spectra for a 60°-dipping northern Teton fault segment. The E15S component is solid and the N15E component is gray. SEA99 average horizontal component estimates for a **M** 6.9 normal-faulting earthquake are shown for soil (dotted) and rock (dashed) site conditions.

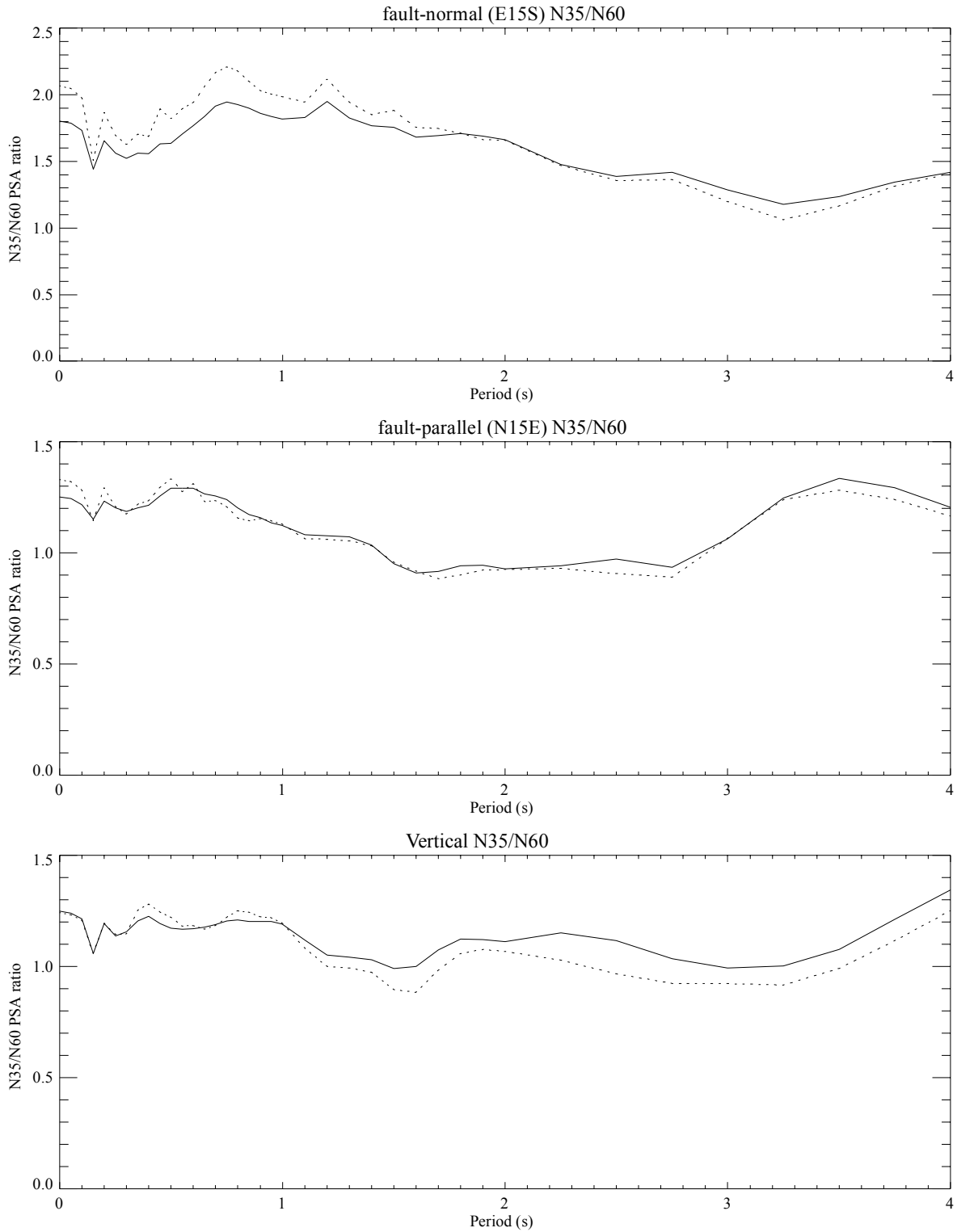


Figure 6-34: JLDW rock site ratios of 35°-to-60°-dipping northern Teton fault segment PSA response spectra. Mean curves are solid and 84% quantile curves are dotted for components as labeled.

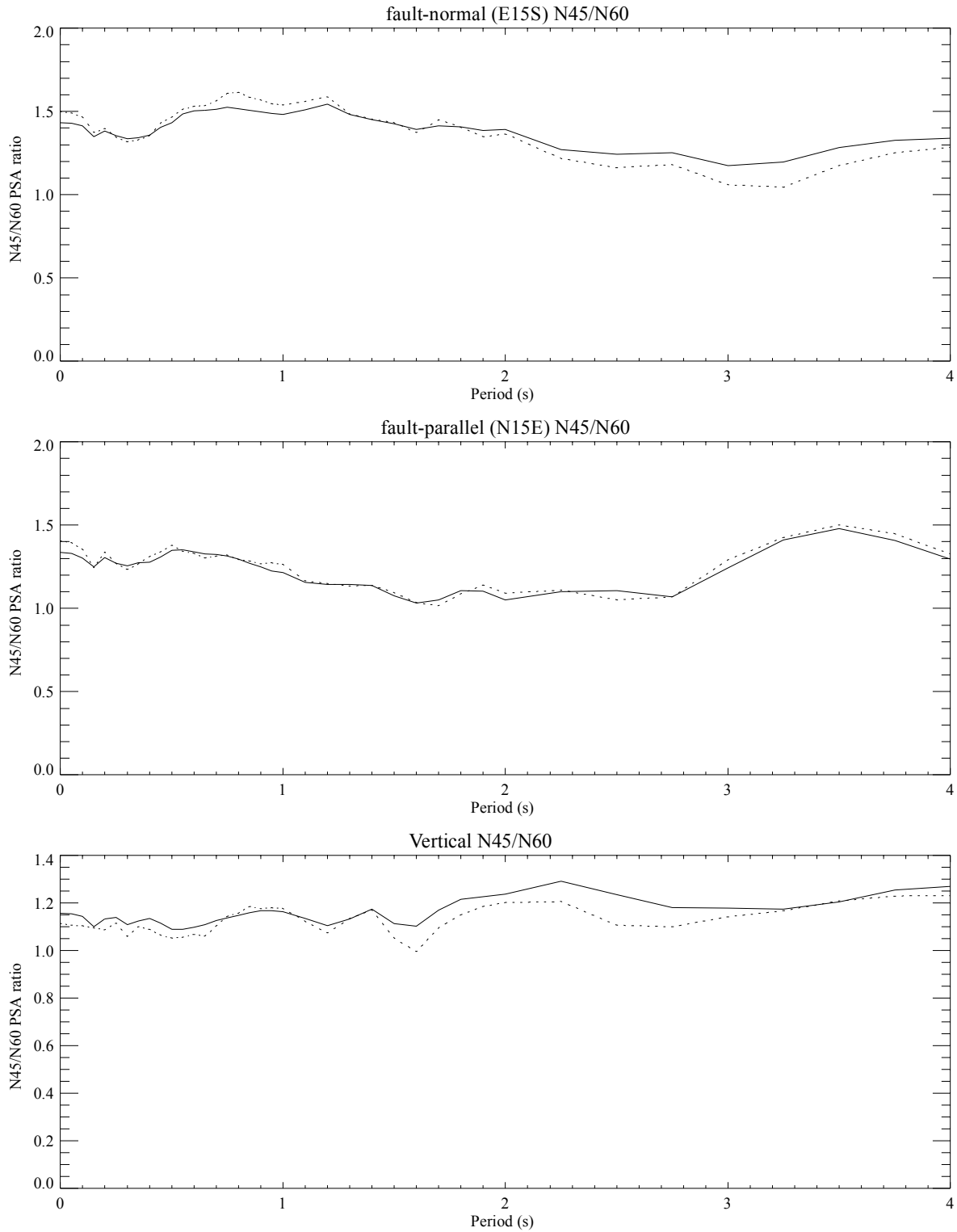


Figure 6-35: JLDW rock site ratios of 45°-to-60°-dipping northern Teton fault segment PSA response spectra. Mean curves are solid and 84% quantile curves are dotted for components as labeled.

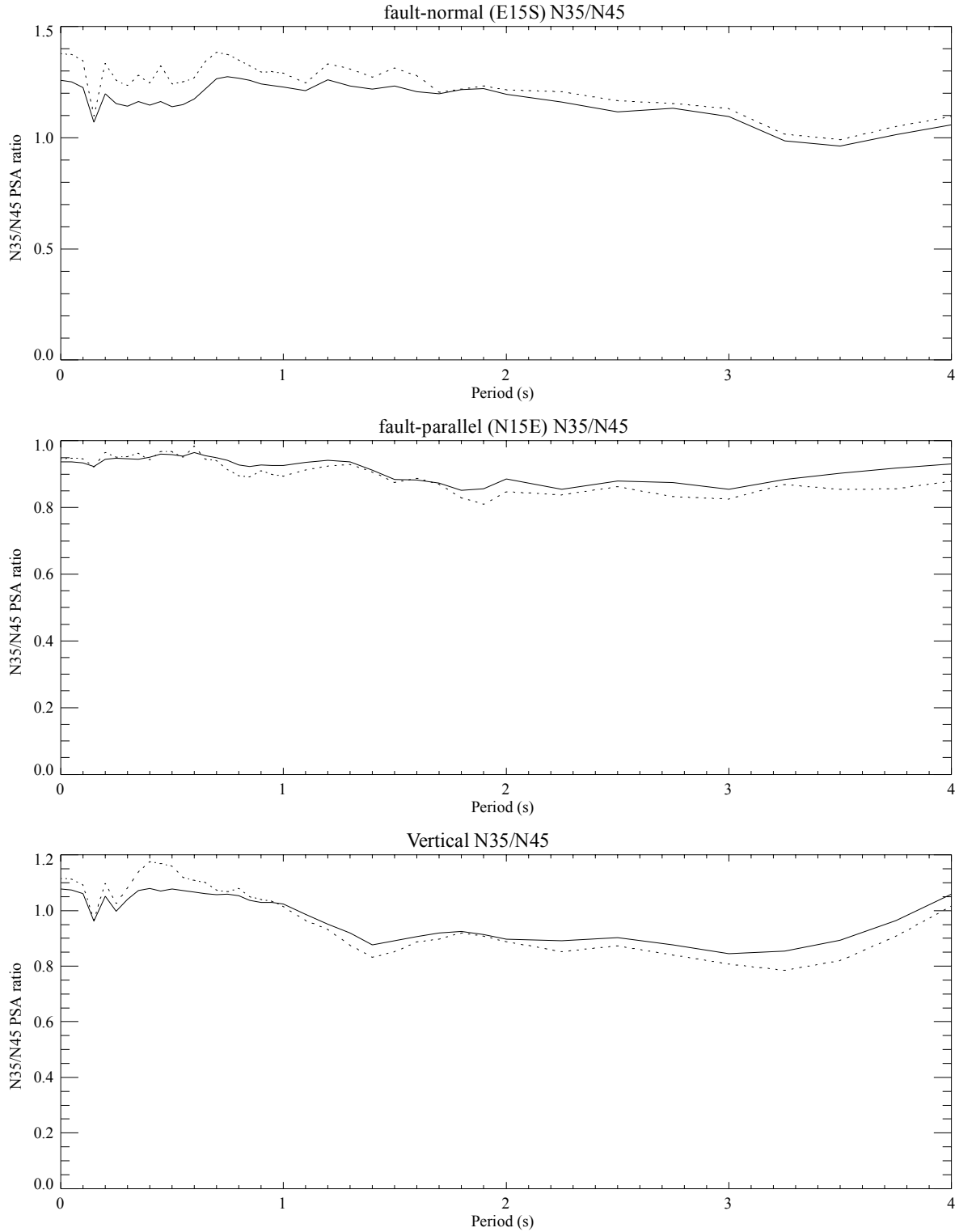


Figure 6-36: JLDW rock site ratios of 35°-to-45°-dipping northern Teton fault segment PSA response spectra. Mean curves are solid and 84% quantile curves are dotted for components as labeled.

fault-parallel motions actually decreased 10%-20%, and vertical motions showed modest changes. Thus, the largest change in peak ground motion acceleration responses is between fault dips of 60° (smallest peak response) to 45°. The 60° fault dip peak responses do show potentially very large long-period vertical responses that are larger over a broader range of periods than for a fault dip of 45°, but otherwise, both the 45° and 35° fault dip PSA responses are much larger than the 60° fault dip PSA responses. If definitive constraints on fault dip become available, particularly if the fault dip is found to be about 60°, then seismic loads at Jackson Lake Dam are likely to be significantly smaller than those recommended for dynamic analyses of the dam in the next section.

6.5 Ground Motions for Dynamic Analyses of the Concrete Portion of Jackson Lake Dam.

Jackson Lake Dam is a complex dam consisting of concrete and embankment sections founded on rock and soil. The concrete section of the dam is primarily founded on overcompacted glacial till and tuff with ~1 km/s near-surface shear wave velocities similar to site JLDW (Sirles, 1986). Ground motions for use in engineering analyses of the embankment section are provided in the Section 6.6. Ground motion developed using the responses calculated at site JLDW are presented here for use in engineering analyses of the concrete section of the dam.

The northern section of the concrete section of the dam is located adjacent to site JLD2, which shows some amplification relative to site JLDW (Section 5). While this report provides ground motions with JLDW site characteristics for engineering analyses of the concrete section of the dam, it may also be valuable to use these JLDW ground motions convolved with JLD2 responses for dynamic engineering analyses. While ground motions modified to contain the amplification observed at station JLD2 are not provided in this report, they can be produced if needed.

There are no $M \sim 7$ normal-faulting ground motion recordings from hanging wall sites located in low-velocity basins (Spudich et al., 1999). Consequently, other ground motion sources must be used to supply three-component acceleration time histories suitable for dynamic analyses of the concrete portion of the dam founded on “rock”. Two broadband synthetic ground motions produced in Section 6.4 are selected for dynamic analyses of the concrete portion of the dam and

one strong motion recording is recommended to provide extended high-frequency durations absent from the synthetic ground motions.

Since the peak ground motions strongly dependent on the assumed dip of the Teton fault, it is necessary to decide which dip scenario is most representative of expected ground motions at the dam. As discussed in Section 2, worldwide $M > 5.5$ earthquake data for normal-faulting earthquakes indicate that normal-fault dips of $\leq 50^\circ$ comprise 76% of the normal-faulting earthquakes (Collettini and Sibson, 2001). The focal mechanism data in Section 3 allow for a Teton fault dip of 25° to 60° , but do not place strong constraints on fault dip. As discussed in Section 4, detailed waveform modeling of two earthquakes suggest that the northern Teton fault segment dips $< 50^\circ$. Normal fault dips vary widely in the western United States. Abbott et al. (2001) suggest that the 16 Dec. 1954 M 6.8 Dixie Valley earthquake, Nevada, occurred on a 30° -dip normal fault. However, Doser (1986) found that the nearby 16 Dec. 1954 M 7.1 Fairview peak earthquake occurred on an oblique-slip normal fault dipping 60° and the largest magnitude Rainbow Mountain earthquake, M 6.8 24. Aug. 1954, occurred on an oblique-slip normal faulting dipping 50° . The primary difference between these three normal faults is that purely normal slip was inferred for the 30° -dip Dixie Valley fault and oblique normal-slip was inferred for the more steeply-dipping normal faults. Doser and Smith (1989) studied source parameters for 50 $M \geq 5.5$ earthquakes in the cordillera of the western United States and found that fault dips were $\geq 38^\circ$ and found no evidence for listric low angle planer faulting (very low dips). The largest ISB crustal normal-faulting earthquake with a well constrained focal mechanism is the 1983 M 7.3 Borah Peak, Idaho, earthquake with a inferred dip of 45° (see Doser and Smith, 1989, for complete references). The local and region evidence for normal-faulting dip suggests that the 35° and 45° fault dip ground motion scenarios represent the most likely dip scenarios for the Teton fault. In view of the lack of any definitive information indicating that the northern Teton fault rupture segment dips $> 50^\circ$, the 60° fault dip ground motion scenarios are not discounted for the purposes of recommending ground motions for dynamic analyses of Jackson Lake Dam. Although a fault dip of 45° is plausible, the ground motions producing using a fault dip of 35° are recommended for dynamic analyses of Jackson Lake Dam for the following reasons:

1. Doser and Smith (1989) found that unilateral rupture dominated $M \geq 5$ earthquake ruptures in the extensional region of the western United States. The ground motion simulations in Section 6.4 showed larger acceleration responses for unilateral rupture scenarios, because LVB-edge S-waves and surface waves coincide with direct S-wave arrivals from fault rupture in most of the central portion of the fault, amplifying acceleration ground motion responses. Using global earthquake data, McGuire et al. (2002) conclude that about 80% of the ruptures of $M \geq 7$ earthquakes since 1994 were unilateral. Thus, the larger peak motions produced by a 35° fault dip serve as approximations to the amplified 45° fault dip motions associated with unilateral fault rupture.

2. Experimentation with correlated-random velocity randomization of the LVB in the 2D finite-difference ground motion simulations in Section 4 showed that fractal velocity randomizations with standard deviations of about 9% could reproduce the long coda durations observed in microearthquake recordings at station JLDW. It would be necessary to run a suite of velocity randomizations of the 3D crustal velocity model to investigate the influence of random velocity variations on peak ground motion amplitudes and ground motion durations. Since each 3D Green's function calculation required several days to compute and more time to setup and process, it was not feasible to conduct such an investigation and maintain the project schedule. Synthetic ground motion durations are likely underestimated because most the 3D crustal velocity model is relatively smooth, and because it was necessary to limit the total duration of the EGFs to accomplish the ground motion simulations in a timely fashion. Consequently, the synthetic ground motion durations for a fault dip of 35° are likely more representative of expected ground motion durations for a fault dip of 45° , and synthetic ground motion durations for a fault dip of 45° are more likely to represent expected ground motion durations for a fault dip of 60° . Consequently, the 35° -dipping Teton fault results are most likely to contain durations adequate for dynamic analyses of Jackson Lake Dam.

3. Normal fault ruptures are likely to be more complex than the kinematic rupture models used to simulation ground motions in Section 6.4. Oglesby et al. (1998; 2000) considered the consequences of the free surface on the dynamic rupture characteristics of dipping faults

using 2D and 3D finite-element models. One consequence of the free-surface boundary condition on stress is that for normal faults with dip angles between about 30° and 75° , fault rupture proceeding from the bottom of the fault toward the free surface brings the fault near the free surface closer to failure than it would have been in a whole space. This effect is predominantly due to the decrease in normal stress on the fault with a resultant decrease in the yield frictional stress. In some circumstances, this effect can lead to the rupture front jumping ahead (a secondary nucleation) near the free surface of a normal fault. After rupture proceeds downdip from the free-surface, normal stresses increase behind the rupture (Oglesby et al., 1998), which may cause the downdip rupture region to heal near the surface prior to the onset of updip rupture, in effect producing two distinct slip events along the shallow portions of the fault. This dynamic rupture behavior may explain the tendency for some normal faults to produce surface slips that appear out of proportion relative to the surface scarp lengths (Wells and Coppersmith, 1994). The implications for ground motions at Jackson Lake Dam is that excitation of LVB-edge S-waves near the Teton fault could occur twice during an earthquake, once when rupture jumps to the free surface and proceeds down dip, and once when rupture preceding updip and intersects the free surface. As shown in Section 4, S-waves produced along the shallow portion of the Teton fault produce large-amplitude LVB-edge S-waves at the dam, due to the focusing effects of the LVB structure. The dynamic rupture simulations results for normal faults of Oblesby et al., (1998;), specifically the tendency for rupture to discontinuously jump to the free surface and produce enhanced slip and multiple slip velocity pulse in the shallow region of the normal fault, were reproduced using the 3D finite-difference approach of Andrews (1999). The results are unlikely to change for different constitutive laws for fault slip (Bizzarri et al., 2001). Since these normal-faulting dynamic slip velocity effects are not included in the kinematic rupture model used to synthesize ground motions at the dam, a reasonable conclusion is that the simulated peak ground motions provide lower bounds on ground motion amplitudes at the dam, and may underestimate peak velocities and accelerations at the dam. In view of these factors, it appears that the peak amplitudes associated with the 35° -dipping Teton fault are likely to be more representative of ground motion associated with a 45° -dipping fault, and peak amplitudes associated with the 45° -dipping Teton fault are likely to be more representative of ground motions associated with a 60° -dipping Teton

fault. Consequently, the 35°-dipping Teton fault results are most likely to contain adequate durations to use for dynamic analyses of Jackson Lake Dam.

4. The rock motions were simulated for the rock reference site JLDW, which is located ~200 m east of the easternmost section of Jackson Lake Dam. As shown in Section 6.4, peak ground motion amplitudes decrease east of the dam. Consequently, rock motions at Jackson Lake Dam will probably be moderately larger than ground motions computed at site JLDW. This is another factor that supports substituting lower-dip ground motion estimates for the next larger dip to provide more representative seismic loads at the dam.

5. The summation of the EGF's LVB-edge S-waves is probably less constructive than would occur in practice since the EGF's are aligned on the first S-wave arrival, and the LVB-edge S-waves have travel-time moveouts that varying systematically between ~3 s and ~6 s, depending on the position of the fault source relative to the site. In contrast the EGF's have a wide variety of LVB-edge S-wave moveouts and are selected at random at each point-source integration point. Consequently, the EGF ground motions are likely to underestimate peak amplitudes somewhat, particularly in the 1 Hz to 6 Hz frequency band where coherent LVB-edge S-waves were observed and modeled in Section 4 using 2D finite-difference methods.

6. The EGF's were low-pass filtered at 6 Hz to ensure convergence of the point-source summations at high frequencies. Consequently, peak acceleration are likely lower bounds because there will be a nonzero contribution of frequencies > 6 Hz to ground motions that was not included in the simulated ground motions. This should not be a large effect because the site kappa estimated from the site responses at the JLDW rock site are large, on the order of 0.08, so seismic energy for frequencies > 6 Hz is naturally attenuated, although not as strongly as in the simulated ground motions.

In light of these seismic source and wave propagation complications, and the practical realities of simulating ground motions, the simulated 45°-fault-dip and 60°-fault-dip ground motions are discounted for the purposes of providing ground motions suitable for dynamic analyses of the dam. Our judgement is that the 35°-dipping ground motions are probably most representative of

expected ground motions for faults dips $< 50^\circ$, the most likely range of dips for the Teton fault, based on world-wide distributions of normal fault dips (Section 2) and the limited inferences that can be made about Teton fault dip from microearthquake data (Sections 3 and 4).

Response spectra from the 3300 simulated ground motions with a fault dip of 35° were compared to the mean and 84% response spectra to find the ground motion simulations that produced horizontal response spectra that most closely resembled mean and 84% PSA responses. Since the E15S horizontal component consistently had the largest PSA responses, it was used to as the basis for comparison. A simulated ground motion was found that closely reproduced the mean E15S PSA response from the 3300 simulations (Figure 6-37). The PHA (Figure 6-38) and PHV (Figure 6-39) responses are close to mean responses for a dip of 35° (PHA are the zero period PSA values). The acceleration time histories in Figure 6-38 were high-pass filtered to eliminate permanent displacement so these ground motions were compatible with typical requirements of dynamic engineering analyses programs. Consequently, the displacement seismograms (Figure 6-40) do not contain the significant permanent displacements associated with translation of the hanging wall during faulting. Significant accelerations, velocities, and displacements persist for > 60 s. These synthetic ground motions become artificially depleted of high-frequency responses after about 30 s because of the ~ 13.5 s limit on the EGF durations used in the ground motion simulations. However, it is expected that the predominant period of the ground motions will progressively shift toward longer periods with increasing time as large-scale LVB responses dominant the responses after ~ 35 s, just not as abruptly as indicated in Figures 6-38 and 6-39.

A simulated ground motion was found that closely reproduced the 84% E15S PSA response from the 3300 simulations (Figure 6-41). The durations of high-frequency accelerations (Figure 6-42) are shorter (~ 50 s of significant acceleration response) than for the mean scenario (Figure 6-38), consistent with amplification associated with rupture directivity producing the stronger 84% peak responses. Peak velocities are on the N15E component, although velocities > 100 cm/s persist longer on the E15S component (Figure 6-43). Strong velocities (> 20 cm/s) persist for ~ 40 s on the E15S and vertical components, indicating a strong response from the LVB (Figure 6-43), as is also evident in the horizontal displacements (Figure 6-44).

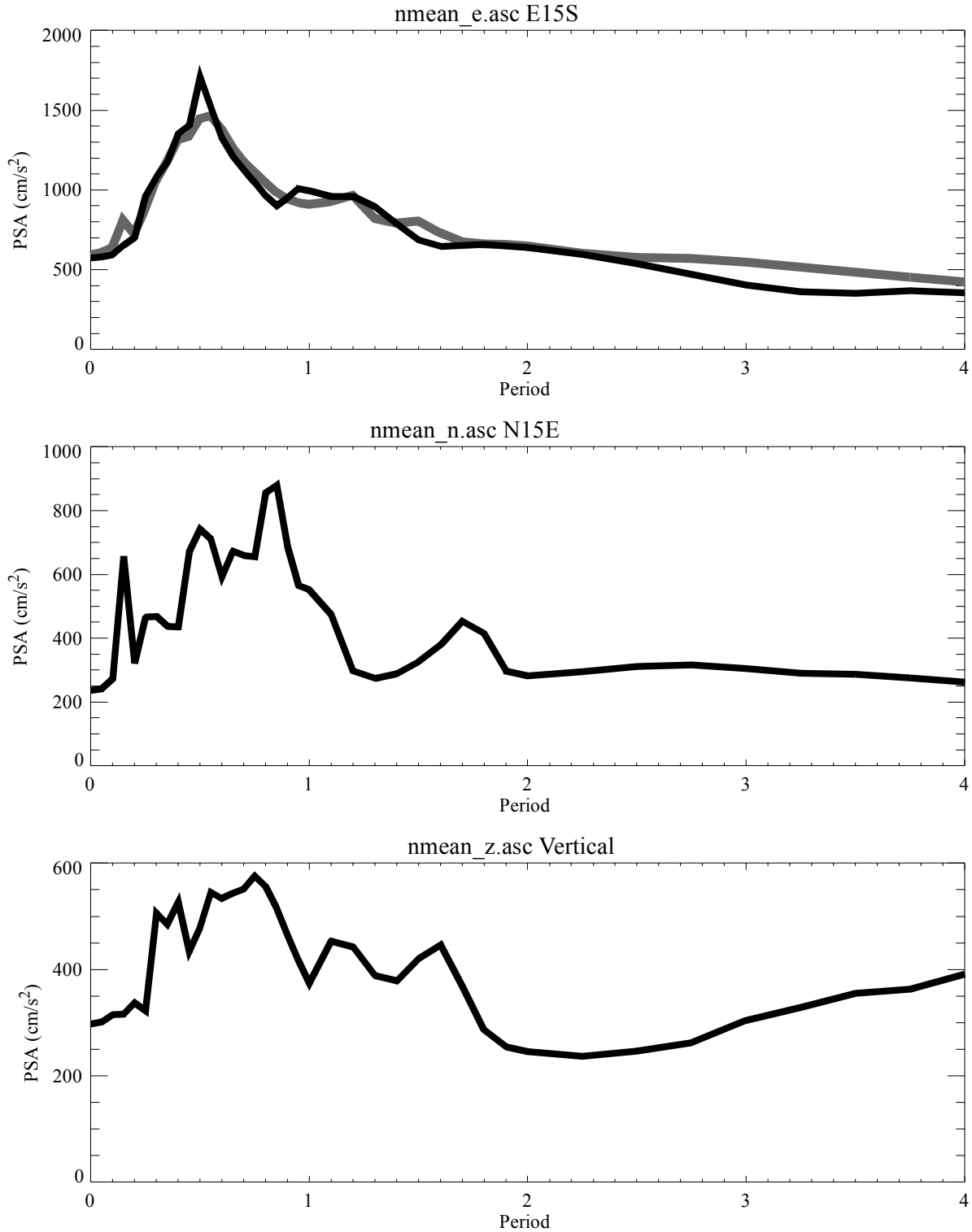


Figure 6-37: JLDW rock site PSA response spectra corresponding to the mean acceleration seismograms. Components are labeled with time history filename and component orientation. The arithmetic mean of the 3300 simulated response spectra for the upstream component for a fault dip of 35° are plotted as the grey curve for comparison at the top.

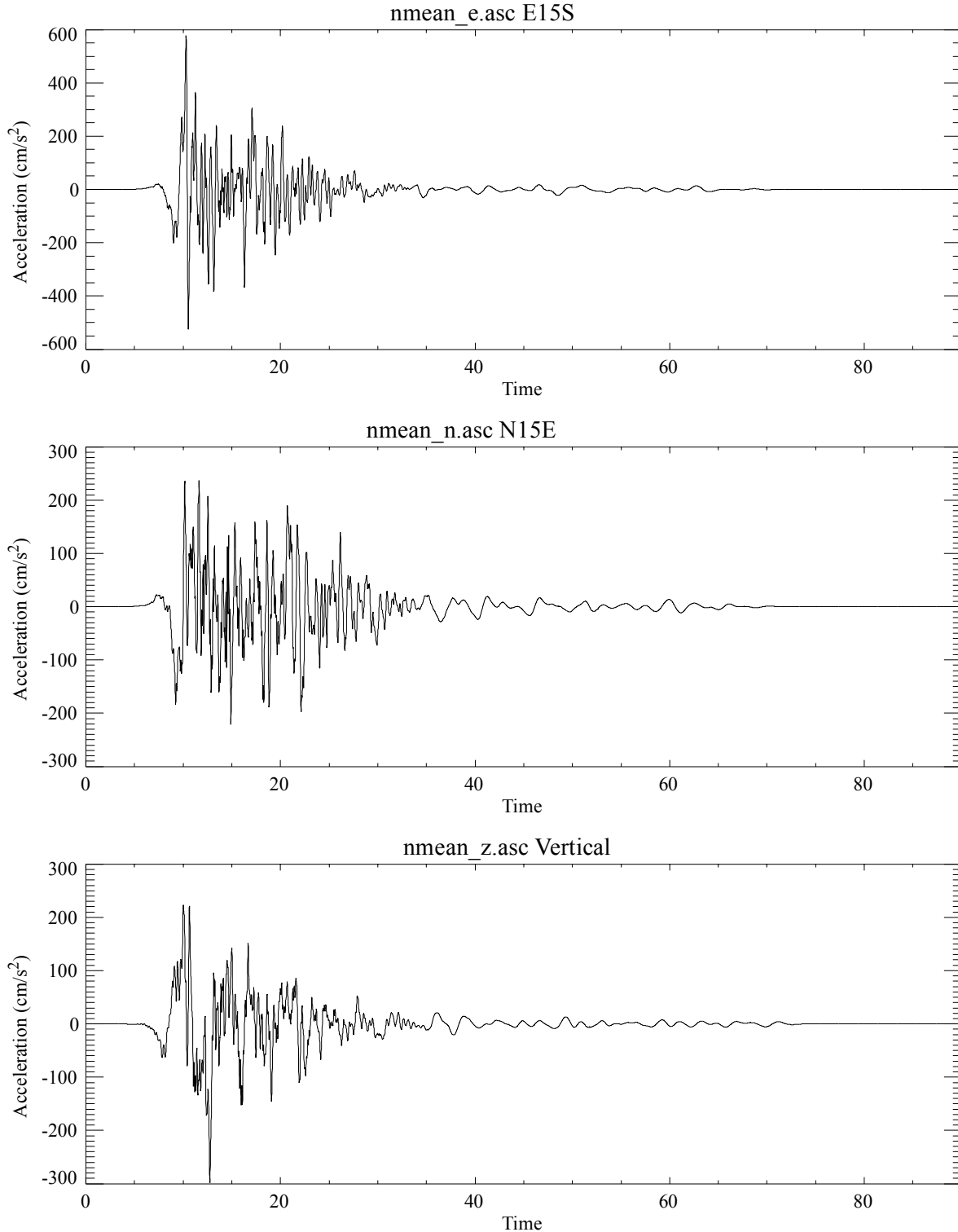


Figure 6-38: JLDW rock site mean acceleration seismograms for dynamic analyses of Jackson Lake Dam. Components are labeled with time history filename and component orientation, with horizontal components orientated upstream and cross canyon (along the dam axis). These seismograms correspond to the best-fitting acceleration response spectra to the mean of 3300 response spectra for a fault dip of 35°.

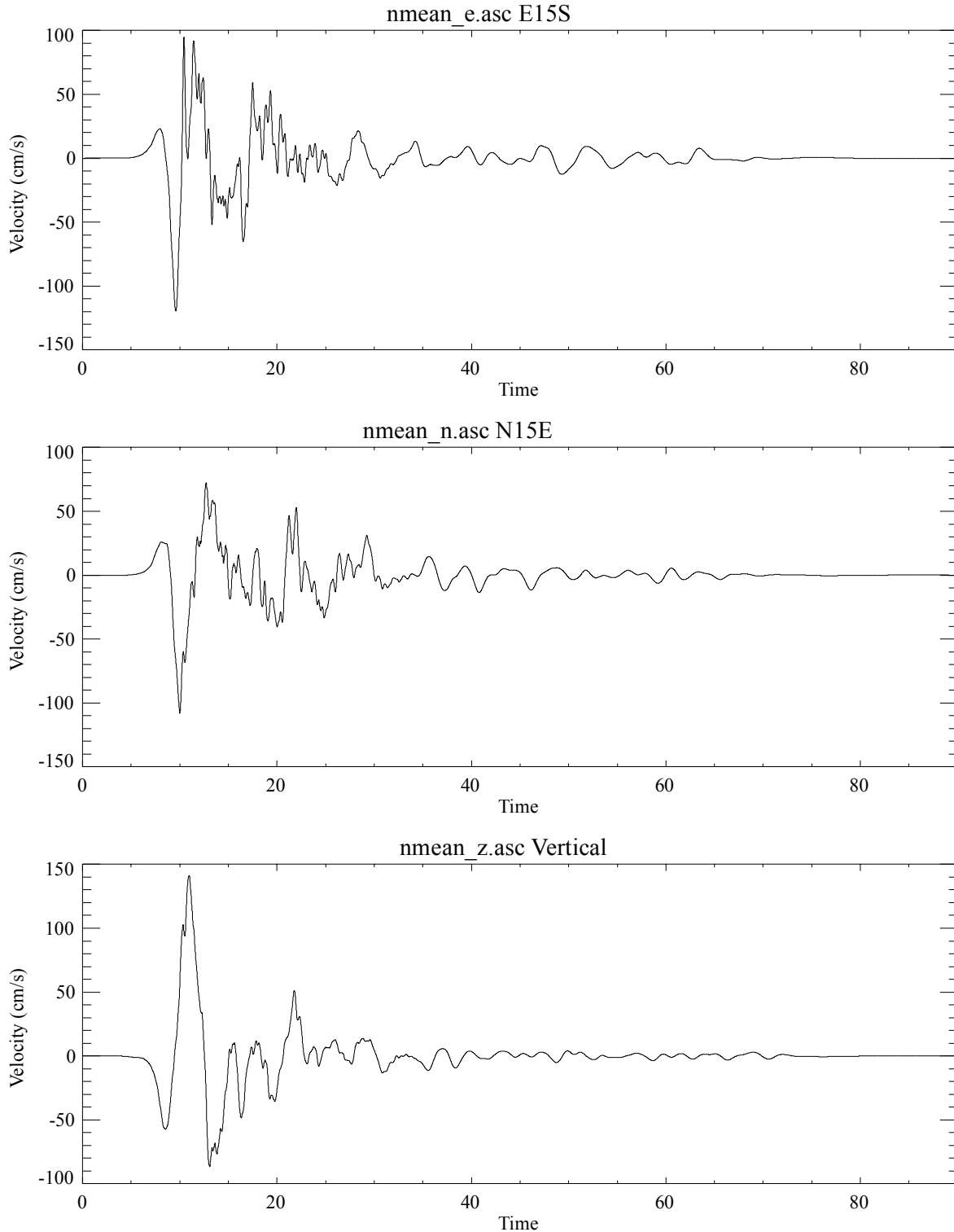


Figure 6-39: JLDW rock site mean velocity seismograms for dynamic analyses of Jackson Lake Dam. Components are labeled with time history filename and component orientation, with horizontal components orientated upstream and cross canyon (along the dam axis). These seismograms correspond to the best-fitting response spectra to the mean of 3300 acceleration response spectra for a fault dip of 35°.

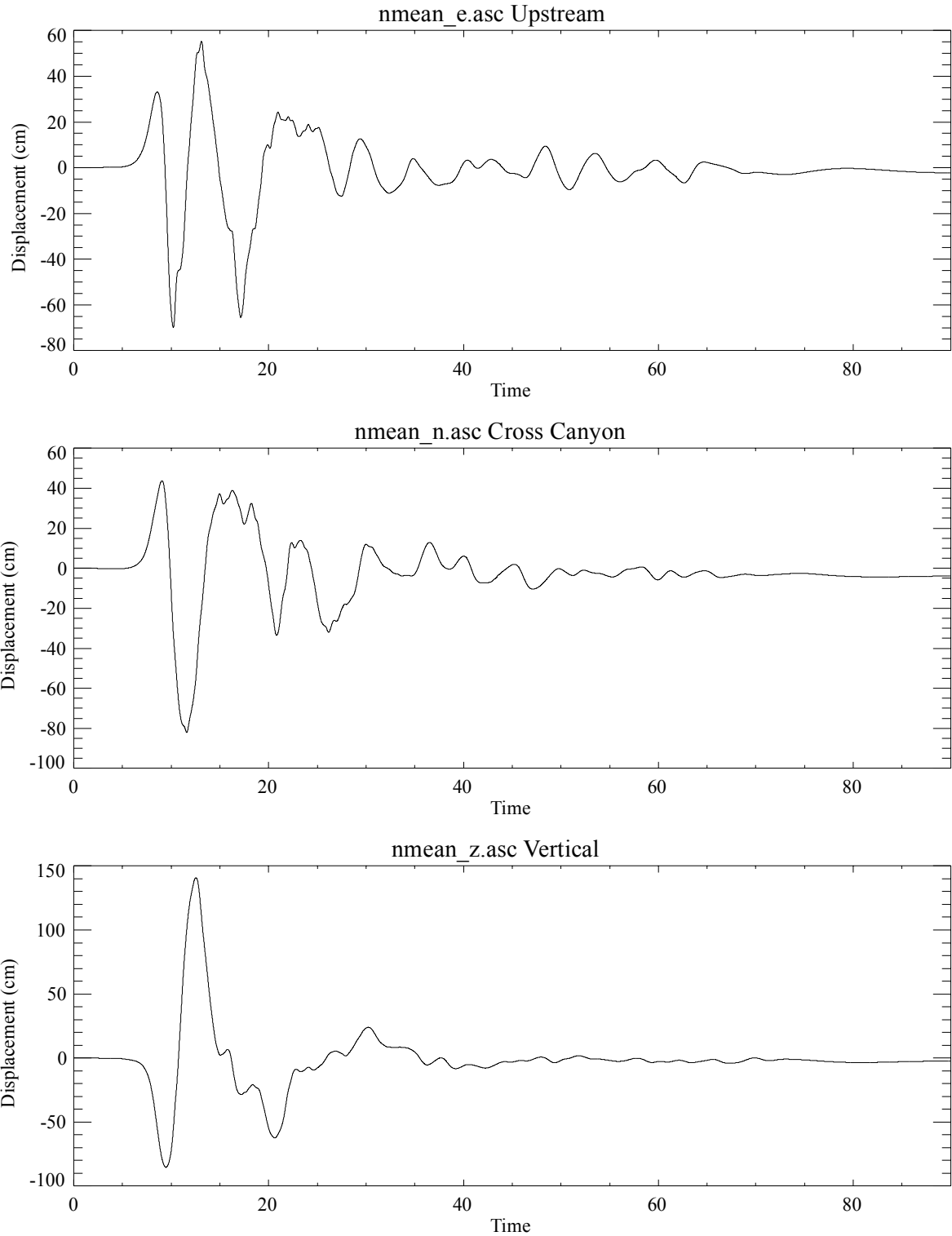


Figure 6-40: JLDW rock site mean displacement seismograms for dynamic analyses of Jackson Lake Dam. Components are labeled with time history filename and component orientation. These seismograms correspond to the best-fitting response spectra to the mean acceleration response spectra for a fault dip of 35°.

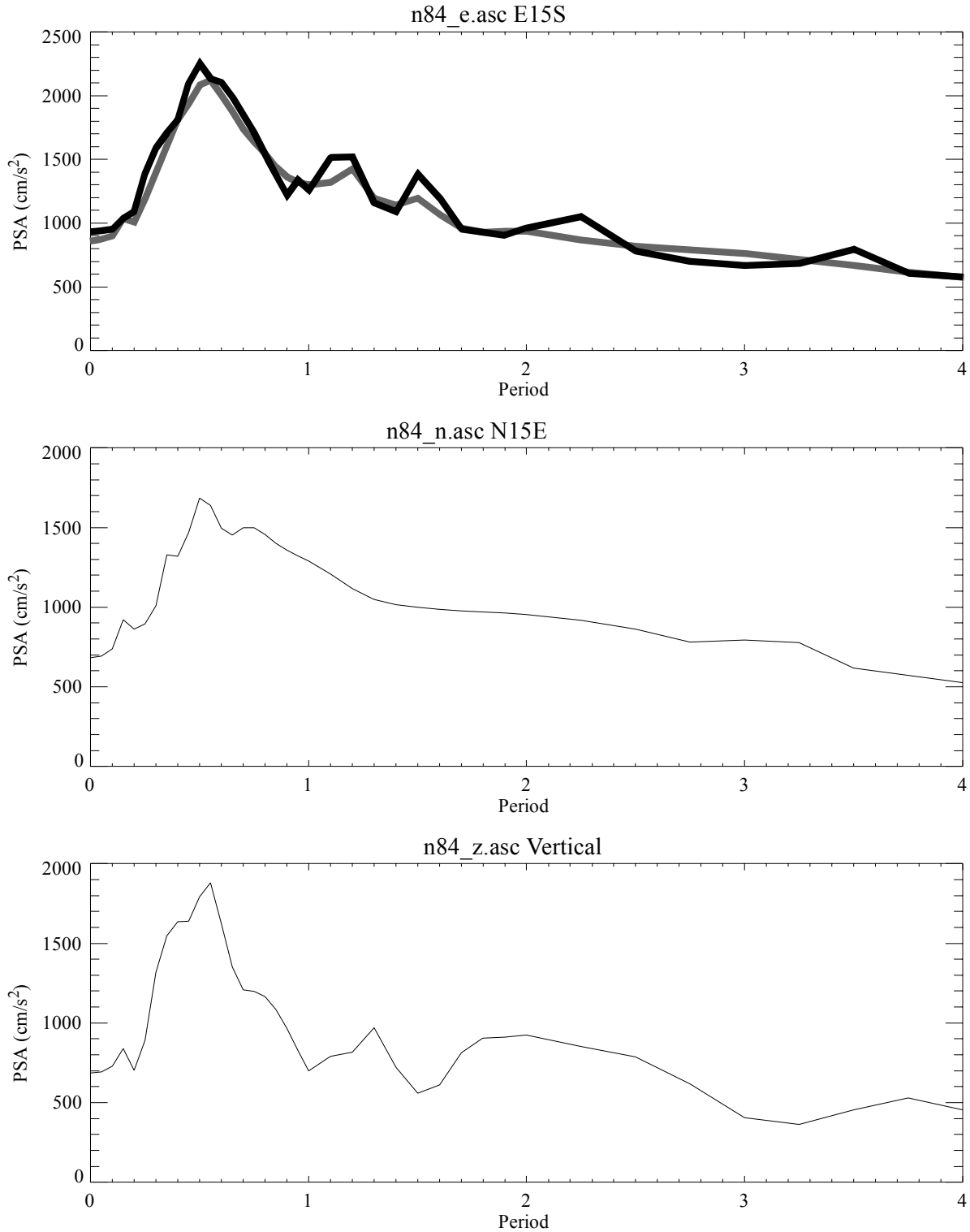


Figure 6-41: JLDW rock site PSA response spectra corresponding to the 84 percentile acceleration seismograms. Components are labeled with time history filename and component orientation. The 84% quantile from 3300 response spectra for the upstream component for a fault dip of 35° are plotted as the grey curve for comparison at the top.

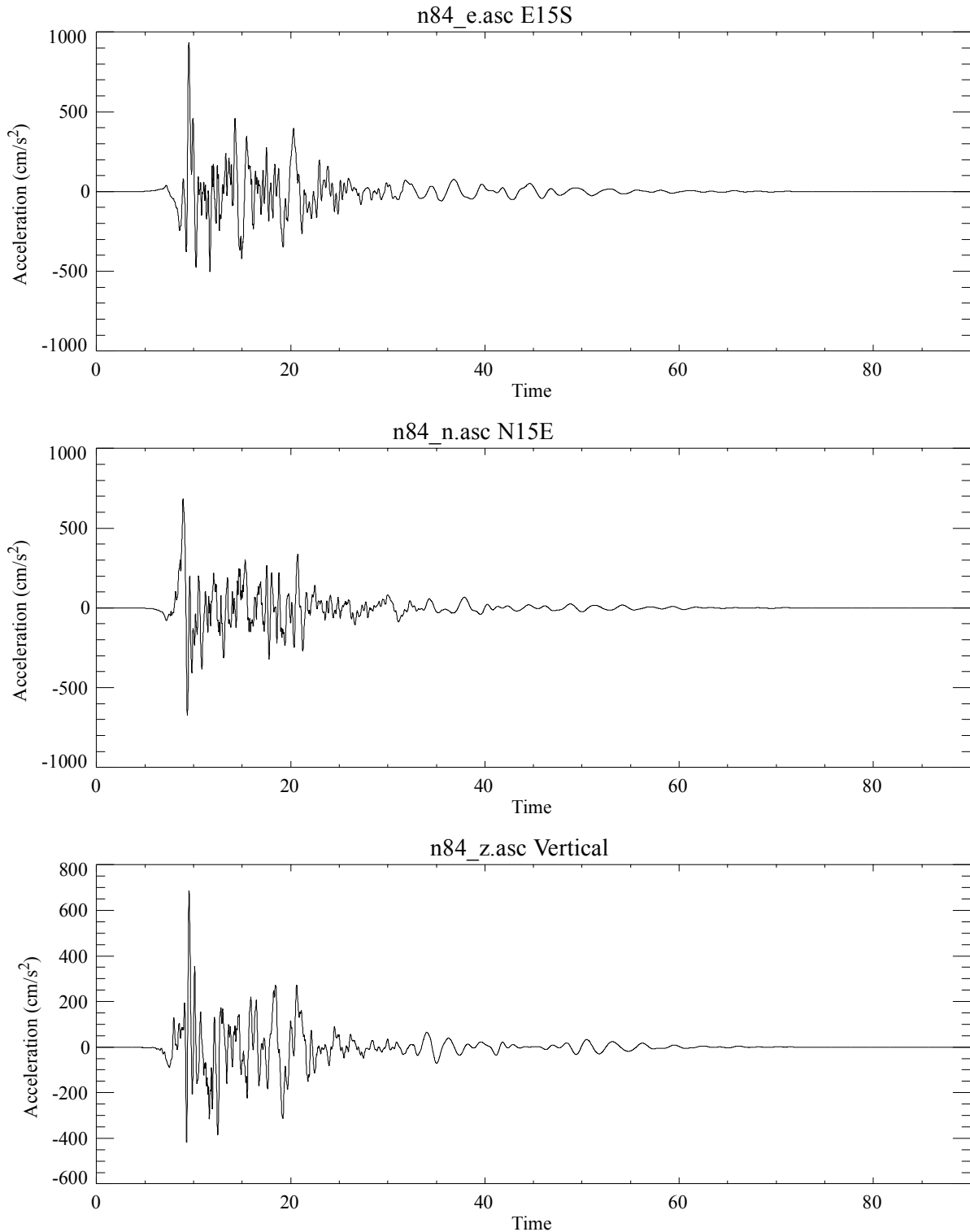


Figure 6-42: JLDW rock site 84 percentile acceleration seismograms for dynamic analyses of Jackson Lake Dam. Components are labeled with time history filename and component orientation, with horizontal components orientated upstream and cross canyon (along the dam axis). These seismograms correspond to the best-fitting acceleration response spectra to the 84 percentile response spectra from 3300 ground motion simulations for a fault dip of 35°.

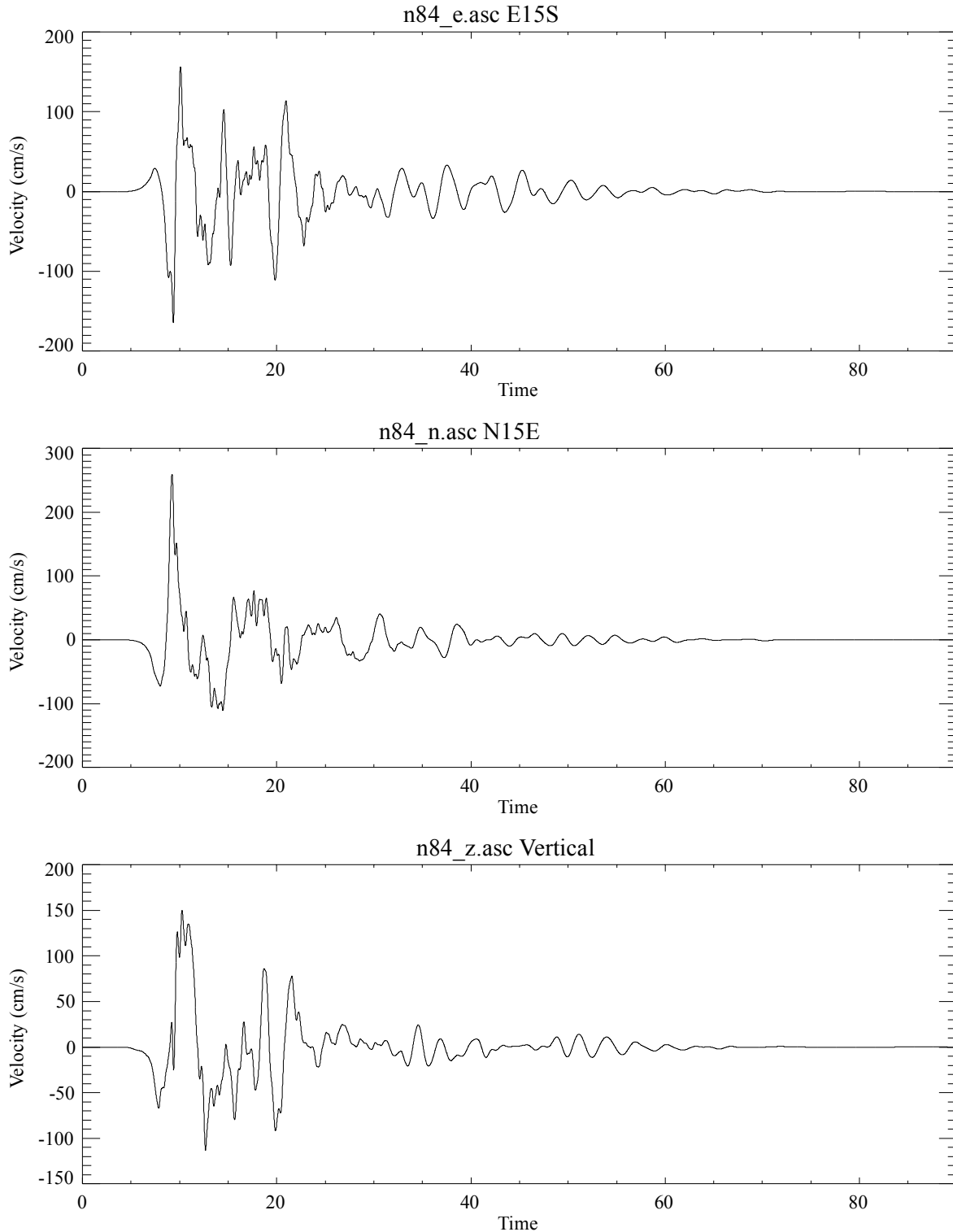


Figure 6-43: JLDW rock site 84 percentile velocity seismograms for dynamic analyses of Jackson Lake Dam. Components are labeled with time history filename and component orientation, with horizontal components orientated upstream and cross canyon (along the dam axis). These seismograms correspond to the best-fitting acceleration response spectra to the 84 percentile response spectra from 3300 ground motion simulations for a fault dip of 35°.

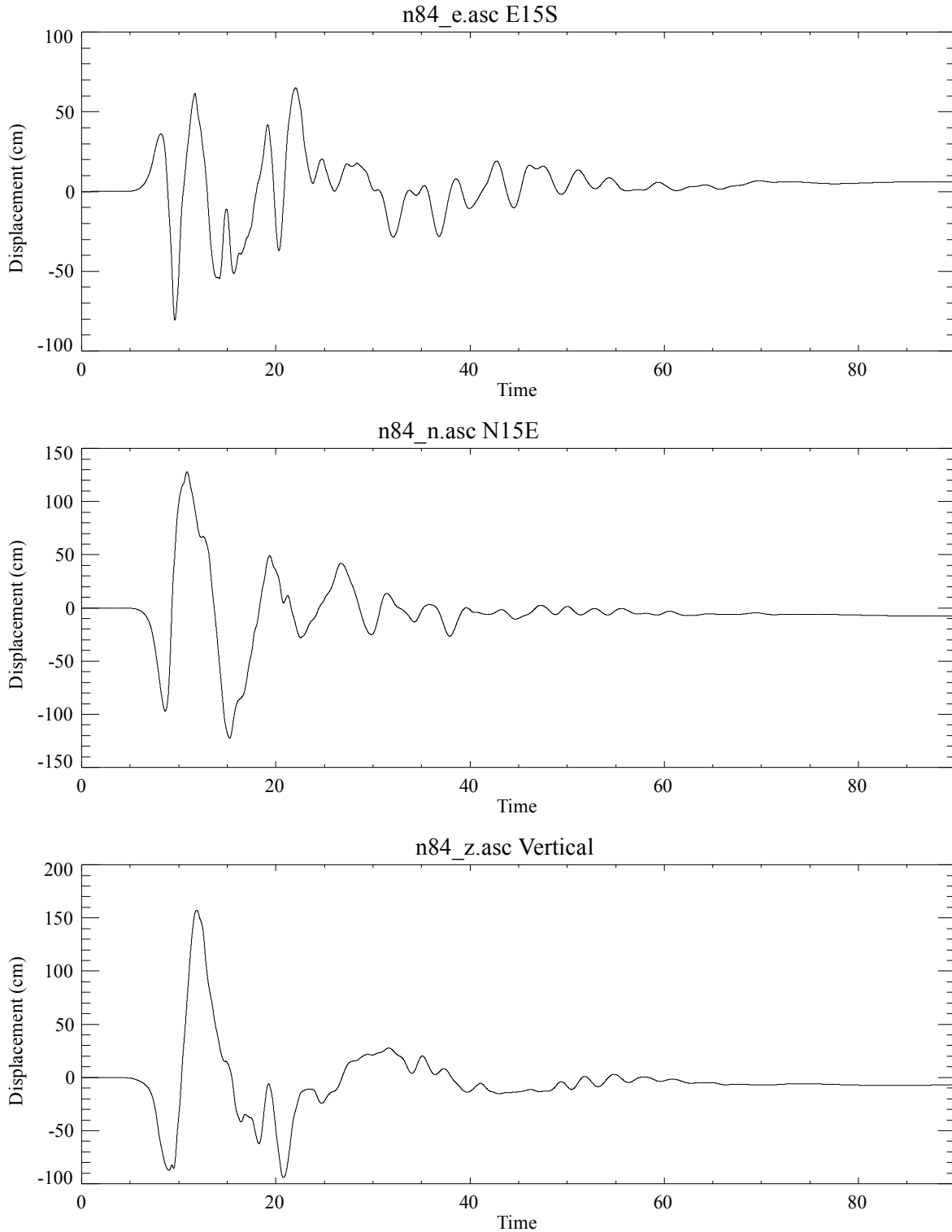


Figure 6-44: JLDW rock site 84 percentile displacement seismograms for dynamic analyses of Jackson Lake Dam. Components are labeled with time history filename and component orientation, with horizontal components orientated upstream and cross canyon (along the dam axis). These seismograms correspond to the best-fitting acceleration response spectra to the 84 percentile response spectra from 3300 ground motion simulations for a fault dip of 35°.

These synthesized mean and 84% ground motions are solely intended for use in dynamic analyses of the concrete portion of the dam, particularly the southern half of the concrete section. The northern end of the concrete section experiences amplified and prolonged ground motion responses associated with the close proximity of the very-low-velocity glacial scour to the northern end of the concrete section. There are likely to be significant soil-structure interactions at the northern end of the concrete section of the dam (Wolf and Song, 1996). One way to account for the foundation complications on ground motion inputs into the northern concrete section of the dam would be to convolve three-component JLD2 site responses with the mean and 84% ground motions in Figures 6-37 to 6-44.

A significant concern with the synthesized ground motions is that the high-frequency durations are probably too short. To address this concern a ground motion recording is also recommended exclusively for use in the dynamic analyses of the concrete portion of the dam that contains significant high frequency duration. The Llolleo station recordings of the 1985 **M** 8 Chilean subduction earthquake is one of the few such long-duration acceleration strong motion records available (Figure 6-45). It provides a long duration consistent with LVB responses and has been recommended for dynamic analyses in Seattle (SAC Steel Project, 1997). However, it lacks the significant peak velocity (Figure 6-46) and displacement (Figure 6-47) responses expected at the dam, and is intended primarily to tests the sensitivity of the concrete section of the dam to prolonged short-period shaking. The Llolleo record should not be used for dynamic analyses beyond the stage of initiation of cracking, particularly to estimate total displacements, since it clearly lacks the substantial velocities and displacements characteristic of ground motions at Jackson Lake Dam. Inadequate peak velocities and displacements are reflected in the relatively low Llolleo PSA responses for periods > 0.8 s (Figure 6-48). The orientation of the horizontal components was selected to assign the peak responses to the E15S component for dynamic analyses. The short period (< 0.4 s) acceleration responses on the E15S component exceed target mean and 84% PSA responses (Figure 6-48), but peak N15E responses are less than peak 84% PSA response.

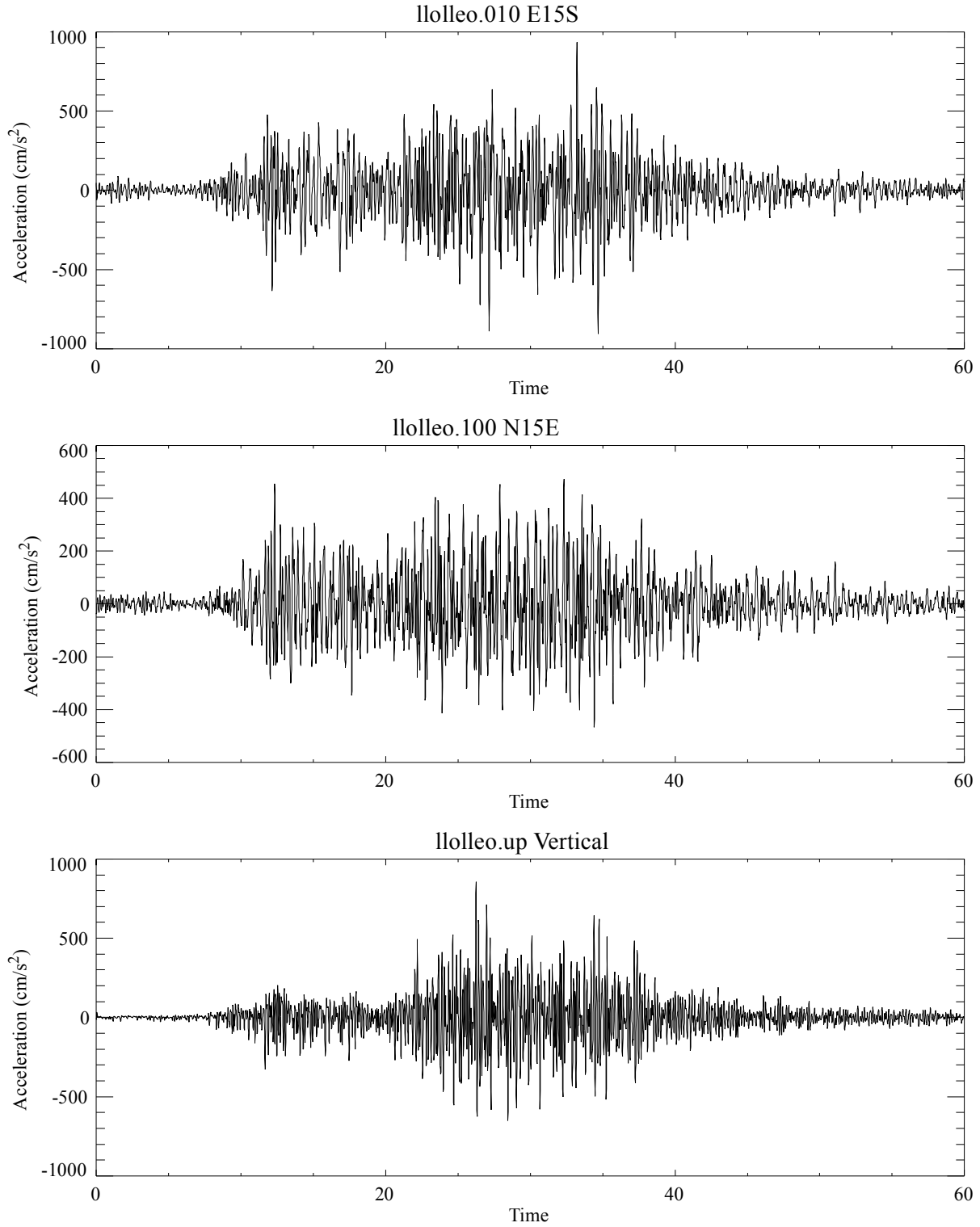


Figure 6-45: Lolloo, Chile, acceleration seismograms for dynamic analyses of the concrete section of Jackson Lake Dam. Components are labeled with time history filename and component orientation.

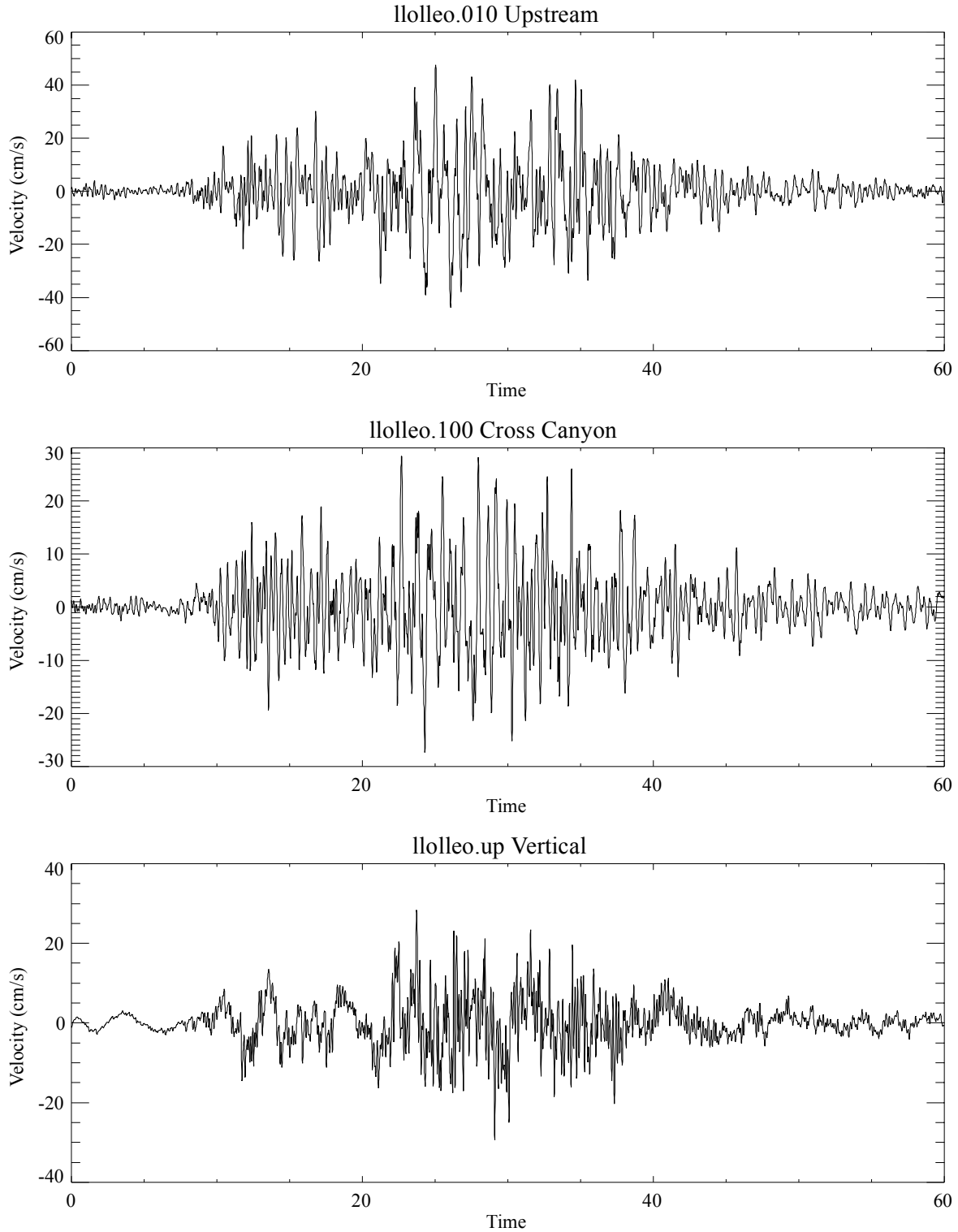


Figure 6-46: Lolloe, Chile, velocity seismograms for dynamic analyses of Jackson Lake Dam. Components are labeled with time history filename and component orientation, with horizontal components orientated upstream and cross canyon (along the dam axis).

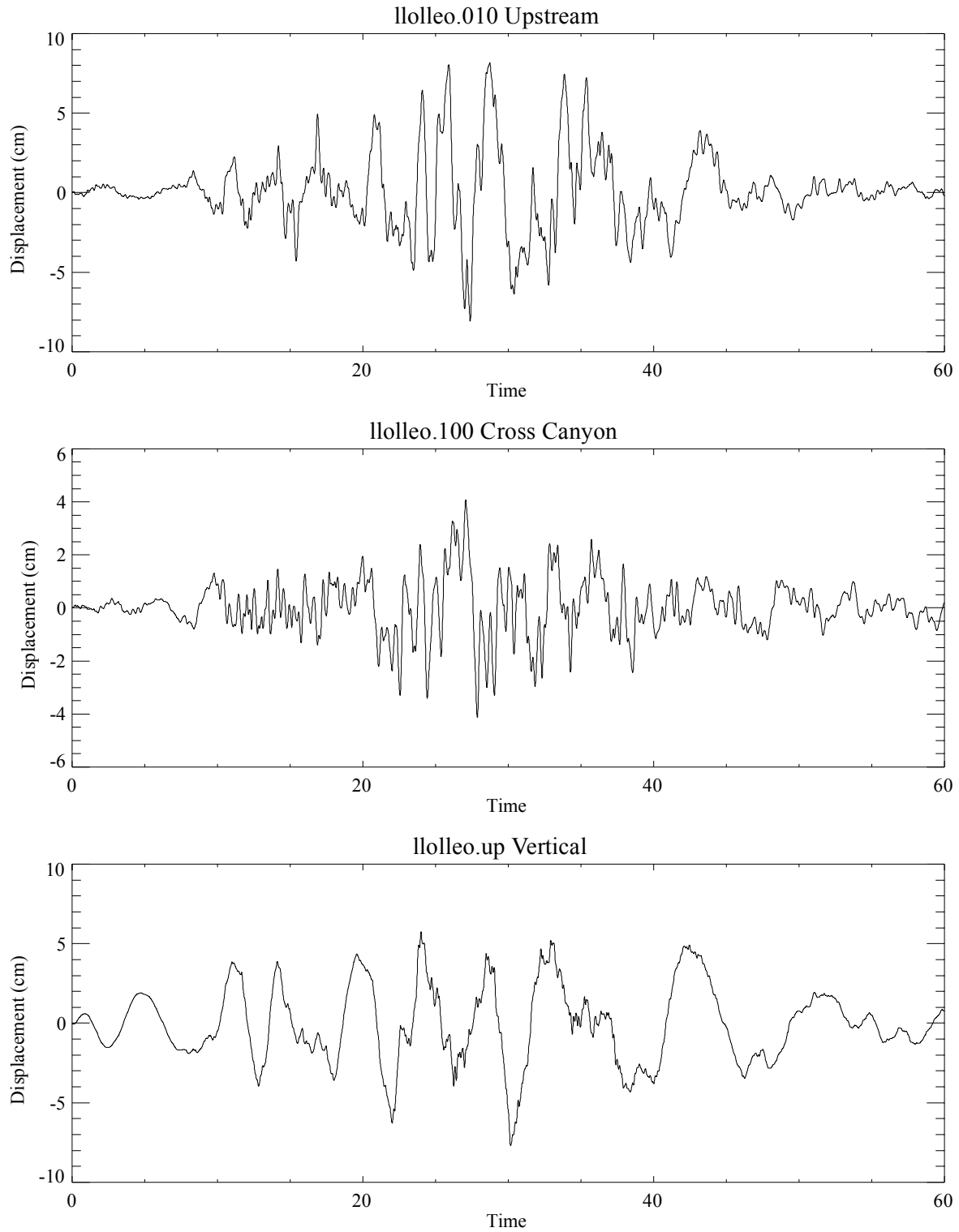


Figure 6-47: Llolleo, Chile, displacement seismograms for dynamic analyses of Jackson Lake Dam. Components are labeled with time history filename and component orientation, with horizontal components orientated upstream and cross canyon (along the dam axis).

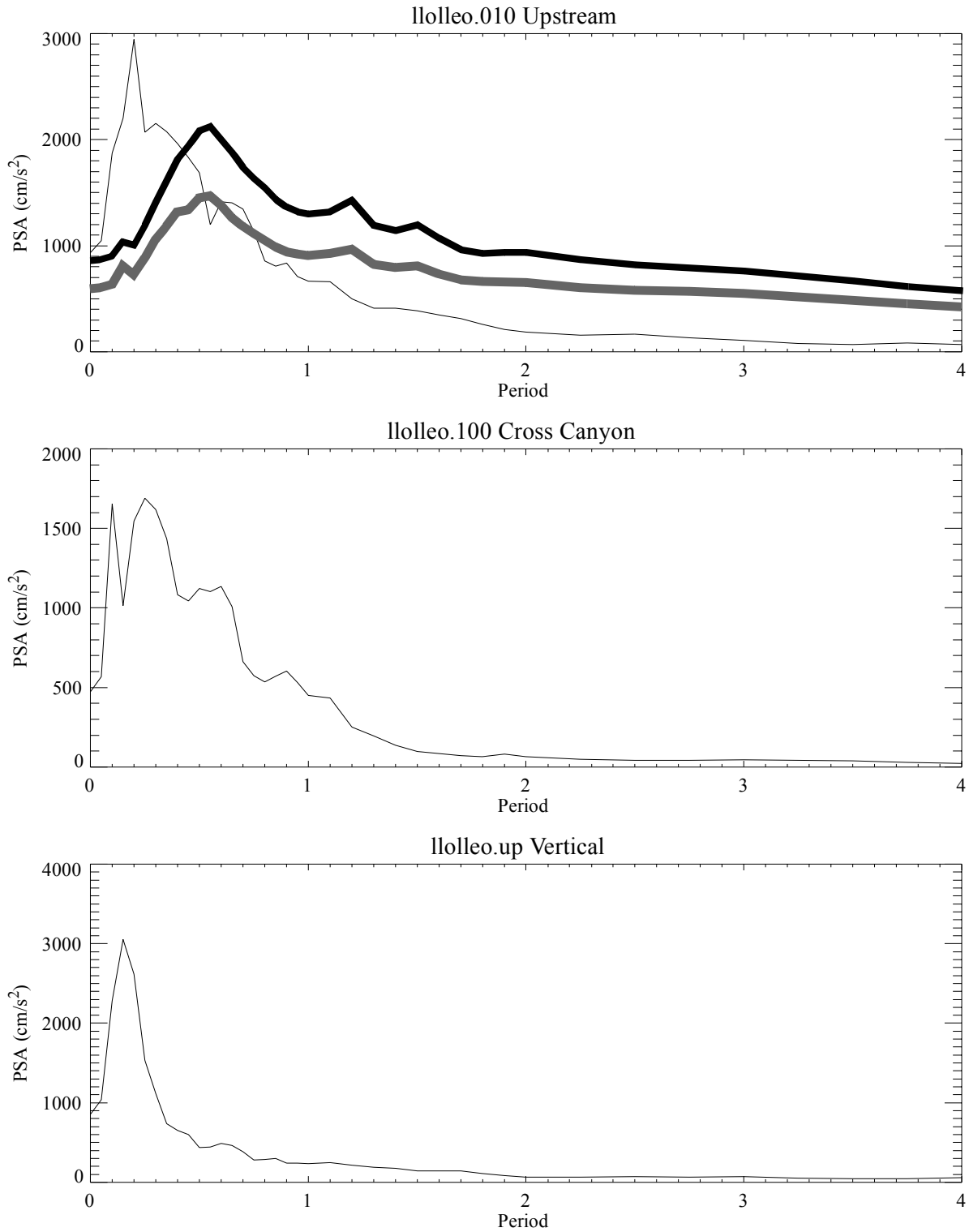


Figure 6-48: Response spectra corresponding to the Lloleo acceleration seismograms. Components are labeled with time history filename and component orientation. The synthetic 84% quantile and mean response spectra for the upstream component for a fault dip of 35° are plotted as the black and grey curves, respectively, for comparison at the top (Llolloe responses are the thin black curves).

6.6 Inputs for Nonlinear Ground Motion Calculations

As discussed in Section 6.1, the finite-difference code NOAH is used to approximate nonlinear soil responses. The site response investigations in Section 5 showed that low-velocity fluvial-lacustrine deposits beneath the embankment portion of the dam amplify ground motions and significantly increase durations, relative to the JLDW rock site (Figure 6-49). Synthetic modeling of the observed long duration ground motions near the embankment section in Section 5 showed that the durations are probably produced by glacial-scour-edge S-waves and horizontally-propagating interface waves, including Stonely waves that radiate energy to the surface from first-order velocity discontinuities and vertical velocity gradients located at depths $> \sim 25$ m. The glacial-scour-edge Rayleigh waves produce large amplitude, broadband Airy phases. Stonely waves are freely propagating interface waves with evanescent decay away from the interface into the media on either side; they are not body waves. The Stonely waves attenuate very slowly, even for Q's of 5, and may not be significantly influenced by soil nonlinearity. Stonely waves cannot be modeled with SHAKE or NOAH. Consequently, the prolonged soil durations associated with Stonely wave energy must be included in the input ground motion to 1D programs like SHAKE and NOAH. The glacial-scour-basin-edge S-waves propagate primarily below 25 m depth and produce strong high-frequency amplitudes for portions of the embankment dam located with 1 km of the southern margin of the glacial scour. Consequently, the most probable scenario is that ground motions impinging on the low-velocity shallow nonlinear soils will have durations comparable to those observed in the weak motion surface recordings presented in Section 5. Time-frequency plots calculated using 1.6 s time windows centered on each time point, illustrate significant differences in the amplitudes and durations between the JLDW rock site (Figures 6-49 and 6-50) and the JLD3 soil site (Figures 6-40 and 6-51). The durations of frequencies > 3 Hz is ~ 2.5 times longer for JLD3 than JLDW. The duration of 1 Hz responses at JLD3 is 3 times longer than at station JLDW. JLD3 spectral amplitudes that are about half of the peak 0.5-to-1 Hz spectral amplitude in the JLD3 seismogram persist for about 60 s.

Three scenarios were used to construct ground motions for use in nonlinear soil calculations to bracket the ranges of possible ground motion inputs into nonlinear soils (Table 6-5). In scenarios 1 and 3, halving the surface motion amplitudes removes the nominal free surface amplification.

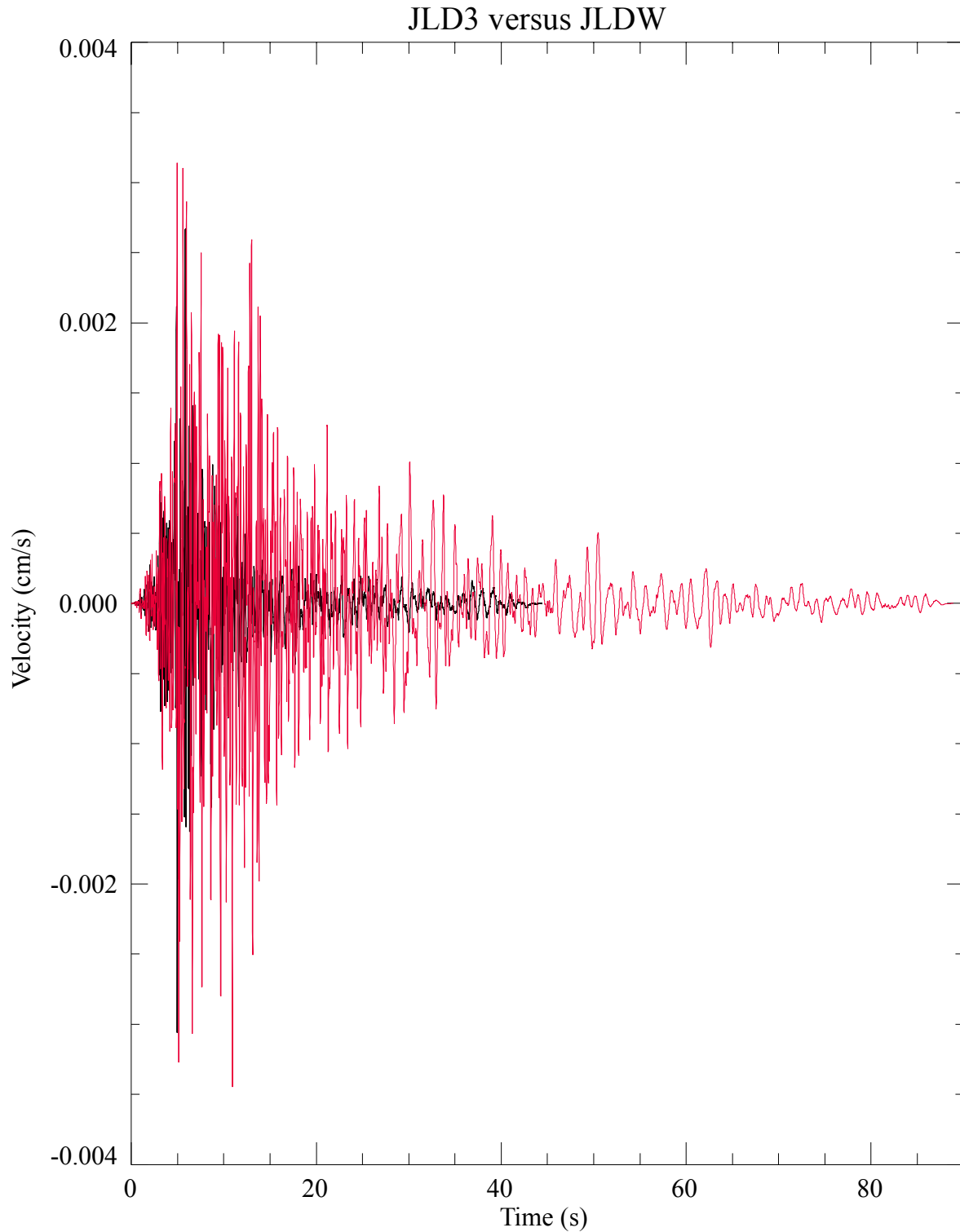


Figure 6-49: East horizontal component microearthquake velocity seismograms for JLDW and JLD3. JLDW is black and JLD3 is red.

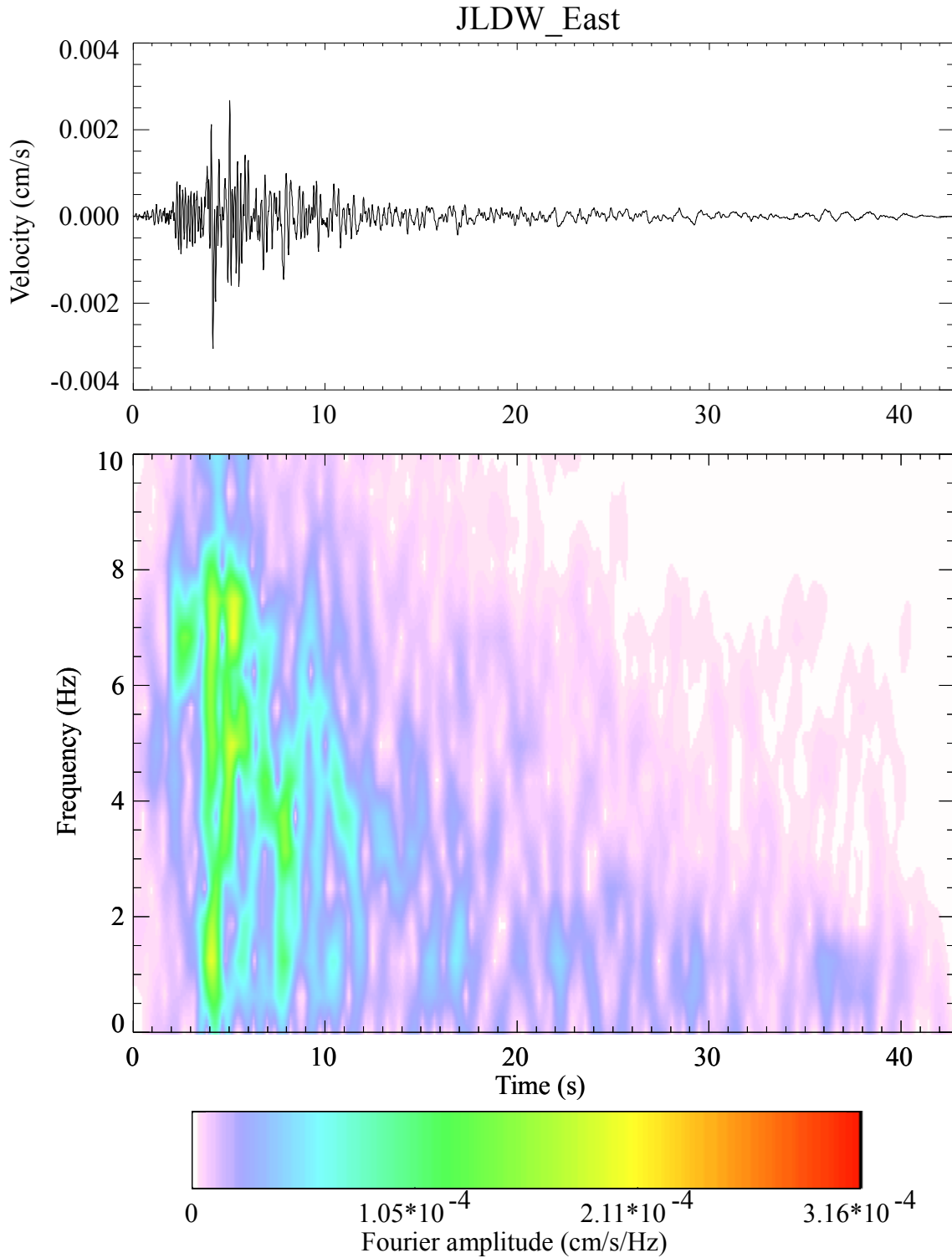


Figure 6-50: Time-frequency for the JLDW east-component seismogram from Figure 6-49. The amplitude scales are the same as in Figure 6-51 for the corresponding JLD3 seismogram.

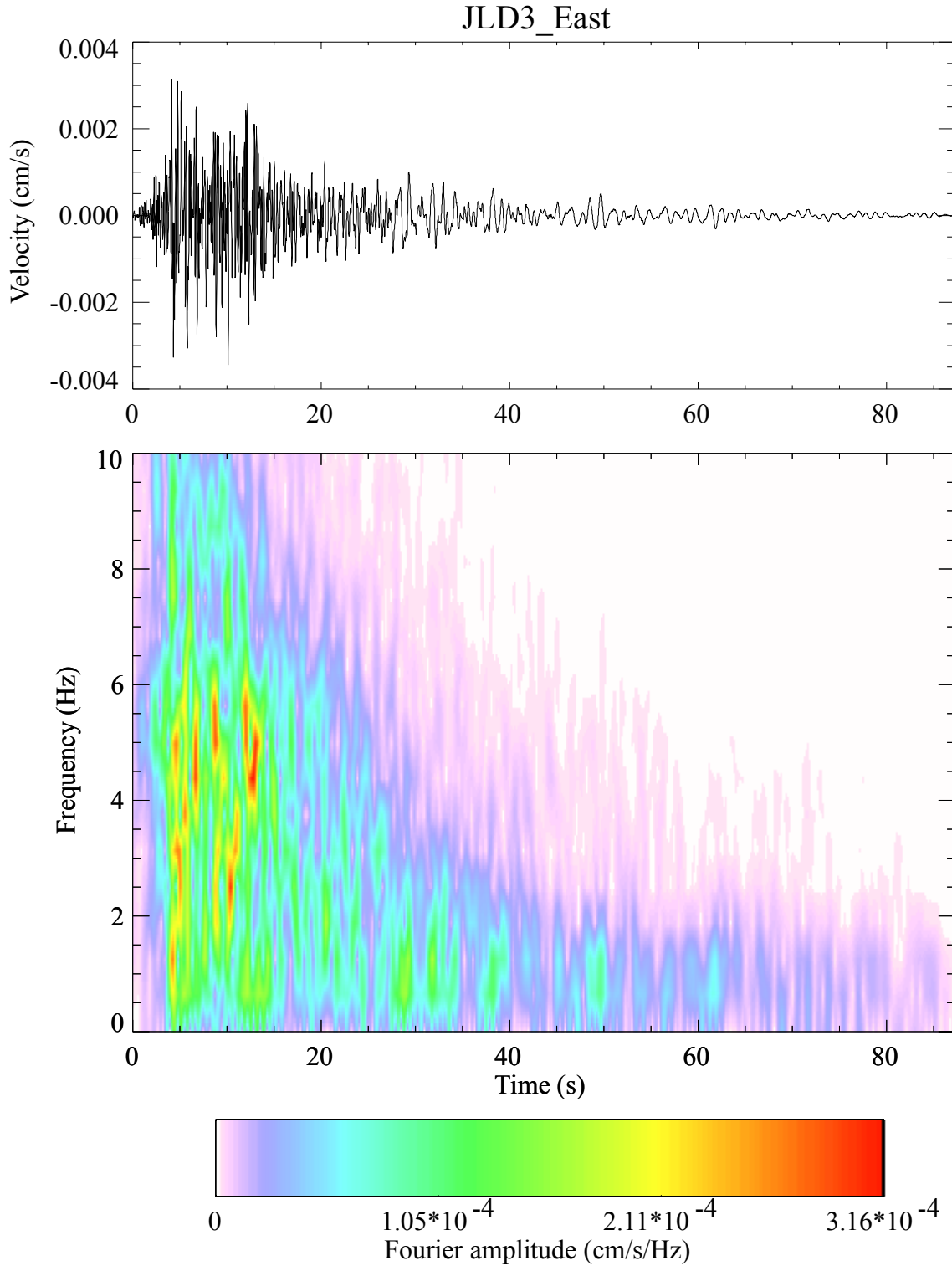


Figure 6-51: Time-frequency for the JLD3 east-component seismogram from Figure 6-49. The amplitude scales are the same as in Figure 6-50 for the corresponding JLDW seismogram, but the duration is about twice as long as in Figure 6-50.

Since the JLDW responses are at the free surface on the same type of material (glacial till) as the material at 140 m depth below the soil, halving the rock responses is reasonable. However, since the incident ground motions are predominantly composed of P-SV waves, and not SH waves, halving can overcorrect for the free-surface amplification, and always over corrects at long periods; halving is appropriate for high frequencies for input motions at 140 m depth. For

Table 6-5: Ground Motion Input Scenarios for Nonlinear Soil Calculations

Scenario number.	Characteristics.
1	Half amplitude, rock duration
2	2/3 * Half amplitude, soil duration
3	Half amplitude, soil duration

scenarios 2 and 3, the rock responses were convolved with JLD3 responses to obtain reasonable soil durations and scaled as 2/3 of half of the surface responses or half of the surface responses. Scaling by 2/3 in scenario 2 was done to compensate for the ~50% amplification of the input peak velocities at the surface by 1D SH propagation (obtained by running weak motion responses through NOAH with the soil compaction velocity profile). Scenario 3 provides a larger input scaling (only removing the free-surface amplification) that accounts for the failure of a 1D SH propagation approach to fully reproduce observed soil amplifications. The rock durations in scenario 1 are very likely to be too short, but combined with the soil durations in scenarios 2 and 3 provide a means to crudely bracket possible durations. Scenarios 2 and 3 are probably most representative of expected soil responses. To account for elastic boundary conditions at the bottom of the NOAH models, all the input motions were scaled by an additional 0.65 to reproduce the intended subsurface rock peak amplitudes immediately above 140 m depth.

Two velocity models were used to approximate the conditions in the compacted soil beneath the embankment (Figure 6-52) and the soil mix walls (Figure 6-53). Obviously, the simplest realistic configuration would require a 2D calculation method to account for the mass and shape of the dam and for the lateral variations in the upstream-downstream direction. Laterally from upstream to downstream, conditions vary from untreated soils upstream of the dam, with near-surface S-wave velocities of ~80-100 m/s (Sirles, 1988), a ~16 m-wide upstream soil mix wall, with S-wave

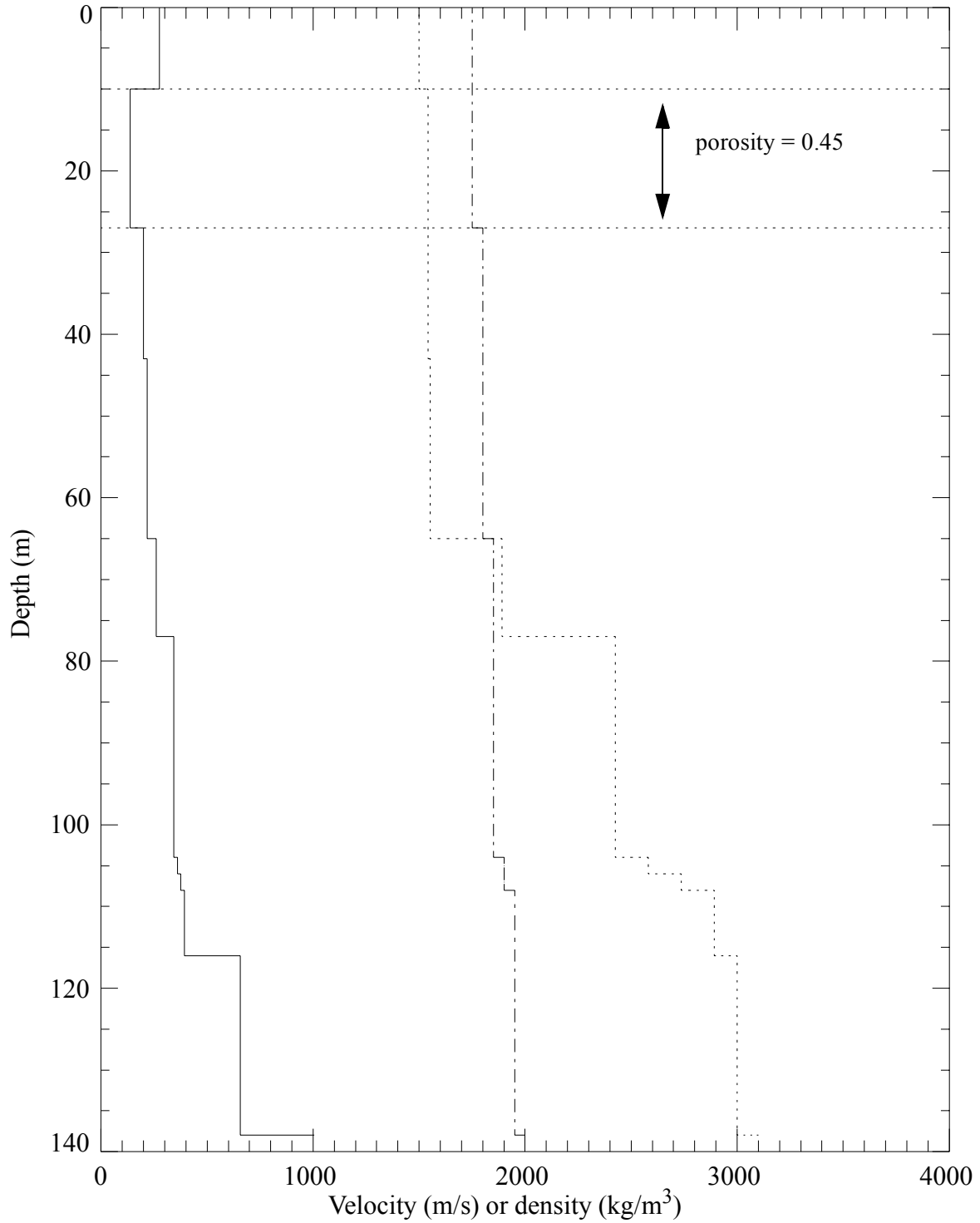


Figure 6-52: NOAH velocity-density depth model for the compaction region. The model extends from the free surface to the high-velocity till at 138 m depth. S-wave velocity is the solid curve, P-wave velocity is the dotted curve, and density is the dash-dot curve. Dotted horizontal lines show the upper and lower limits of the low-velocity region with nonzero porosity.

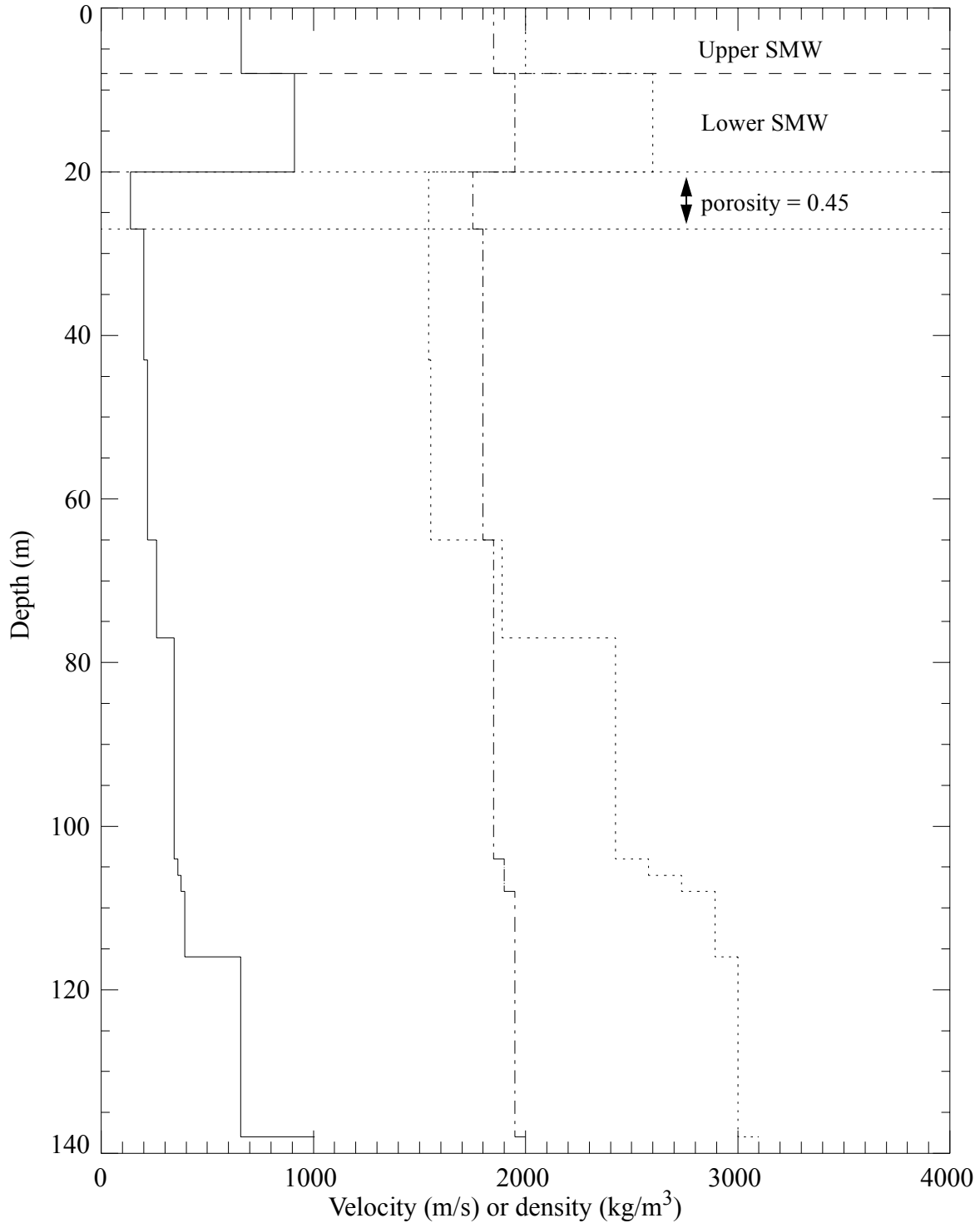


Figure 6-53: NOAH velocity-density depth model for the soil mix wall region. The model extends from the free surface to the high-velocity till at 138 m depth. S-wave velocity is the solid curve, P-wave velocity is the dotted curve, and density is the dash-dot curve. Dotted horizontal lines show the upper and lower limits of the low-velocity region with nonzero porosity. The upper horizontal dotted line shows the bottom of the soil mix wall (SMW) and the horizontal dashed line shows the bottom of the upper, low-velocity portion of the SMW.

velocities of ~660 m/s to a depth of ~8 m and S-wave velocities of ~910 m/s to a depth of ~20 m (Wright, 1990), a ~30 m-wide compacted soil zone beneath the central embankment section with S-wave velocities of ~275 m/s to a depth of ~10 m and S-wave velocities of ~138 m/s to a depth of ~27 m (Dave Gillette, personal communication), a 16 m-wide downstream soil mix wall with the same properties as the upstream soil-mix wall, and untreated downstream materials with near-surface S-wave velocities of ~80-100 m/s (Sirles, 1988). Soil-structure interactions between the soil mix walls and adjoining compacted and untreated soils are likely to complicate responses in all materials relative to the 1D approximations used in SHAKE and NOAH. For instance, ground motions at station JLD4 located on a soil mix wall was deamplified for frequencies > 1 Hz relative to motions at station JLD3, located ~28 m downstream of JLD4 on untreated soil (Section 5). Consequently, peak motions near the center of the soil mix walls may be lower than calculated in the 1D approximation, but compacted soil responses are likely to be underestimated (the soil mix walls will likely focus energy into the compacted soils beneath the dam, particularly for frequencies > 1 Hz). The water table is placed at a depth of 2 m, but the soil mix walls and compacted soil are assumed to be always dry (zero porosity). Only the low-velocity layer below the soil mix walls and compacted soil are assigned a nonzero porosity of 0.45 (Figures 6-52 and 6-53).

The synthetic rock reference site ground motions and the recording of the 1978 **M** 7.4 Tabas, Iran, earthquake were combined with the empirical site response information from Section 5 to develop ground motion time histories for input into nonlinear soil responses calculations using NOAH and SHAKE. Only NOAH effective stress results, which account for pore pressure (Bonilla et al., 1998; Bonilla, 2000), are presented in this report. The approximated impulse response function obtained by deconvolving the station JLDW east horizontal component from the soil station JLD3 described in Section 5 was convolved with the three rock site ground motions, and rescaled to produce scenarios 2 and 3 inputs for nonlinear calculations at 140 m depth (Figures 6-54 to 6-56 show scenario 3 seismograms). NOAH results were also produced using the three rock motions divided by two as inputs at 140 m depth. The nonlinear rock motion inputs are solely used to provide a lower bound on soil responses. The rock motions lack the soil amplification and duration responses characteristic of the soil responses at JLD3 and the 1D SH approximations used in NOAH and SHAKE are not sufficient to convert rock durations to realistic soil durations.

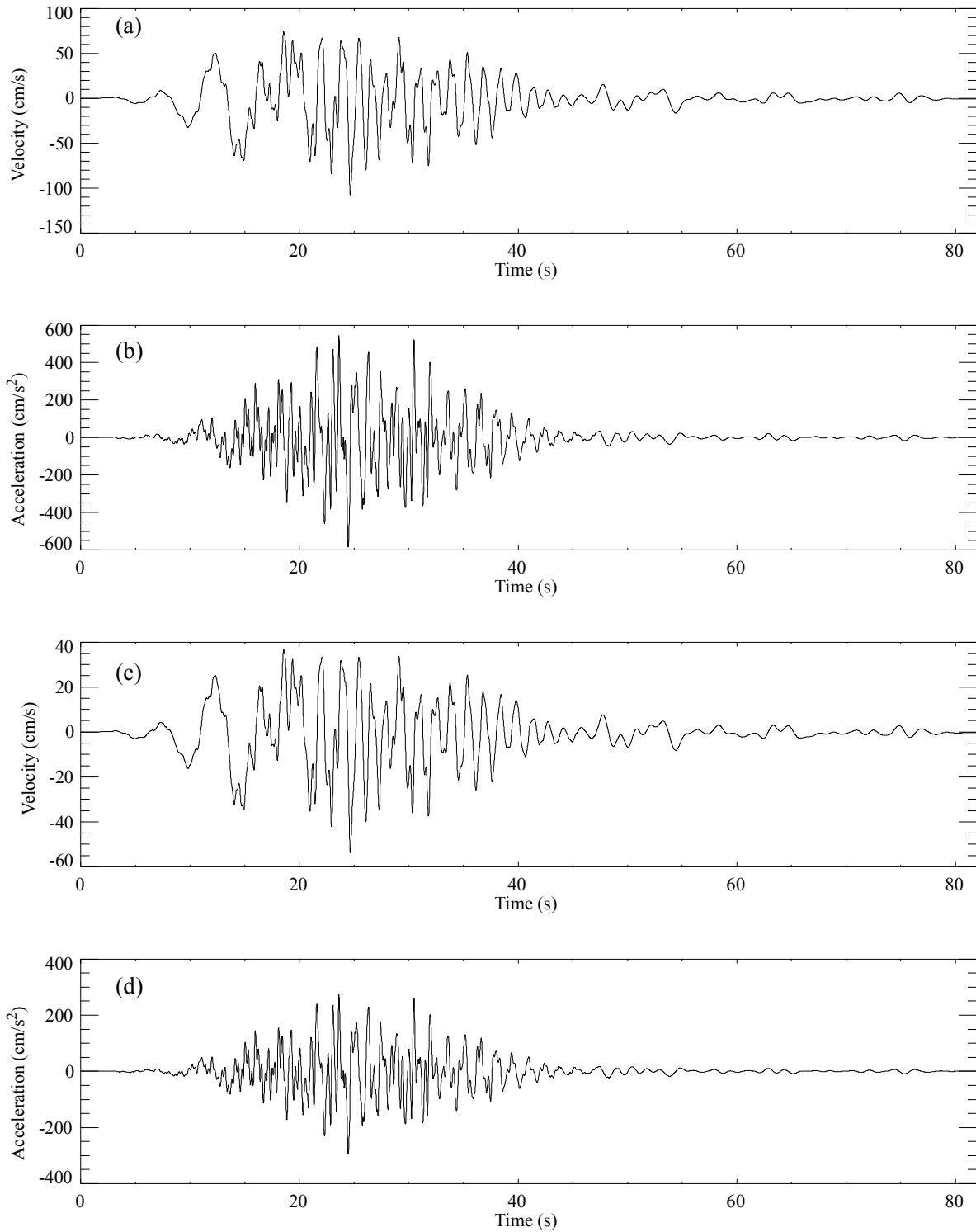


Figure 6-54: Mean JLDW E15S rock motion velocity (a) and acceleration (b) convolved with the JLD3 soil response transfer function. The resulting motion was rescaled by half for input into NOAH (c-d).

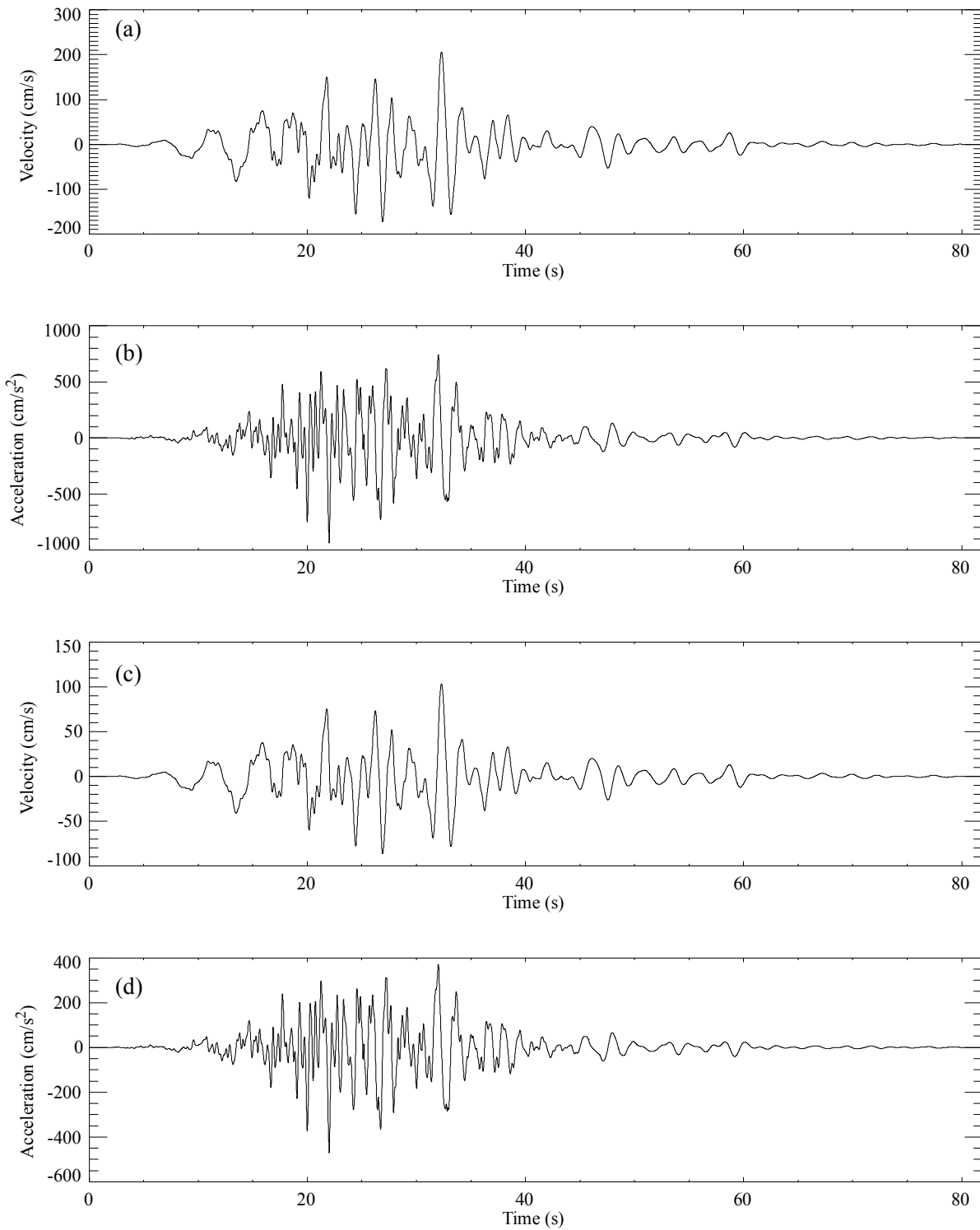


Figure 6-55: 84% JLDW E15S rock motion velocity (a) and acceleration (b) convolved with the JLD3 soil response transfer function. The resulting motion was rescaled by half for input into NOAH (c-d).

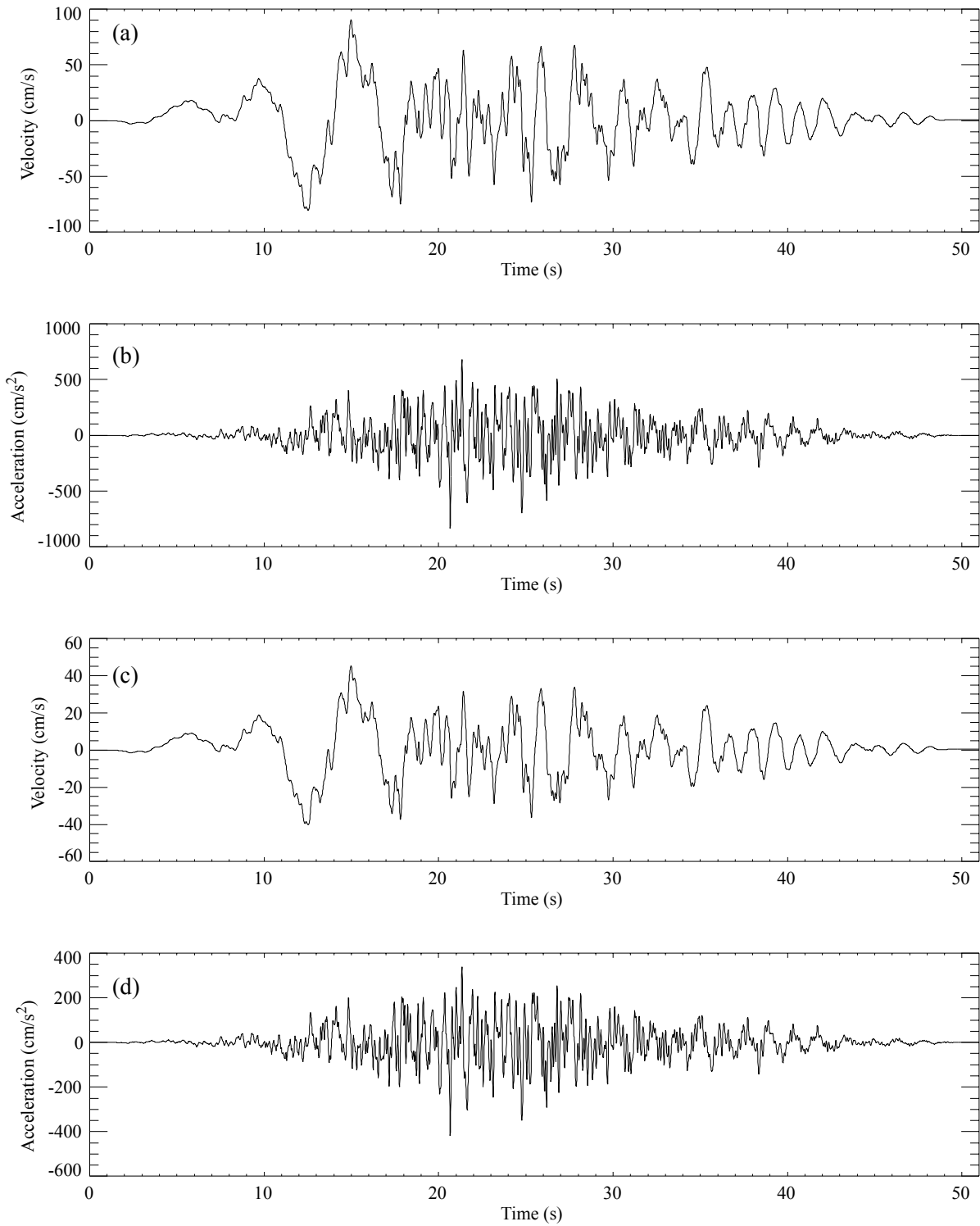


Figure 6-56: Tabas E15S rock motion velocity (a) and acceleration (b) convolved with the JLD3 soil response transfer function. The resulting motion was rescaled by half for input into NOAH (c-d).

Only summary results are presented in this section. The NOAH inputs and outputs for scenarios 1-3 are presented in Appendix E and UCSB nonlinear soil analyses are presented in Appendix F.

6.6.1 Nonlinear Compacted Soil Zone Results. Nonlinear NOAH JLD3 site-response input results for the compacted soil zone velocity model (Figure 5-52) are summarized in Figure 6-57. The minimum peak acceleration in the lower portion of the compaction layer is > 0.4 g (Figure 6-57). Arias Intensities and durations in portions of the compaction layer are always larger than corresponding rock motions (Tables 6-2 to 6-4) and approach values associated with $M \sim 8$ earthquakes based on the relations of Kayen and Mitchell (1997) and Bommer and Martinez-Pereira (1999). Since peak accelerations are often dominated by frequencies > 10 Hz, response spectra for periods of 0.2 s, 0.5 s, 1 s, and 2 s are presented in Figure 6-58 to provide relevant acceleration loads for the dam. For periods of 1 s and longer, the PSA exceed 0.4 g for all JLD3 response inputs. Comparison of the nonlinear NOAH rock site-response input results for the compacted soil zone velocity model in Figure 6-59 with the JLD3 response input results in Figure 6-57 show the influence of input ground motion duration on calculated soil responses. For rock motion inputs, Arias Intensities and durations are generally a two-thirds to half of the JLD3 response inputs. Minimum peak accelerations are only slightly smaller in the compaction layer, but maximum peak shear strains are strongly reduced using rock input motion durations (Figure 6-59). Duration also strongly influences PSA responses. Figure 6-60 shows that the shorter rock input durations produced reduced PSA responses. The rock input results likely underestimate soil responses because they lack the long soil durations that are result of horizontally-propagating trapped waves propagating at various depths within the ~ 140 m deep low-velocity glacial scour. Consequently, the JLD3 response input results (Figures 6-57 and 6-58) are more likely to represent expected responses at the dam.

6.6.2 Nonlinear Soil Mix Wall Results. Nonlinear NOAH JLD3 site-response input results for the soil mix wall velocity model (Figure 5-53) are summarized in Figure 6-61. Minimum Arias durations are somewhat longer than rock motions, but minimum Arias Intensities are larger than for rock motions. Minimum peak accelerations exceed 0.2 g. The PSA response in Figure 6-62 provide more robust acceleration load estimates than peak accelerations, which are dominated by > 10 Hz responses. The nonlinear soil responses decrease PSA response for 0.2 s

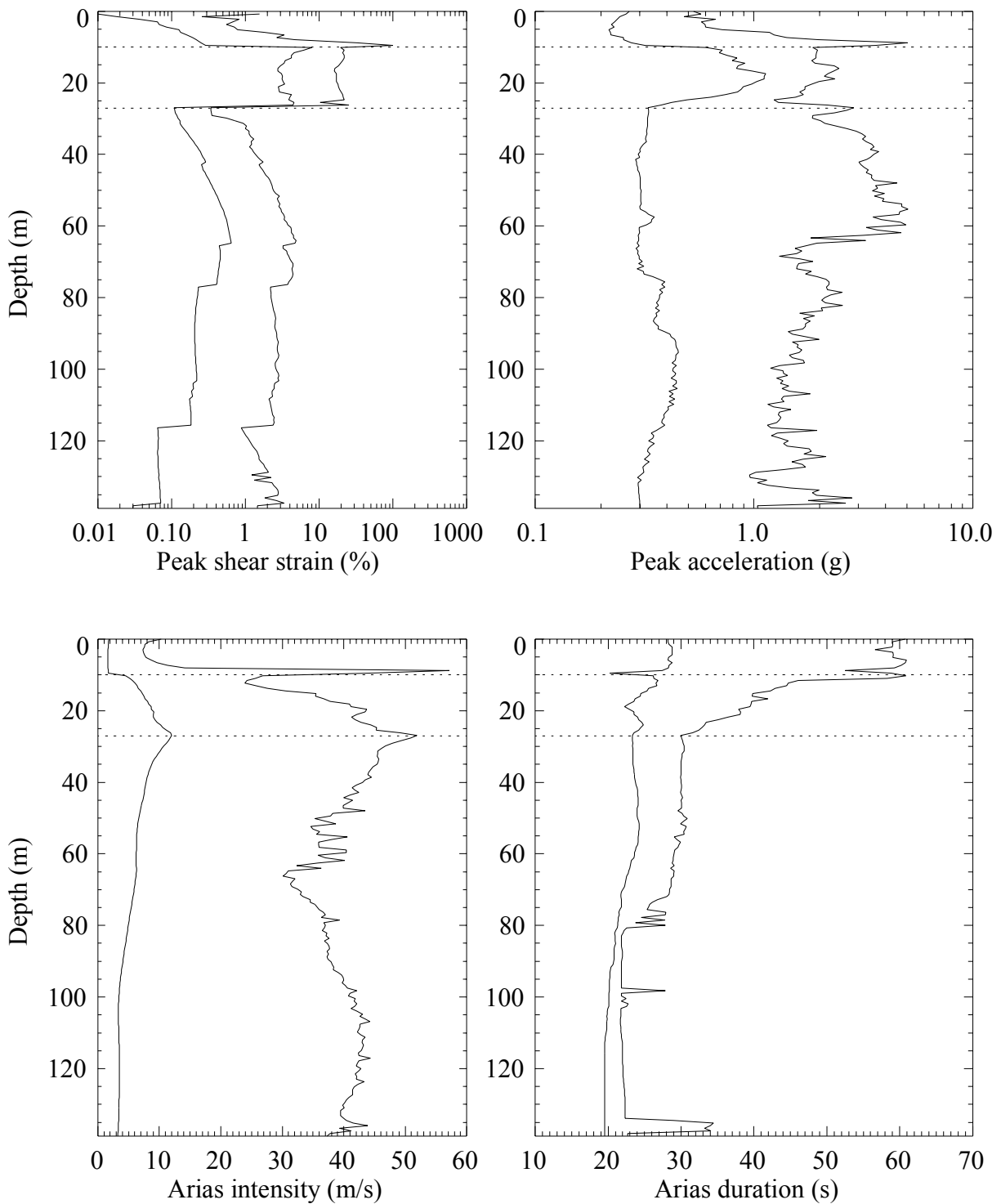


Figure 6-57: Time-domain compacted soil responses for JLD3 response input motions. In each figure the solid lines indicate minimum and maximum responses at each depth from the six input ground motions. The horizontal dotted lines show the depth range of the low-velocity layer with nonzero porosity. The compaction zone is the region above the top dotted line.

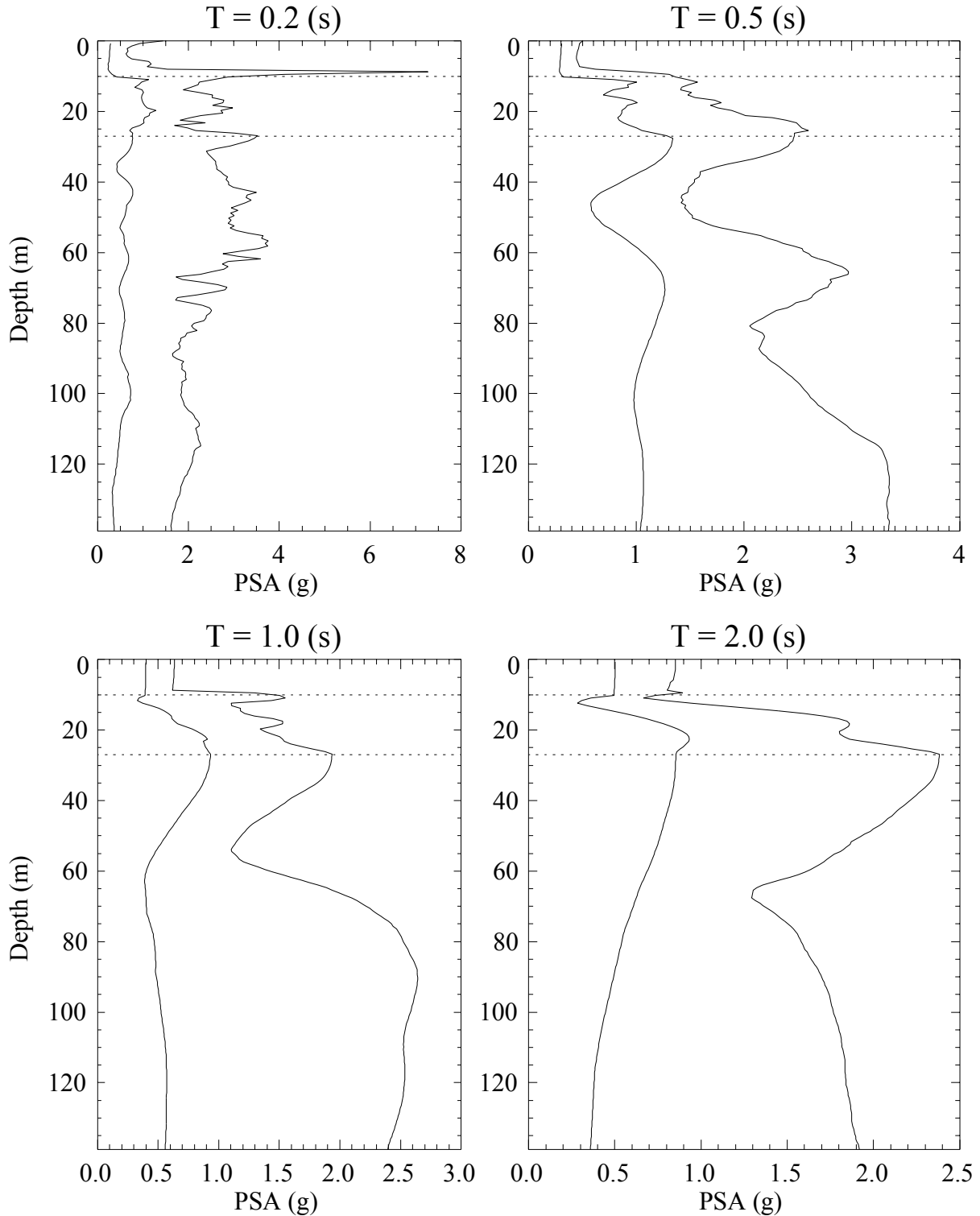


Figure 6-58: Compacted soil acceleration response spectra for JLD3 response input motions. Title of each figure is the period and the solid lines indicate minimum and maximum responses at each depth from the six input ground motions. The horizontal dotted lines show the depth range of the low-velocity layer with nonzero porosity. The compaction zone is the region above the top dotted line.

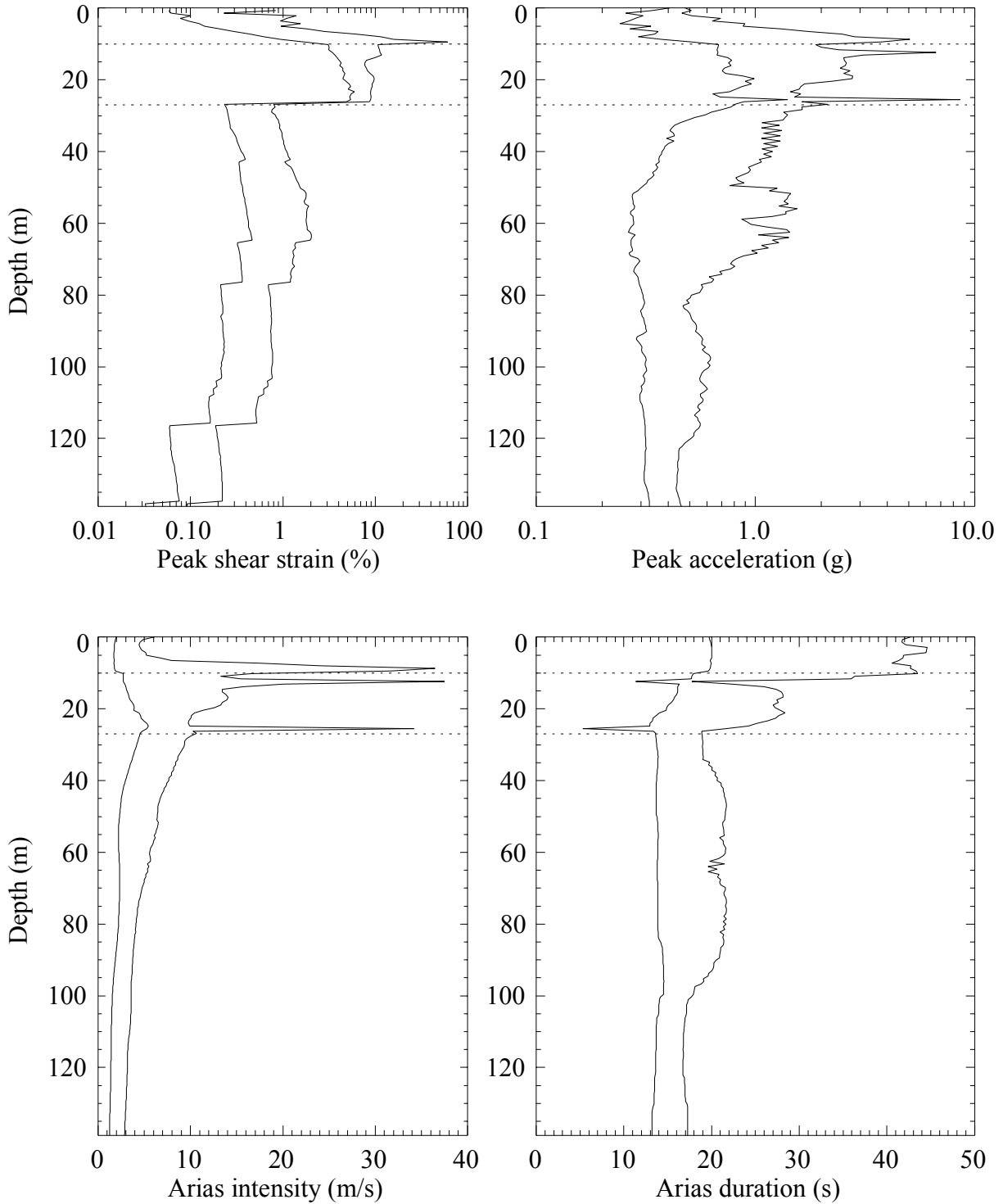


Figure 6-59: Time-domain compacted soil responses for rock response input motions. In each figure the solid lines indicate minimum and maximum responses at each depth from the six input ground motions. The horizontal dotted lines show the depth range of the low-velocity layer with nonzero porosity. The compaction zone is the region above the top dotted line.

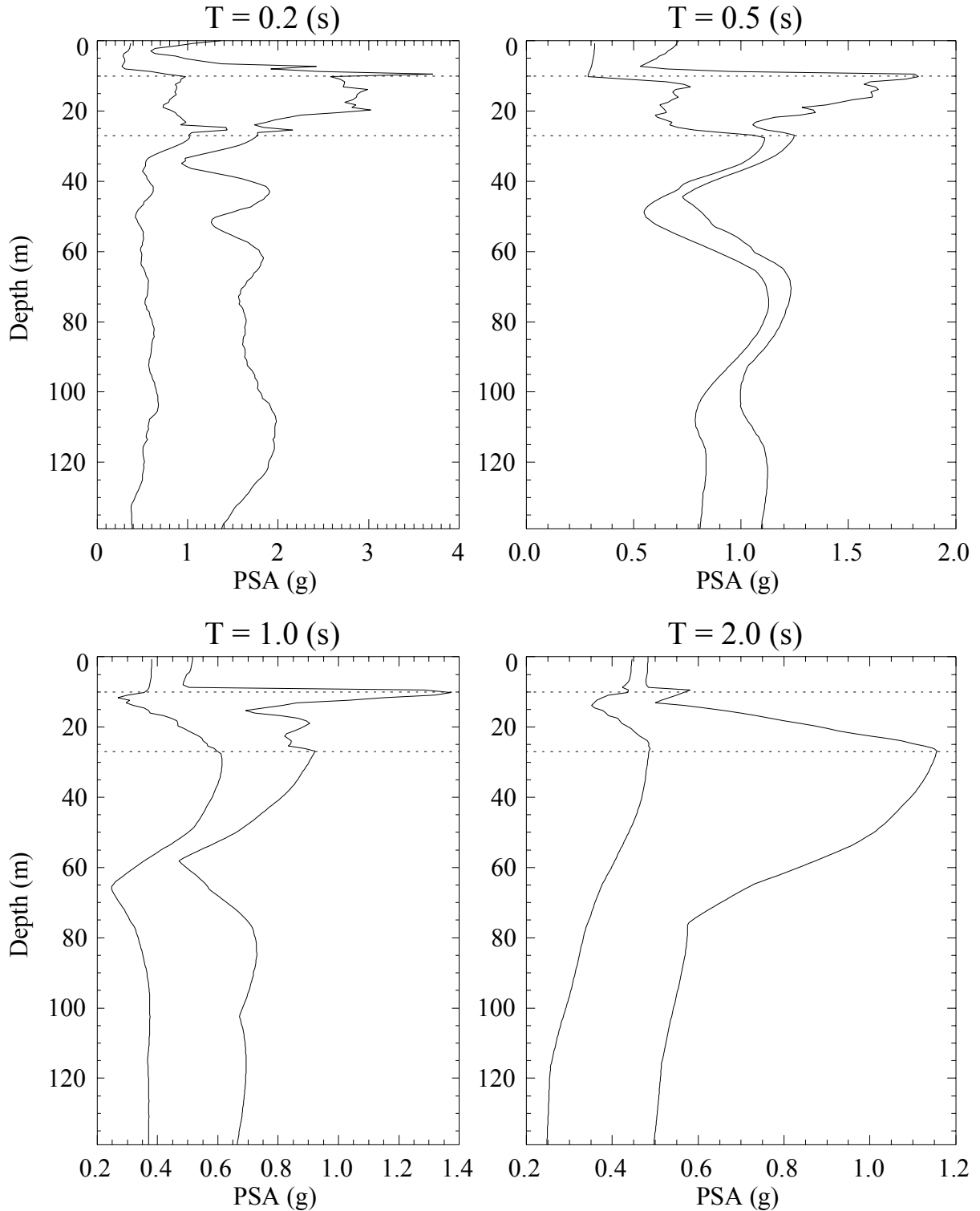


Figure 6-60: Compacted soil acceleration response spectra for rock response input motions. Title of each figure is the period and the solid lines indicate minimum and maximum responses at each depth from the six input ground motions. The horizontal dotted lines show the depth range of the low-velocity layer with nonzero porosity. The compaction zone is the region above the top dotted line.

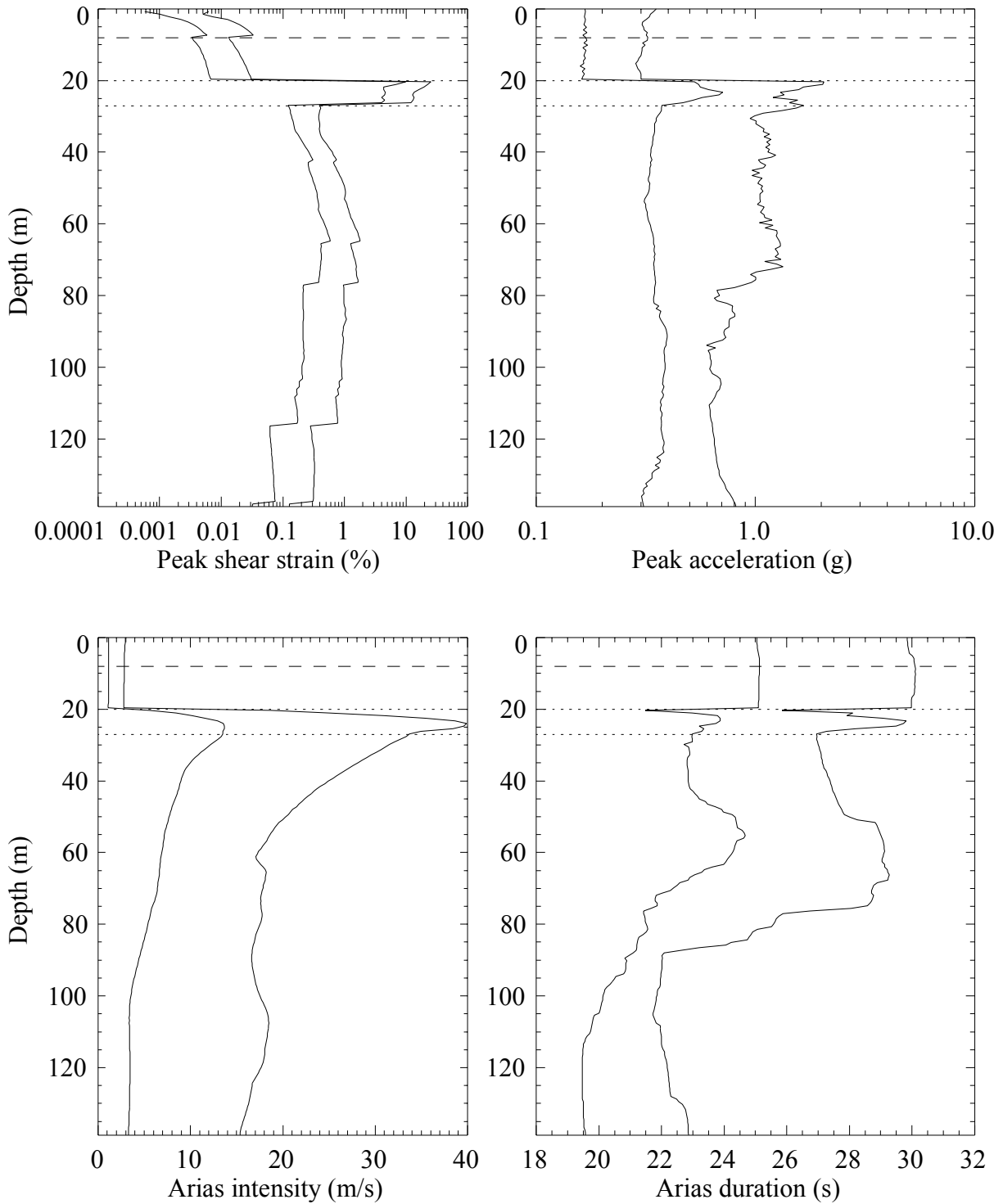


Figure 6-61: Time-domain soil mix wall responses for JLD3 response input motions. In each figure the solid lines indicate minimum and maximum responses at each depth from the six input ground motions. The horizontal dotted lines show the depth range of the low-velocity layer with nonzero porosity. The high-velocity SMW layer is located between the horizontal dashed line and the top dotted line. The lower-velocity SMW layer is located above the horizontal dashed line.

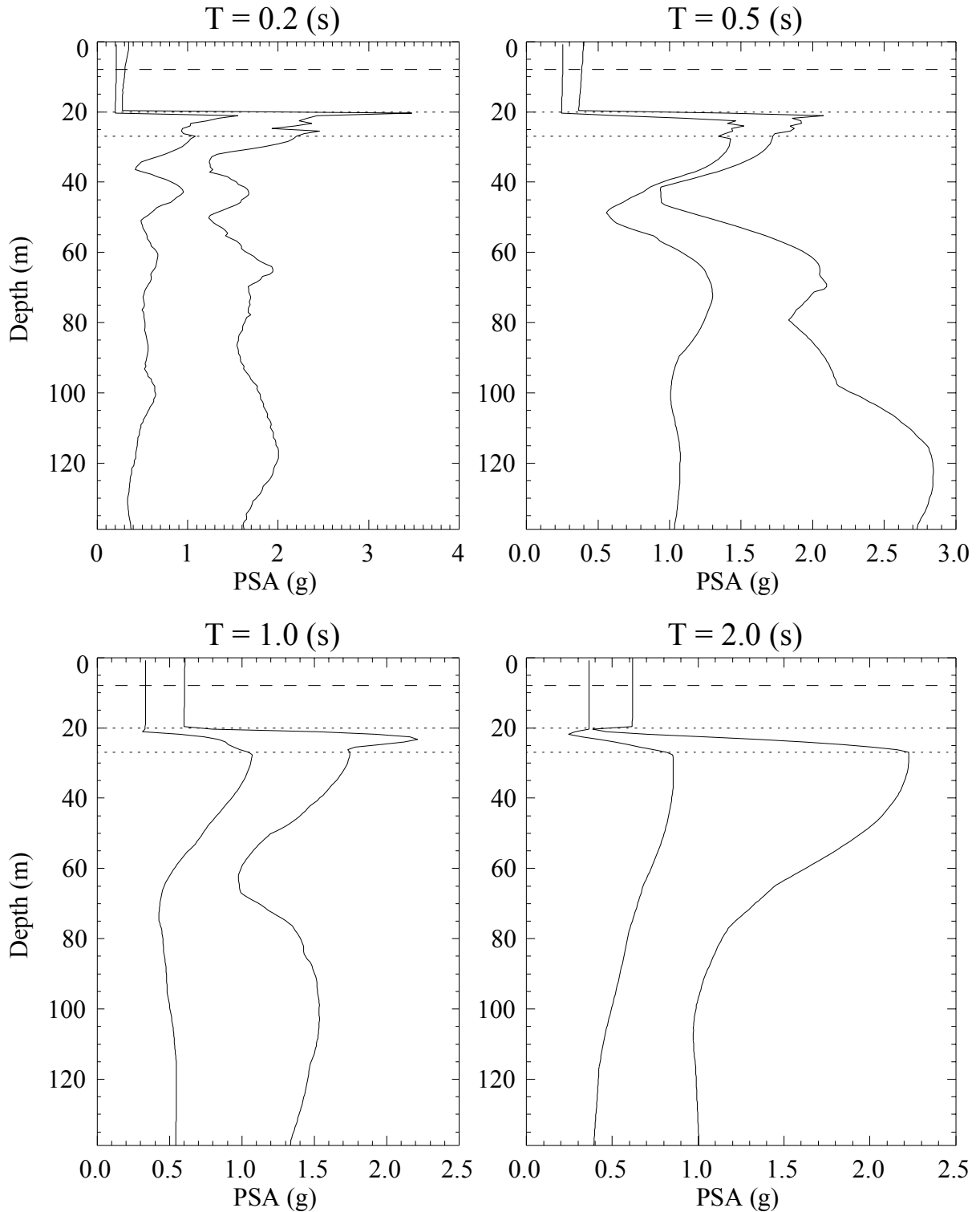


Figure 6-62: SMW soil acceleration response spectra for JLD3 response input motions. Title of each figure is the period. The solid lines indicate minimum and maximum responses at each depth from the six input ground motions. Horizontal dotted lines show the depth range of the low-velocity layer with nonzero porosity. The high-velocity SMW layer is located between the horizontal dashed line and the top dotted line. The lower-velocity SMW layer is located above the horizontal dashed line.

period. However, for periods of 0.5 s or larger, minimum PSA responses in the SMW are > 0.3 g (Figure 6-62). Comparison of the JLD3 response nonlinear results with nonlinear responses with rock input motions (Figure 6-63) shows a different dependence of peak motions and duration on input motion duration compared to Section 6.6.1. Peak accelerations and Arias Intensities are only slightly smaller for shorter duration rock input motions (Figure 6-63) than for long duration soil motions (Figure 6-61), but rock motion Arias durations are substantially smaller. PSA responses are only slightly lower for rock input motions (Figure 6-64), showing a weak influence of duration on SMW peak acceleration responses over a wide range of periods. The rock input results likely underestimate soil responses because they lack the long soil durations that are result of horizontally-propagating trapped waves propagating at various depths by significant velocity discontinuities and vertical velocity gradients within the ~140 m deep low-velocity glacial scour. Consequently, the JLD3 response input results (Figures 6-61 and 6-62) are more likely to represent expected SMW responses at the dam.

6.6.3 Discussion of Nonlinear Results. While nine different ground motion load scenarios were considered used in the nonlinear ground motion calculations, an important fact to consider is that both SHAKE and NOAH simplify seismic motions to vertically-propagating SH waves. At Jackson Lake Dam the seismic phases that produce the largest peak accelerations and velocities are likely to be SV waves in a coupled P-SV wavefield. Thus, neither SHAKE nor NOAH represent the physical quantities that will produce the strong ground motions at the dam. Consequently, the nonlinear ground motion calculations that use rock input motions are only provided to indicate lower bounds on soil motion responses. The nonlinear input motions produced using the JLD3 responses provide more realistic soil response scenarios than the rock input motions. A 2D (plane-wave) P-SV nonlinear calculation is necessary to determine if SHAKE or NOAH adequately represent nonlinear ground motion responses likely to occur at the dam. NOAH only predicts large-amplitude cusped, one-sided accelerograms for certain combinations of soil properties. It is not clear how well NOAH (or any other nonlinear approach) will predict nonlinear soil behavior at the dam, because estimates of important nonlinear soil parameters were not available from the dam site and must be inferred. A common assumption is that peak accelerations will generally decrease with depth in soils. Yoshida et al. (2002) showed that peak accelerations at the Kobe Port Island (a site that experienced liquefaction during the

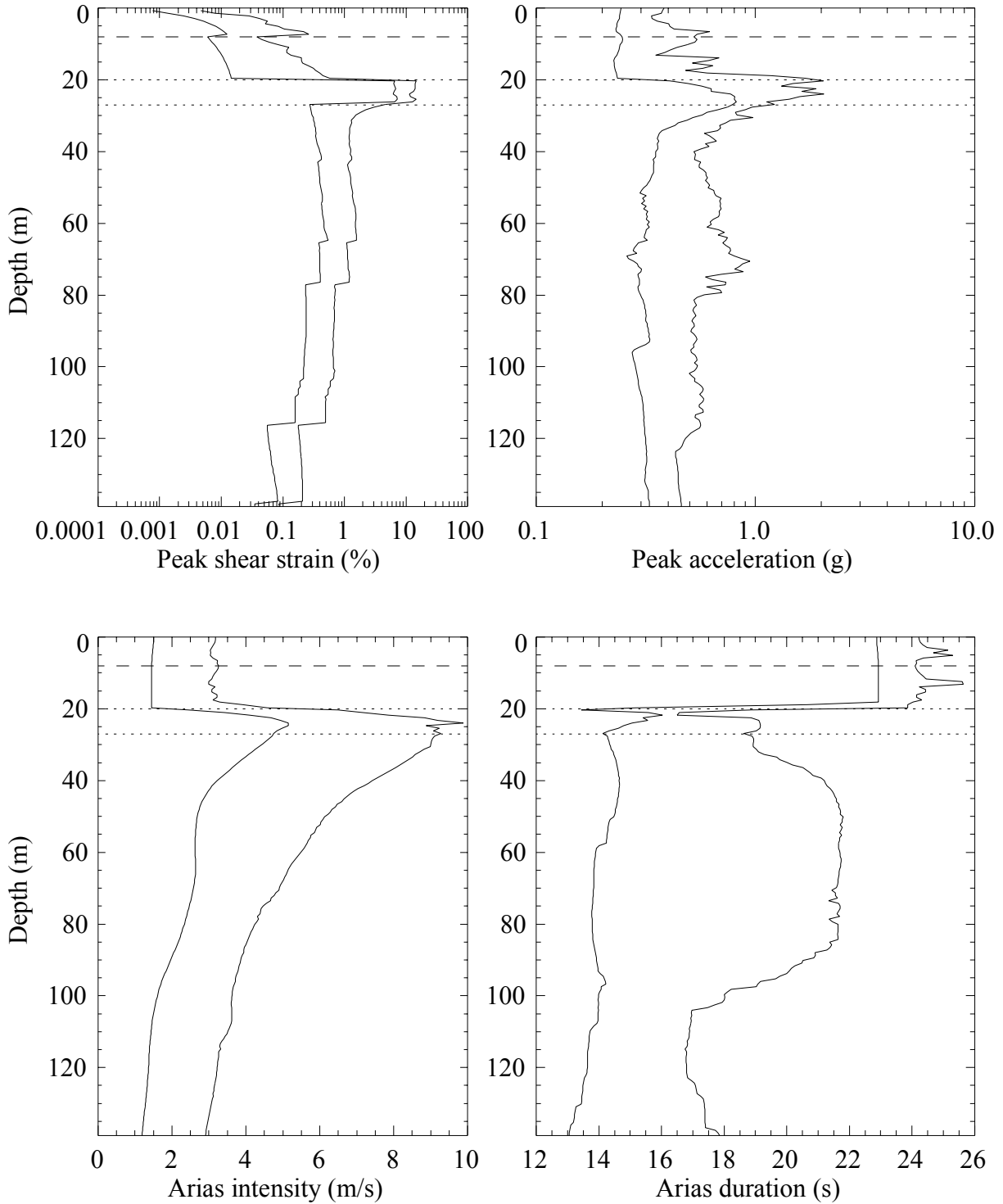


Figure 6-63: Time-domain soil mix wall responses for rock response input motions. In each figure the solid lines indicate minimum and maximum responses at each depth from the six input ground motions. The horizontal dotted lines show the depth range of the low-velocity layer with nonzero porosity. The high-velocity SMW layer is located between the horizontal dashed line and the top dotted line. The lower-velocity SMW layer is located above the horizontal dashed line.

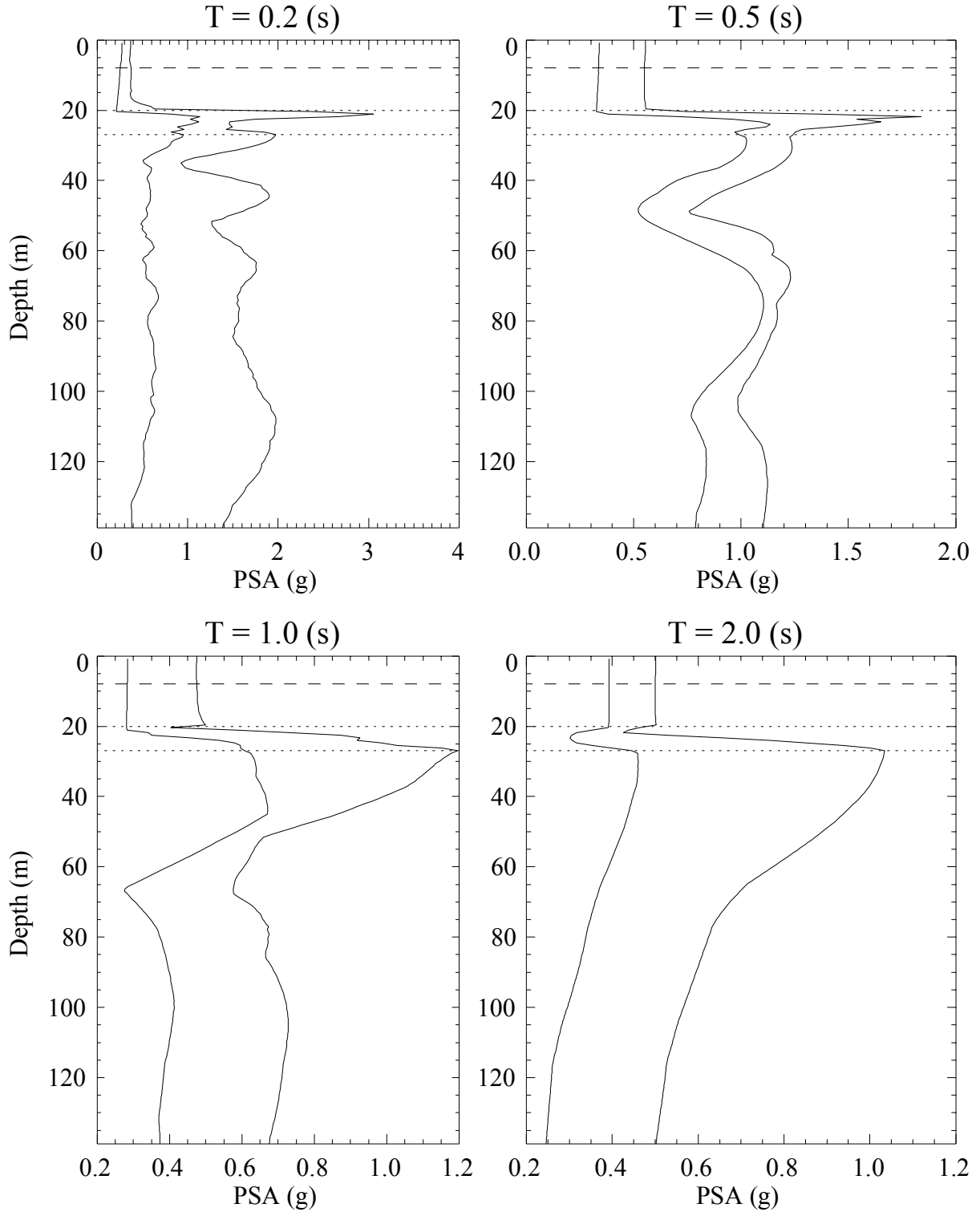


Figure 6-64: SMW soil acceleration response spectra for rock response input motions. Title of each figure is the period. The solid lines indicate minimum and maximum responses at each depth from the six input ground motions. Horizontal dotted lines show the depth range of the low-velocity layer with nonzero porosity. The high-velocity SMW layer is located between the horizontal dashed line and the top dotted line. The lower-velocity SMW layer is located above the horizontal dashed line.

1995 M 6.9 Kobe earthquake) increased from ~ 0.3 g at the surface, to ~ 0.6 g at 16.4 m depth, and ~ 0.55 g at 32.4 m depth. Similarly, NOAH sometimes predicted large peak accelerations at depths that depended on the assumed depth of potentially liquefiable materials (see Appendices E and F). Information on the nonlinear soil properties as a function of depth below the dam is necessary to reliably predict peak accelerations, stresses, and strains at depth and at the surface. Due to the presence of the soil-mix columns with low velocities to 10-30 foot depths, underlain by higher velocity soil-mix (Wright, 1990) and the compacted soils beneath the dam, the material properties vary strongly in the upstream-downstream direction; both NOAH and SHAKE assume lateral homogeneity. The presence of the higher-velocity soil-mix columns than the surrounding soil, will result in amplification of seismic waves in the soil beneath the dam and in the untreated soil adjacent to the soil-mix columns.

6.7 Ground Motion Summary

The location of Jackson Lake Dam in the LVB located above the Teton fault results in substantial seismic loads at the dam associated with $M \sim 7$ earthquakes on the Teton fault. The hybrid ground motion simulations of $M \sim 7$ earthquakes on the northern Teton fault segment predict larger rock peak velocities, and comparable peak accelerations to those estimated at Casitas Dam (O'Connell, 1999b), previously the strongest seismic loads estimated for a Reclamation structure. Casitas Dam is located on the hanging wall of the Red Mountain reverse fault, placing it on the highest velocity rocks in the vicinity of the Red Mountain fault. Casitas Dam was subjected to maximum rupture directivity because it was located closer to the Red Mountain fault than Jackson Lake Dam is relative to the Teton fault. While much of the concrete portion of Jackson Lake Dam is located on ~ 1 km/s S-wave velocity material that would be considered rock sites in California, there are large velocity contrasts between the LVB containing the dam and the basement rocks. Thus, Jackson Lake Dam is located in the lowest velocity rocks in its crustal neighborhood and it experiences ground motion amplification as a result. Since the EGFs were used to construct the > 1 Hz responses and contain a wide variety of LVB-edge S-wave amplitudes and time moveouts relative to the direct S-wave arrival, the < 1 s PSA responses may be underestimated because LVB-edge S-waves would likely have more systematic move-outs, amplitudes, and phasing that represented by the random summing of eight EGF responses. In spite of potential underestimation of < 1 s period responses, the hybrid ground motion simulations for Teton fault dips of 35° and

45°, the mean and 84% PSAs for periods > 0.35 s exceed Spudich et al.'s (1999) empirical predictions for rock for site JLDW; the combined influences of rupture directivity and the LVB amplify rock motions at the dam to produce PSA rock responses more like a soil site than a ~ 1 km/s S-wave velocity rock site. For a fault dip of 35°, the mean and 84% PSA exceed Spudich et al.'s (1999) empirical prediction for soil at rock site JLDW for periods > 1 s. For a fault dip of 45°, the mean and 84% PSA exceed Spudich et al.'s (1999) empirical prediction for soil at rock site JLDW for periods $> \sim 1.5$ s. Unfortunately, hanging wall LVB amplification produces ground motions at Jackson Lake Dam that mimic extreme ground motion characteristics of rupture directivity while producing extended durations of strong ground shaking, not typically associated with rupture directivity. The ground motions recommended for dynamic analyses of the concrete section of Jackson Lake Dam in Section 6.5 reflect these realities.

Ground motions are also provided for nonlinear analyses of the embankment section of the dam that reflect the extended durations and amplification associated with the ~ 140 -m-deep very-low-velocity glacial scour that is the foundation for most of the embankment section of the dam. To provide realistic inputs for nonlinear soil responses calculations at depth, these soil ground motions were constructed with a JLD3 site response to account for the wide variety of S-wave and interface wave phases that likely exist at depths > 25 m in the VLV glacial scour sediments. Nonlinear effective-stress soil response calculations with NOAH show that near-surface Arias Intensities and peak acceleration responses, and their associated durations are very sensitive to input motion peak amplitudes and durations. Certain combinations of input motions produced nonlinear soil Arias Intensity and Arias duration responses that exceeded corresponding rock responses by a factor of six. Nonlinear soil response (modulus reduction) may increase ground motions durations because interface phase velocities will be reduced, increasing the time required for Airy phases to propagate from the boundaries of the glacial scour to the dam.

Jackson Lake Dam is > 1.5 km long and spans a wide variety of foundation materials with widely varying S-wave velocities and straddles a region with $> 10:1$ S-wave velocity contrasts. These large velocity contrasts occur between the overcompacted till ($V_s \sim 1$ km/s) and the soils in the glacial scour ($V_s \sim 0.1$ km/s). S-wave velocities also vary both laterally and vertically within the glacial scour region that is composed of fluvial-lacustrine deposits with V_s varying from to 0.09

km/s to 0.2 km/s (Sirles, 1986). Ground motions are likely to vary substantially, both along the dam's axis and in the upstream-downstream direction, because the low soil S-wave velocities result in wavelengths nearly equal to the dam's width at 1 Hz. Chen and Harichandran (2001) showed that spatially varying ground motions are likely to substantially increase shear stresses in foundation materials at the toes of an embankment dam, particularly when spatial coherence is significantly < 1 for low frequencies. Santa-Cruz et al. (1999) showed that for low-velocity basins, the absolute value of coherency can be substantially less than 1 for frequencies as low as 0.3 Hz, for separation distances as low as 800 m, and for frequencies as low as 1 Hz, for separation distances as low as 100 m. Given the results of Santa-Cruz et al. (1999), and the substantial and variable thickness of low S-wave velocity materials in the glacial scour that comprises the foundation for the embankment section of the dam, and the strongly varying site responses noted in Chapter 5 from the Jackson Lake Dam site response stations, it is likely that ground motions coherency will be substantially < 1 for frequencies as low as 0.3 Hz along the embankment portion of the dam.

The southern portion of the dam, consisting primarily of the concrete section, is founded on ~ 1 km/s S-wave velocity till and tuff. The rest of the dam is founded on ~ 0.1 km/s S-wave fluvial-lacustrine deposits that increase in thickness towards the northern end of the dam. The southern portion of the dam will shake less strongly and for shorter durations than the rest of the dam. Consequently, the largest strains resulting from differential motions along the axis of the dam are likely to be located in the embankment section extending from the concrete section to station 32, where Sirles (1986) found a ~ 140 m thick section of fluvial-lacustrine deposits below the ground surface. The distances between stations JLD2 near the northern end of the concrete section and station JLD3 near station 24+00 is 356 m. For a vertically-incident shear wave, the propagation delay at station JLD3 relative to JLD2 due to ~ 140 m of fluvial-lacustrine fill with an average S-wave velocity of ~ 140 m/s is 0.87 s (1 s travel-time through the last 140 m for JLD3 and 0.13 s travel time through the last 140 m for JLD2). This yields a S-wave apparent velocity of 0.41 km/s, which will likely reduce S-wave coherency at low frequencies, based on the results of Santa-Cruz et al. (1999). This is an apparent velocity 10 times *smaller* than considered by Chen and Harichandran (2001) in their analyses of the influence of coherency on the dynamic analysis of embankment dams. Since the peak velocity loads at Jackson Lake Dam are substantially larger

than considered by Chen and Harichandran (2001), and apparent velocities are much lower, differential displacements, and correspond strains and stresses are likely to be larger at Jackson Lake Dam than those considered in Chen and Harichandran (2001). S-wave apparent velocities will decrease for S-waves arriving from the south (about half of the northern Teton rupture segment, and the entire southern Teton rupture segment). S-wave apparent velocities will be increased slightly for S-wave arrivals from north of station JLD3, but the increases in apparent velocity will be modest.

Consistent with past approaches to reduce ground motion estimation biases and uncertainties (Anderson and O'Connell, 1998; Anderson and O'Connell, 1993; O'Connell and Unruh, 2000; Ake et al., 2002) microearthquake data from the Jackson Lake Seismic Network provided the crucial information about the subsurface fault geometries, particularly dip of faults at depth, and seismotectonic constraints on state-of-stress and fault kinematics, information necessary to estimation ground motions at Jackson Lake Dam. The combination of broadband site response stations at Jackson Lake Dam and the short-period JLSN provided empirical Green's functions and the ability to estimate site responses in the same manner as the site response stations in previous studies (O'Connell and Ake, 1995; O'Connell, 1999b; O'Connell and Unruh, 2000; O'Connell, 2001), where local seismographic networks such as the short-period Southern California Seismic Network and the Northern California Seismic Network provided crucial information necessary to convert site response recordings into empirical Green's functions. The development of site-specific ground motions using empirical Green's functions substantially reduced ground motion biases in several previous studies (O'Connell, 1999a, 1999b; O'Connell and Unruh, 2000; O'Connell, 2001). For instance, site-response recordings used in conjunction with short-period data from the Southern California Seismic Network showed that convention approaches to estimating near-source ground motions at stiff-soil sites in southern California were likely to strongly overpredict peak ground motions (O'Connell, 1999a). At a high-velocity hard-rock site, broadband site-response data in conjunction with short-period data from the Northern California Seismic Network showed that source characterization of blind thrust faults in the western Sacramento Valley were incorrect (O'Connell and Unruh, 2000; O'Connell et al., 2001) and that peak acceleration loads would likely be about 2/3 empirical predictions, resulting in substantially lower final peak ground motion estimates (LaForge, 1999). Estimation of the 3D

velocity structure of the crust and discovery of the significant impacts of 3D velocity structure on peak ground motions and ground motion durations were made possible by the earthquake data from the JLSN and the broadband site response seismographs at Jackson Lake Dam. The earthquake data provided by the JLSN were necessary to fully exploit the site response earthquake recordings to develop empirical Green's functions and site response information for nonlinear soil analyses. At Jackson Lake Dam, development of site-specific ground motions increases confidence that estimated ground motions are not likely to be significantly biased.

There are several factors that produce significant ground motion uncertainties. The uncertainty in Teton fault dip produces at least a factor of two uncertainty in peak seismic loads at the dam. Since it appears the Teton fault is entirely located within basement rocks, a significant velocity contrast across the fault is unlikely; seismic reflection/refraction methods are unlikely to be able to image the fault at depth. Several earthquake recorded by the JLSN suggest the Teton fault dips $\sim 45^\circ$. As is typically the case at other Reclamation dams (Casitas, B.F. Sisk, Hoover, Monticello, O'Neill, and Ridgway Dams), earthquake locations and focal mechanisms are probably the only feasible way to constrain the dip of the Teton fault at depth, in the absence of a strong geodetic signal produced by a $M \sim 7$ earthquake on the Teton fault. Uncertainties in the spatial extent and velocities in the LVB produce, as yet, unknown uncertainties in peak ground motions and durations.

Uncertainties about the velocity structure and spatial extent of the glacial scour produce uncertainties of about a factor of two in peak soil ground motions, and factor of four uncertainties in soil ground motion durations. It is necessary to determine the wave-types that comprise the long duration soil ground motions to determine the appropriate methods to calculate nonlinear soil responses. Synthetic calculations in Section 5 indicate that a significant fraction of the long-duration high-amplitude soil motions at the dam may be produced by S-waves and horizontally propagating interface waves occurring at depth in the glacial scour basin.

The 20-station short-period seismographic network provided many critical pieces of data necessary to estimate ground motions at the dam. However, its configuration was not well-suited to obtain the seismic data necessary to substantially reduce remaining ground motion uncertainties. In particular, the vertical-component short-period JLSN did not provide S-wave

velocity constraints. Earthquake depth estimation capabilities in the vicinity of the Teton fault were limited by the large area spanned by the JLSN, the 10-20 km JLSN station spacing, and the absence of three-component seismographs. A smaller broadband three-component network located within and on the periphery of the LVB, combined with one or more soil borehole three-component packages at the dam, with three-component sensors at the surface and at several depths extending to ~50 m depth, would provide much more valuable and relevant information for Jackson Lake Dam than the 20-station short-period JLSN.

Earthquake magnitude is sometimes used as a proxy for ground motion duration in engineering analyses of soils. The earthquake magnitudes used to simulate ground motions at Jackson Lake Dam from earthquakes on the Teton fault should *not* be used for this purpose. Due to the proximity of the Teton fault to the LVB and glacial scour very-low-velocity basin, and the resulting peak ground motion amplifications, extended durations, and increased Arias intensities of ground motions at the dam, effective magnitudes for geotechnical analyses of the seismic loads are 7 1/2 for the rock ground motions, and are 8 for the soil ground motions. These recommended magnitudes for soil analyses are 1/4 to 1/2 magnitude units larger than the moment magnitudes of all-segment and northern segment rupture scenarios of the Teton fault, specifically to account for the extended durations and amplifications of ground motions observed at the dam (Section 5). The most likely scenarios for soil response based on section 5 and nonlinear soil calculations using NOAH indicate ground motion durations of at least 60 seconds and possibly as long as 120 s for the embankment portion of the dam.

Because this section only considers the Teton fault as a seismic source and background seismicity clearly increases the seismic loading rates (Section 3), it is necessary to increase annual exceedence probabilities relative to activity rates of the Teton fault to provide representative probabilistic seismic loads for dynamic analyses of the dam. These analyses are presented in the next section.